Pulsed Laser Deposition and Characterization of AlN, TiO_2, and $Zn_{1-x}Mg_xO$ ($0 \leq x \leq 0.7$) Semiconductor Thin Films

by

GAURAV SHUKLA

DEPARTMENT OF PHYSICS
INDIAN INSTITUTE OF TECHNOLOGY GUWAHATI
GUWAHATI INDIA
MAY 2011

Pulsed Laser Deposition and Characterization of AlN, TiO_2, and $Zn_{1-x}Mg_xO$ ($0\leq x\leq 0.7$) Semiconductor Thin Films

A Thesis

submitted in partial fulfillment of the requirements for the award of

the degree

of

DOCTOR OF PHILOSOPHY

by

GAURAV SHUKLA

DEPARTMENT OF PHYSICS
INDIAN INSTITUTE OF TECHNOLOGY GUWAHATI
MAY 2011

Dedicated to my Parents

INDIAN INSTITUTE OF TECHNOLOGY GUWAHATI

DEPARTMENT OF PHYSICS

STATEMENT

I hereby declare that the matter embodied in this thesis is the result of investigations carried out by me at the Department of Physics, Indian Institute of Technology Guwahati, Guwahati, India, under the supervision of Prof. Alika Khare. This thesis has not been submitted to any university, institute or elsewhere for the award of the any degree, diploma or associateship.

Date: …25/05/2011……. **Gaurav Shukla**

भारतीय प्रौद्योगिकी संस्थान गुवाहाटी
Indian Institute of Technology Guwahati
Department of Physics
Guwahati-781039, Assam State, INDIA
Phone: +91 361 2582705, 2582701, 2690321 to 328 (extn. 2705),
Fax: +91 361 2582749

Dr. Alika Khare
Professor
E-mail: alika@iitg.ernet.in, k_alika@yahoo.com

Date: 25/05/2011

Certificate

This is to certify that work contained in the thesis entitled ‘**Pulsed Laser Deposition and Characterization of AlN, TiO_2, and $Zn_{1-x}Mg_xO$ ($0 \leq x \leq 0.7$) Semiconductor Thin Films**’, by **Mr Gaurav Shukla** (Roll no. 05612103), a student of Department of Physics, Indian Institute of Technology Guwahati, for the award of degree of Doctor of Philosophy, has been carried out under my supervision and that the same has not been submitted elsewhere for a degree.

(Alika Khare)

ACKNOWLEDGEMENTS

I wish to express my sincere appreciation to my research supervisor, Prof. Alika Khare, for giving me an opportunity to pursue this research work, for her continuous care, invaluable advice, guidance, encouragement, and supervision of the research. I must acknowledge the unconditional freedom to think, plan, execute and express, that I was given in every step of my research work.

My gratitude goes to my doctoral committee members, Dr. Pratima Agarwal, Dr. Sunil Kumar Khijwania, Dr. Saurabh Basu and Prof. J. B. Baruah for their timely and invaluable suggestions, which helped me to improve the work pertaining to PhD thesis. I owe my thanks to the Department of Physics, IIT Guwahati and CIF, IIT Guwahati for providing me the necessary facilities to fulfill my PhD thesis objectives. In particular, I would like to extend my sincere thanks to Mr. Chandan Burgohain, Mr. K. K. Senapati, Dr Sidananda Sarma, Mr Atul Chandra Deka, Mr Bimal Kumar Sarma and Mr Madhurjya Borah for their kind help with various instruments.

I would like to thank MHRD, India and IIT Guwahati for providing financial assistance during my Ph.D. tenure.

It was pleasure to work with my research lab members Dr.Archana, Arpita, Abu, Indrajeet, Partha, and Satchi. Thanks to them for their suggestions, time, help in experiments and kindness throughout my PhD.

I am deeply indebted to all my friends at IIT Guwahati for providing a welcome diversion from the critical situations during my PhD, whenever I needed. I must acknowledge all my friends for their love, encouragement and support.

My special thanks and appreciation goes to my parents as well as my family for their blessings, love, patience, support and understanding throughout my studies and most of all to the Almighty God who made everything possible.

Date: …25/05/2011…… **Gaurav Shukla**

ABSTRACT

The focus of work presented in this thesis was to understand and optimize the pulsed laser deposition (PLD) process to fabricate thin films of three important wide band gap semiconductors, AlN, TiO_2 and $Zn_{1-x}Mg_xO$ ($0 \leq x \leq 0.7$). These three materials were chosen due to their potential for opto-electronic applications in the UV region.

AlN thin films were deposited onto Si (100) at room temperature in N_2 ambient using PLD technique. The use of pure Al metal as target in the present work, instead of AlN ceramic pellets has made the PLD system simplified. Highly (002) oriented wurtzite AlN thin films were grown in low N_2 pressure regime (0.05 mbar to 0.10 mbar) while (101) oriented wurtzite AlN thin films were obtained in high pressure regime (10 mbar to 100 mbar). The emission spectrum of laser ablated Al plasma in N_2 ambient was studied to understand the deposition process.

TiO_2 thin films were deposited using PLD in Ar and O_2 ambient. As-deposited thin films of TiO_2 were having anatase phase which were converted to rutile phase with annealing. TiO_2 films deposited in O_2 ambient converted into rutile nanorods upon annealing. TiO_2 films deposited in Ar ambient preserved the anatase phase upon annealing and showed nanocone structures. The Ti:O ratio was found to be more stochiometric for films deposited in O_2 ambient as compared to Ar ambient.

ZnO thin films were deposited using PLD technique on to Si (100) substrates in O_2 ambient. From the spectroscopic measurements of laser induced ZnO plasma, O_2 pressure and target substrate distance was optimized for the deposition of c-axis oriented stochiometric ZnO thin films.

Bandgap of ZnO was tuned by alloying with MgO. $Zn_{1-x}Mg_xO$ composite thin films were deposited via PLD onto (0001) sapphire substrates in O_2 ambient. Wurtzite structure was obtained for $Zn_{1-x}Mg_xO$ alloy films up to 34 % Mg concentration and cubic phase for 60 % and above of Mg concentration. Excitonic emission was observed from the c-axis oriented $Zn_{1-x}Mg_xO$ ($0.0 \le x \le 0.34$) thin films. Effect of Mg concentration and substrate temperature on the exciton band gap, exciton binding energy, and broadening parameter was studied from the absorption spectra. The annealing of the sapphire substrate prior to the deposition enhanced columnar growth and crystallinity of the $Zn_{1-x}Mg_xO$ films.

The second harmonic generation, MPA induced UV emission and Non-linear absorption co-efficient, nonlinear refractive index and third order nonlinear susceptibility in $Zn_{1-x}Mg_xO$ thin films were studied. The NLO properties of these films were found to be decreasing with increase in Mg content.

Vertically oriented ZnO nanorods were hydrothermally grown onto pulsed laser deposited ZnO seed layer. The effect of pre-heating time, seed layer and growth time on the structural and optical properties of these nanorods was discussed. Nonlinear absorption coefficient and nonlinear refractive index were estimated using z-scan technique and found to be enhanced significantly compared to that of pulsed laser deposited ZnO seed layer. Lasing action and harmonic generation in ZnO NRs having high aspect ratio was realized via multiphoton absorption process.

CONTENTS

LIST OF FIGURES

LIST OF TABLES

ABBREVIATIONS

AFM – Atomic Force Microscopy

ASE – Amplified Stimulated Emission

CVD – Chemical Vapor Deposition

DSO – Digital Storage Oscilloscope

EBD – Electron Beam Deposition

EDAX – Energy Dispersive Absorption X-ray

EHP – Electron Hole Plasma

FP – Fabry Perot

FTIR – Fourier Transform Infra Red

FWHM – Full Width at Half Maximum

HRTEM – High Resolution Transmission Electron Microscope

IBD – Ion Beam Deposition

LED- Light Emitting Diode

LIP – Laser Induced Plasma

LIPS– Laser Induced Plasma Spectroscopy

LTE – Local Thermodynamic Equilibrium

MBE- Molecular Beam Epitaxy

MIS – Metal Insulator Semiconductor

MOCVD – Metal Organic Chemical Vapor Deposition

MPA – Multi Photon Absorption

NLO – Non Linear Optical

NR – Nanorod

OES – Optical Emission Spectroscopy

PD – Photo Diode

PMT – Photo Multiplier Tube

PL – Photo Luminescence

PLD – Pulsed Laser Deposition

RF – Radio Frequency

SAED - Selected Area Electron Diffraction

SEM – Scanning Electron Microscope

SHG – Second Harmonic Generation

TEM – Transmission Electron Microscope

THG – Third Harmonic Generation

TPA – Two Photon Absorption

UV – Ultra Violet

VLS – Vapor Liquid Solid

WBG – Wide Band Gap

XRD – X-Ray Diffraction

3PA – Three Photon Absorption

SYMBOLS

α – Absorption coeeficient

β – Nonlinear absorption coefficient

n_2 – Nonlinear refractive index

Δm – Supersaturation

R – Actual deposition rate

R_e – Equilibrium deposition rate

T_s – Substrate temperature

k – Boltzmann constant

h – Planck's constant

N_e – Electron density (of laser induced plasma)

T_e – Electron temperature (of laser induced plasma)

ΔE – Energy difference between transition levels

I_{ji} – Line intensity of the transition from upper state j to lower state i

E_j^z – Energy of level j (ionization stage z)

g_j – Degeneracy of the level j

A_{ji} – Transition probability from level j to i

N^z – number density of ionization stage z

U^z – Partition function of ionization stage z

λ_{ji} – Transition wavelength from level j to i

λ – Wavelength

λ_o – Center wavelength

$\Delta\lambda_D$ – Doppler broadening

$\Delta\lambda$ – Stark broadening

m – Atomic mass

ω – Angular frequency of laser

ω_{imp} – Elecetron impact parameter

A- Ion broadening parameter

L_{eff} – Effective sample length

z_o – Rayleigh length

w_o – Beam diameter at focus

f- Focus length

$\Delta\phi$ – Nonlinear phase change

T – Transmittance

$\chi^{(3)}$ – Third order nonlinear susceptibility

n_o – Linear refractive index

c – Speed of light

Chapter 1

Introduction

Pulsed laser deposition (PLD) technique is emerging as a promising thin film deposition technique because of its ability to process almost any material to yield thin films of desired composition and thickness ranging from nm to micron [1-3]. The technique of laser ablation is very flexible and the composition of the thin film can be controlled by the composition of target material, laser power, target-substrate distance and the back ground pressure. The major advantages of PLD are its small installation setup, adaptability towards multiple upgrades, possibility of in-situ measurements during deposition and direct processing technique for the deposition of thin films. PLD requires low deposition temperature and can even deposit crystalline films at room temperature [4-6]. PLD appears to be a suitable method to transfer stoichiometrically complex monolayer structures from single or composite targets to the substrate in nitrogen/oxygen environment [7]. PLD was first proposed in the early 1960's [8], soon after the first high power ruby laser became available, and was first demonstrated by Smith and Turner in 1965 [9]. Although PLD technique has been developed and improved since its first stage, it became more and more popular in 1980's [10, 11]. PLD has been successfully employed for ceramic superconductor thin films [12, 13]. It has been also highly successful in stochiometric growth of multi-component thin films using a single target which is difficult to achive using other deposition techniques [14-16]. Growth of functional materials and multi layer hetero-structures became possible with the advanced PLD systems [17, 18].

1.1 Pulsed Laser Deposition Technique

The schematic of a typical PLD system is shown in Fig 1.1. It utilizes mostly excimer [19, 20] or harmonics of Q switched Nd:YAG lasers for ablation of target [21, 22]. In a PLD system, a focused high power laser beam (laser intensity ~ 10^9 – 10^{11} W/cm^2 and pulse duration ~ 6-20 ns) strikes onto a target placed inside an ablation chamber maintained at low back ground gas pressure (10^{-3} to 10^{-1} mbar) or under high vacuum. Due to the interaction of very high power laser with matter within the focal volume, highly energetic forward-directed plasma (plume) is generated [23, 24]. This plasma containing ions and neutrals of target material further expands and reacts with the background gas. The back ground gas may also be ionized either in the vicinity of the target directly via laser or via collision with high energetic charged particles of laser induced target plasma. Afterwards, recombination process takes place which results in vapour phase growth of desired molecules. These molecules condense and deposit in the form of thin film onto the surface of a cleaned substrate which is mounted inside the ablation chamber through a substrate holder. Usually the substrate holder is fitted with substrate heater to heat the substrates up to 800^o C during the film growth. The initial vacuum may be of the order of 10^{-6} mbar. As per the requirements of the particular film growth process, different types of working gases can be filled inside the vacuum chamber using appropriate gas inlet ports. The gas pressure inside the chamber can be monitored with appropriate pressure gauges attached to various ports of the chamber. The quality and properties of the thin film can be modified by performing the PLD in different background gases. The role of back ground gas is either to thermalize the highly energetic plasma species or to compensate for the loss of an elemental component of the target due to localized laser heating [25, 26]. The optical steering system for focusing the laser on to the target is placed out side the vacuum chamber and hence avoiding the contamination of expensive high damage threshold optics.. The multiple-target mounting assembly can also be adopted for the PLD system for the growth of multicomponent/multilayer/hetero-structure thin film [27, 28].

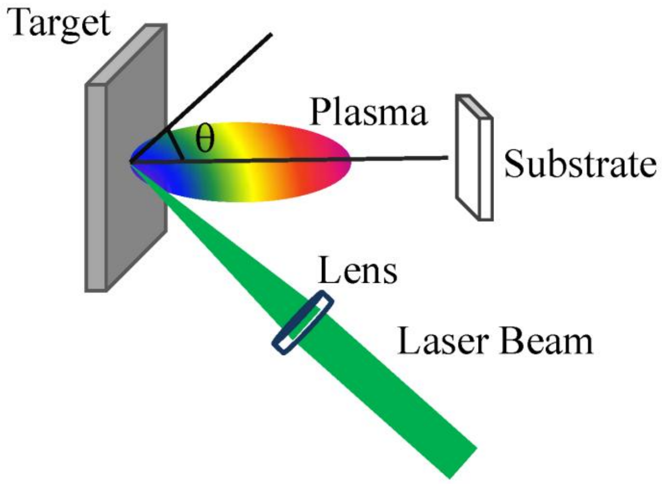

Fig. 1.1 Schematic of pulsed laser ablation set-up

1.1.1 Mechanism of pulsed laser ablation and deposition of thin films via PLD

The process of interaction of high power laser with the target is extremely complicated [29-31]. It depends on the parameters of high power laser; laser irradiance, pulse duration, wavelength as well as on to the optical and thermo-physical properties of target material [32, 33]. When the focused laser irradiance on to the target is ≤ 10^6 W/cm^2, the absorbed radiation appears in the form of heat and results into the minor modification on the surface of the target [34]. When the irradiation is in the range of 10^6-10^7 W/cm^2, intense local heating followed by melting and evaporation of the target material results into the ejection of neutrals and molecules [34]. In this intensity regime, coupling of the laser beam to the target occurs by photon-electron coupling and the target material undergoes an electronic excitation [35]. This interaction occurs within a sub nano -second. The energy associated with the electronic excitation is transferred to the material through electron- phonon coupling, which takes less than a nanosecond. This conversion of photon energy to thermal energy results in rapid localized heating, melting and evaporation of the surface layer [36]. The amount of evaporated target material will depend upon the absorption length of the laser beam with in the target material [37].

At further higher intensity, > 10^8 W/cm^2, the absorption of the radiation is dominated by multiphoton absorption [38] causing the multiphoton ionization of the target atom/molecules inducing the direct emission of positive ions and electrons. This results into the formation of plasma of the target surface with in the focal regime of the laser. This plasma plume expands and the further absorption of laser energy takes place within plasma via an inverse Bremsstrahlung process that involves the absorption of a photon by a free electron [39]. The expanding plasma will absorb the largest fraction of the laser beam energy close to the target surface [35]. Near the target surface, plasma temperature is very high (few ev to few tens of ev or more, depending on the focal intensity of laser) and expands with very high velocities (~10^6 m/sec) [40-42]. The very high expansion velocities of the plume results in the rapid decrease of the plasma density and temperature as it moves away from the target surface. When the target is placed in an gaseous ambient then the gas molecules also undergo ionization/ dissociation/ plasma formation via multiphoton absorption of laser energy in the vicinity of focal spot (on the target) as well as via interaction of highly energetic plasma plume of the target. Both these plasmas (target plasma and background gas plasma) undergo adiabatic cooling and under suitable dynamics undergo the reaction phase to form the molecular species.

Finally, the condensation of ablated species/ molecular species contained within adiabatically cooled plasma takes place. These condensed particles (adatoms) nucleate onto the substrate surface and growth of the thin film starts. There are three modes of thin film growth, Stranski-Krastanov growth (layer-plus-island), Volmer-Weber growth (island only), and Frank-van der Merwe growth (layer-by-layer) [43]. Depending upon the substrate surface energy, lattice orientation and dynamics of the laser induced target plasma; any of the three modes can be preferred for the film deposition.

The growth of epitaxial thin films on a single crystal surface depends critically on the interaction strength between adatoms and the substrate surface as well as on the dynamics of the laser-induced target plasma. The two main thermodynamic parameters which determine the growth mechanism and the properties of thin films are the substrate temperature T and super saturation Δm. The super saturation Δm, can be defined as [44],

$$\Delta m = kT_s \ln(R / R_e) \tag{1.1}$$

where k is the Boltzmann constant, R is the actual deposition rate, and R_e is the equilibrium deposition rate at substrate temperature T_s. In the PLD process, $kT_s \sim 2.5 \times 10^3$ J/mol and $R/R_e \sim 10^7$ and hence $\Delta m \sim 10^5$ J/mol [45]. This high degree of the super saturation or high deposition rate can lead to the two-dimensional nucleation with monoatomic height, which is favorable for the layer growth mode [43, 44].

The laser ablated plasma is characterized by a high density (results in high deposition rate), high ionization degree (up to 70%), and a high kinetic energy (from several eV to 100 eV) [40-42]. The thermal and kinetic energies of evaporated species play an important role in the film growth process. If the thermal energy of the species within the plume is much less than the dissociation energy of the molecules of the target material, the resultant thin films may not be able to keep the stoichiometry of the multi-component target material [45]. On the other hand, high kinetic energy of the laser ablated plasma species is responsible for radiative defect (vacancies) formation in the single-crystalline substrate. These defects act as additional crystallization centers. As a result, the epitaxial growth can be realized at a lower substrate temperature compared to other techniques. In addition various deposition parameters like deposition pressure, target-substrate distance, laser irradiance, ambient pressure and the nature of ambient affect the properties of the pulsed laser deposited wide band gap semiconductor thin films.

1.2 Characterization of Laser Ablated Plasma

The properties and dynamics of laser induced target plasma heavily influence the growth process and properties of deposited thin films. Hence to obtain the optimum parameters for deposition of high quality thin films of oxide or nitride WBG semiconductors via PLD technique and to understand the growth mechanism, dynamics of the laser ablated target plasma have to be studied.

1.2.1 Optical Emission Spectroscopy

The laser induced plasma (LIP) emits the characteristics spectrum of its constituent ionic, neutral and molecular species. The recording and analyses of this characteristics spectrum is termed as Laser induced breakdown spectroscopy (LIBS) or Optical emission spectroscopy (OES). OES forms a powerful tool to monitor the plasma density and plasma temperature of

LIP [46-48]. LIBS is a very sensitive technique and is being used for the analyses/detection of very small quantity of material [49-52].

1.2.2 Measurement of Laser induced Plasma Parameters

The electron density in LIP can be measured by recording the stark broadening of emitted line profile [53, 54]. The electron temperature can be estimated using the Boltzmann and Saha–Boltzmann equations [55-57]. Both these techniques are applicable to the optically thin emission line [58] where self absorption of the emitted transitions is negligible. In the optically thick plasma, due to the self absorption, the spectrum line profile will be distorted and requires some correction to it for correct interpretation [59].

1.2.2.1 Measurement of Electron Temperature

The estimation of the electron temperature from OES is based on the assumption of local thermodynamic equilibrium (LTE) in plasma where electrons are assumed to be under Maxwellian distribution. For LTE to hold in the plasma, the collisions with electrons have to dominate over the radiative processes. This condition requires a sufficiently large electron density. McWhirter [60] has proposed a critical electron density above which collisional rates are at least ten times than that of radiative rates. For an energy gap difference ΔE between the transition levels, the McWhirter criterion for LTE is:

$$N_e \geq 1.6 \times 10^{12} T_e^{1/2} (\Delta E)^3 \ \text{cm}^{-3} \tag{1.2}$$

where N_e is the electron density, T_e is the electron temperature (K) and ΔE is the energy difference between the transition levels (eV).

The critical electron density in LIP are typically in the range 10^{15}–10^{16} cm^{-3} [61] and is below the electron density observed in PLD process thus satisfying the LTE criteria.

Under the LTE assumption, the ratio of the relative intensities of two emitted lines from an element in same ionization stage can be related to the electron temperature using Boltzmann equation, [55, 56]:

$$\ln\left(\frac{I_{ji}\lambda_{ji}}{A_{ji}g_j}\right) = -\frac{E_j^z}{kT_e} + \ln\left(\frac{hcN^z}{4\pi U^z}\right) \tag{1.3}$$

In Eq. (1.2), the superscript z refers to the ionization stage ($z = 0$ for neutral atoms, $z = 1$ for singly-charged ions), I_{ji} is the line intensity of the transition from upper state j to lower state i, A_{ji} is the transition probability, λ_{ji} is transition wavelength, T_e is the electron temperature, N^z is the total number density, E_j^z and g_j are the energy and degeneracy of the energy level j, U^z is the partition function, k is the Boltzmann constant, h is Planck's constant and c is the speed of light. The level energies, degeneracy and transition probabilities are very well documented in various atomic databases. The Boltzmann method has the advantage of its simplicity, and has been used frequently in the LIPs having transitions in the visible region of the spectrum. The main disadvantage of the Boltzmann method is that it may lead to considerable uncertainties in the determined temperatures which are related with the probability of large relative error in the intensity ratio of different transitions within same ionization stage for temperature estimation.

Saha–Boltzmann equation over comes the limitation of Boltzman distribution. It compares the relative intensities of lines from subsequent ionization stages of the same element and is given by [56]:

$$\frac{I_{ki}^z}{I_{ji}^{z-1}} = \frac{2(2\pi mkT_e)^{3/2}}{N_e h^3}\left(\frac{g_k A_{ki}}{\lambda_{ki}}\right)^z \left(\frac{\lambda_{ji}}{g_j A_{ji}}\right)^{z-1} \exp\left(-\frac{(E_k^z - E_j^{z-1} + V^z)}{kT_e}\right) \tag{1.4}$$

where I_{ki}^{z} and I_{ji}^{z-1} are the intensities of corresponding transitions of z and (z-1) ionization stages, g_k and E_k^z is the degeneracy and energy of level k, respectively. A_{ki} and λ_{ki} is the transition probability and wavelength of transition k to i, respectively while A_{ji}, g_j, E_j^{z-1}, and λ_{ji} represent the corresponding parameters for the transition j to i of ionization stage (z-1). N_e is the electron number density, T_e is the electron (plasma) temperature, V^z is the ionization potential of stage z, h is the Planck's constant, k is Boltzmann constant, and m is the electron mass. Equation 1.3 or eq. 1.4 can be easily used to estimate the electron temperature T_e from the intensities of emitted LIP spectrum.

1.2.2.2 Measurement of Electron Density

The shape and width of the spectral lines emitted by plasma are governed by the collisional processes perturbing the emitting atoms and ions. Hence, the plasma density can be estimated from the profile of the spectral line. The main contributions to the broadened line profile are the Stark effect, Doppler broadening, and instrumental width [51-52, 62-64]. The Doppler broadening can be estimated from the relation [62, 65],

$$\Delta\lambda_D = \lambda_0\sqrt{\frac{8kT_e\ln 2}{mc^2}} \tag{1.5}$$

where λ_o is the center wavelength, k is the Boltzmann constant, T_e is the plasma temperature, m is the atomic mass and c is the velocity of light. At a temperature of 10,000 K, the Doppler width is estimated to be ≈ 0.005 nm for the transitions in visible range. The instrumental widths are typically around 0.01 nm for such experiments. Thus, the dominating contribution to the line width is attributed to the Stark effect. The full width at half maximum (FWHM) of a Stark broadened line is expressed as [66, 67],

$$\Delta\lambda = 2\omega_{imp}\left(\frac{N_e}{10^{16}}\right) + 3.5A\left(\frac{N_e}{10^{16}}\right)^{1/4}(1-1.2N_D^{-1/3})\omega_{imp}\left(\frac{N_e}{10^{16}}\right) \tag{1.6}$$

Here, ω_{imp}(nm) is the electron impact parameter, which is a weak function of temperature, A (nm) is the ion broadening parameter, N_e (cm^{-3}) is the electron number density, and N_D is the number of particles in the Debye sphere. The contribution due to the ion broadening is much smaller than the broadening due to electron impact; therefore, it can be neglected [51-52] and, thus, only the first term on the right hand side of eq. (1.6) is sufficient to extract the number density. Hence eq. (1.6) reduces to a well known simple form,

$$\Delta\lambda = 2\omega_{imp}\left(\frac{N_e}{10^{16}}\right) \tag{1.7}$$

The Stark broadened emission line profiles are recorded experimentally and by fitting to the Lorentzian profile, FWHM of the emission line $\Delta\lambda$ can be obtained and electron number density N_e can be calculated using eq. 1.7.

1.3 Advantages and drawbacks of PLD

The most important feature of the PLD is the high kinetic energy (2 eV-100 eV) of the ablated species [40-42]. In comparison, the average kinetic energies of the impinging atoms in MBE are around ~ 0.1 eV and in sputtering are of the order of ~ 1-2 eV [68, 69]. The high energy of the ablated species allows growth of high-quality thin films at relatively low temperature. Using PLD, epitaxial films can be grown at relatively low temperatures down to room temperature [4-6]. The lower growth temperature also reduces the possibility of clustering of dopants and evaporation of elements with high vapour pressure from the pulsed laser deposited thin films. The high density of LIP in the presence of a background gas results into high deposition rates. In PLD, nano-second pulsed laser having repetition rates of few tens of pulses per second is used [19, 21]. In between two successive pulses, the time of no deposition (~ ms) allows for surface relaxation and improves film morphology. The spatially confined LIP plume ensures minimum contamination in side the chamber and helps in preserving the stoichiometry in case of multi component target for the deposition of hetero-structures. The pulsed nature of the PLD allows the film thickness to be controlled precisely by varying the pulse repetition rate or exposure time of laser. PLD is an extremely versatile technique and thin films of almost all the materials, including metal, ceramics and polymers can be deposited by it.

The non–equilibrium nature of the PLD growth process permits the growth of novel materials having metastable phases and introducing dopant concentrations in excess of the thermodynamic limits. In addition, the minimal interaction between the laser and the gas species allows a relatively high dynamic range of deposition pressure and relaxes the requirements for ultra high vacuum system. The ease of manipulation and handling of the laser source makes PLD a much simpler deposition technique compared to electron or ion beam deposition techniques.

The major drawback in the PLD technique is the non-uniform distribution of plasma resulting into spatial variation in thickness [32]. The forward-directed plume is responsible for the spatial thickness variation in the films grown by PLD. The spatial variation of film thickness is given by $\cos^p\theta$, where θ is the angle between the radial vector and the surface normal to the plane of the target [Fig1.1] and p is the exponential factor varying between 8-12 depending on laser irradiance, irradiated spot-size, etc [70]. This variation in film thickness is of concerned only for large substrates. For smaller samples (≈ 1 cm x 1 cm), one can achieve fairly uniform growth by controlling the deposition parameters such as laser irradiance, substrate – target distance and spot size. For deposition of larger surface area, the use of rastering stage for the substrate can overcome this limitation.

1.4 Motivation for the present work

The present research work was aimed towards the fabrication and characterization of AlN, TiO_2, $Zn_{1-x}Mg_xO$ ($0\leq x\leq 0.7$) semiconductor thin films via PLD. These materials belong to the group of wide band gap (WBG) semiconductors which are important for the optoelectronics industries to generate the electromagnetic radiation towards the shorter wavelength (blue to ultraviolet region) [71-73].

Aluminum nitride is an *n*-type III-V nitride WBG semiconductor with hexagonal wurtzite structure and having 6.2 eV bandgap [74]. AlN is generally reported to be non-polymorphous. It shows high chemical stability, radiation hardness, thermal conductivity (320 W/mK) as well as electrical resistivity [75]. It has low thermal expansion coefficient (4 ppm/K) [76]. AlN is an extremely hard material (~9 at Mohs' scale) having a high melting temperature over $2000^{o}C$ [77] and has a high surface acoustic wave speed (5.67 km/sec) [78]. It shows piezoelectric effect and negative electron affinity [79, 80]. It is used for acoustic wave devices on Si, optical hard coatings for spacecraft applications, heat-sinks in electronics packaging application, buffer layer for GaN deposition, as well as electroluminescent devices in the wavelength range from 215 nm to the blue end of the optical spectrum [81-84].

ZnO is an II-VI oxide WBG semiconductor with an optical band gap of 3.37 eV. It possess multi-functional (piezoelectric, ferroelectric and dilute ferromagnetic) properties [85]. ZnO shows room temperature excitonic emission, very high radiation hardness, and strong UV luminescence [85]. The surface conductivity of ZnO is very sensitive to the exposure of various gases and hence it can be used to fabricate ZnO based gas sensors [86]. It shows wurtzite (B_4), zinc blende (B_3), and rocksalt (B_1) type crystal structures [87]. Due to its non-centrosymmetric crystal structure, ZnO has large non-linear optical coefficients, which make it a very promising candidate for various opto-electronic applications [88-92]. Room temperature excitonic emission from ZnO makes it a material of choice for ultraviolet light emitting diodes (LEDs) and laser diodes [93-95]. Lasing action can be achieved upon photo pumping or electrical pumping of nano-cavities created in the form of ZnO nanostructures [96, 97]. Vertically aligned ZnO nanorods with high aspect ratio are the most suitable nanostructure for the creation of such nano cavities capable of lasing [98].

To further harness the optical properties of ZnO for various optoelectronic applications in ultraviolet range, it is necessary to engineer the band gap of ZnO by making suitable composites with MgO [99-104]. In the $Zn_{1-x}Mg_xO$ alloy system, the emission wavelength can be precisely tuned towards UV region (3.3-7.8eV) by changing the Mg composition or by inducing thermal intermixing in the ZnO/ZnMgO superlattice by annealing [101]. $Zn_{1-x}Mg_xO$ also possesses unique figures of merit, the availability of lattice-matched single-crystal substrates (hexagonal ZnO and cubic MgO substrates to deposit the $Zn_{1-x}Mg_xO$ thin films with corresponding phase), relatively low thin film growth temperatures (200 – 700^{o}C), intrinsic visible blindness and radiation hardness, which are crucial for practical realization of optoelectronic devices.

In addition to II-VI oxides, TiO_2 is another interesting material with a lot of applications in the field of solar cells, photocatalysis, smart material applications and environmental sanitation etc [105-110]. Titanium dioxide crystallizes in three different structures; rutile (tetragonal) anatase (tetragonal) and brookite (rhombohedral) [111]. It is an *n*-type, wide band gap semiconductor (3.03 eV for anatase phase and 3.26 eV for rutile phase). The control over formation of different phases during deposition of TiO_2 thin films is important for various device applications [112-117].

The deposition of AlN, TiO_2 and $Zn_{1-x}Mg_xO$ thin films have been reported via metal oxide chemical vapour deposition method (MOCVD) [118], molecular beam epitaxy (MBE) [68], chemical vapour deposition (CVD) [119], electron beam deposition (EBD) [120], sputtering [69], and pulsed laser deposition (PLD) [8]. Out of these methods, MOCVD, MBE and CVD have been extensively used for deposition of AlN, TiO_2 and $Zn_{1-x}Mg_xO$ ($0 \leq x \leq 0.7$) semiconductor thin films. AlN thin films have been deposited using MOCVD [121], MBE [122], CVD [123, 124], PLD [125], and RF magnetron sputtering [126]. Among them the CVD techniques have been commonly used for the growth of AlN but the substrate temperature in conventional CVDs is very high ($>1000^oC$) [127] and a smooth surface morphology of AlN thin films cannot be obtained by this method due to its high grain growth rate. In MOCVD technique, precursors of Al and N are thermally decomposed at high pressures to deposit AlN thin films on to a suitably placed substrate [121]. During the deposition process, incorporation of redundant volatile decomposition fragments (carbon and oxygen) in the growing film can degrade its quality [128-130]. Pulsed laser deposition may be a more desirable process for the deposition of AlN due to its processing simplicity and scalability in the semiconductor industry.

PLD of WBG oxide semiconductors proved to be highly successful in comparison to other techniques [131]. ZnO/ZnMgO based homojunction and quantum well devices require low thin film deposition temperature to prevent the merging of successive intermediate layers [132], which is possible only via PLD. The control on stoichiometric growth of bandgap tailored composites can not be achieved using other deposition techniques except PLD.

There is hardly any report on pulsed laser deposition of AlN thin films at room temperature using pure Al as the target. On the other side, growth of ZnO and TiO_2 thin films using PLD is well established but the deposition of band gap tailored $Zn_{1-x}Mg_xO$ composites films using PLD is not much studied. The effects of various deposition parameters and plasma dynamics on to the properties of these thin films are not detailed in the literature at all. Hence in the present work, deposition of AlN, TiO_2 and $Zn_{1-x}Mg_xO$ ($0 \leq x \leq 0.7$) thin films using PLD technique is reported and effect of laser ablated plasma dynamics on the film growth process is analyzed.

1.5 Organization of Present Thesis

The objective of present research work was to optimize the pulsed laser deposition process of thin films of oxide and nitride semiconductors. It included the optimization of various growth factors and parameters like substrate annealing, substrate temperature, background gas pressure and after growth annealing of films. The structural, morphological and optical characterizations of pulsed laser deposited thin films were performed using various available techniques. The dynamics of laser ablated plasma during PLD of thin films was studied to optimize the process parameters and obtain high quality thin films. Further, lasing action and frequency up-conversion was studied in ZnO, Mg-doped ZnO thin films and ZnO nanorods.

The thesis organization and overview of various chapters is mentioned below:

Chapter 1, "*Introduction*", presents literature survey on the subject and discusses basic concepts of pulsed laser deposition technique and laser induced plasma spectroscopy.

Chapter 2, "*Experimental Details*" describes the setups assembled to fabricate the thin films of AlN, TiO_2, $Zn_{1-x}Mg_xO$ ($0\leq x\leq 0.7$) using PLD and to study the laser induced plasma dynamics. The substrate processing and target preparation techniques are described. The setups and growth techniques developed to study lasing action and non-linear optical properties of ZnO thin films/nanostructures are also documnetd in this chapter.

Chapter 3, "*Pulsed laser deposition and charecterization of AlN thin films*" discusses the effect of N_2 pressure, target substrate distance and laser intensity on structural and optical properties of pulsed laser deposited AlN thin films. The laser induced plasma of Al in N_2 ambient was studied to understand the probable mechanism of AlN formation in different phases.

Chapter 4, "*Pulsed laser deposition and charecterization of* TiO_2 *thin films*", describes room temperature deposition of mixed phase TiO_2 thin films and effect of post-annealing/O_2 pressure on structural and optical properties of TiO_2 thin films.

Chapter 5 is on, "*Pulsed laser deposition and charecterization of ZnO and* $Zn_{1-x}Mg_xO$ ($0<x\leq 0.7$) *thin films*". In the beginning of this chapter the dynamics of laser ablated ZnO plasma is discussed to understand the probable role of oxygen ambient in the depostion of these thin films. The properties of Mg-doped ZnO films deposited via PLD are presented. In the last section of the chapter, the improvement in the quality of $Zn_{1-x}Mg_xO$ thin films upon high temperature pre-annealing of sapphire substrate is detailed.

Chapter 6 "*Non-linear optical properties of ZnO and* $Zn_{1-x}Mg_xO$ *(*$0<x\leq0.1$*) thin films*" discusses the harmonic generation and measurement of non-linear absorption coefficient, nonlinear refractive index and third order susceptibilty in thin films of ZnO and $Zn_{1-x}Mg_xO$ ($0<x\leq0.1$).

Chapter 7, "Multiphoton absorption induced lasing action in ZnO nanorods" initially discusses the hydrothermal growth of vertically aligned ZnO nanorods of 3-4 µm length on to pulsed laser deposited ZnO seed layer, followed by NLO properties and multiphoton absorption (MPA) induced lasing.

The last chapter of the thesis, *Chapter 8* is the *concluding* chapter and it provides salient features of the present research work along with the possibilities of future explorations.

Chapter 2

Experimental Details

Pulsed laser deposition (PLD) is a promising technique for the deposition of stochiometric and multi-component/multilayer thin films for various applications. In the present thesis, PLD has been used to deposit thin films of AlN, ZnO, TiO_2 and $Zn_{1-x}Mg_xO$ ($0 \leq x \leq 0.7$) composites. In the PLD technique, growth and properties of deposited thin films are governed by the laser ablated plasma dynamics to a large extent. Hence, for optimization of deposition parameters, laser ablated plasma dynamics has been studied using the optical emission spectroscopy technique. The effect of the three process parameters; ambient pressure, target-substrate distance and laser irradiance have been analyzed to draw the correlation between laser ablated plasma dynamics and the optical as well as structural properties of the deposited thin films.

Further, to study laser action in ZnO nanostructures, hydrothermal growth technique was used to grow ZnO nanorods on to the pulsed laser deposited ZnO seed layer. Non-linear properties of ZnO and Mg-doped ZnO thin films were explored by recording frequency up-converted signals and z-scan. The experimental details of target preparation, substrate preparation, PLD setup, plasma spectroscopy setup, hydrothermal growth technique and other assembled setups are presented in this chapter.

2.1 Target Preparation

For the deposition of AlN thin film via PLD, high purity Al (99.998 %) (Alfa-Aesar) was used as the target material. Compared to AlN ceramic target for PLD of AlN [125], pure Al target is easy to handle and is of low cost. Aluminium was used in the form of a thick foil of 1.54 mm thickness, 1.5 cm width and 3 cm length. Before loading into the vacuum chamber, Al target was cleaned with 5% HF solution and then rinsed twice with acetone to remove surface oxide layers.

PLD of TiO_2 thin films was performed using rutile phase TiO_2 target. High purity ($\geq$ 99.9 %), rutile phase TiO_2 targets were prepared using chemical and solid state synthesis route. Chemically synthesized rutile powder was pressed into rectangular shape using a dye and sintered at 1100^{o}C for 3 hrs. After initial annealing, TiO_2 targets were further sintered at 1200^{o}C for 18 hrs to do the hardening.

ZnO targets were prepared from ZnO powder using solid state synthesis route. The pure ZnO (99.98%) powder was fine grounded and then pressed into round pellets of ~ 13 mm diameter using a dye with 10 MPa pressure. The pellets were sintered at 1200^{o}C for 24 hrs in a furnace to obtain the hard ZnO targets.

For the PLD of $Zn_{1-x}Mg_xO$ thin films, ZnO-MgO composite targets with Mg contents from 1 atom. % to 70 atom. % were prepared. MgO (99.99 %) and ZnO (99.98 %) powders were mixed in appropriate proportion and blended mechanically to obtain mixture of uniform composition. These mixtures, in the form of powder were grounded and pressed into round pellets of ~ 13 mm diameter. The final targets were obtained after the pellets were sintered at 1000°C for 12 hrs and then at 1200°C for 4 hrs. Two stage sintering process was employed in order to achieve uniform substitution of Mg into ZnO lattice. The compositions of $Zn_{1-x}Mg_xO$ targets used for fabricating the thin films of $Zn_{1-x}Mg_xO$ ($x = 0.00$ to $x = 0.65$) are listed in Table 2.1.

S.N.	***Composition of $Zn_{1-x}Mg_xO$ pellets***	***Weight of ZnO powder taken for a 5gm sample (gm)***	***Weight of MgO powder taken for a 5gm sample (gm)***
1	$Zn_{0.99}Mg_{0.01}O$	4.9746	0.0249
2	$Zn_{0.98}Mg_{0.02}O$	4.9495	0.0500
3	$Zn_{0.95}Mg_{0.05}O$	4.8731	0.1265
4	$Zn_{0.90}Mg_{0.10}O$	4.7388	0.2606
5	$Zn_{0.85}Mg_{0.15}O$	4.5978	0.4017
6	$Zn_{0.80}Mg_{0.20}O$	4.4488	0.5506
7	$Zn_{0.75}Mg_{0.25}O$	4.2912	0.7081
8	$Zn_{0.70}Mg_{0.30}O$	4.1243	0.8751
9	$Zn_{0.65}Mg_{0.35}O$	3.9472	1.0527
10	$Zn_{0.60}Mg_{0.40}O$	3.7588	1.2406
11	$Zn_{0.55}Mg_{0.45}O$	3.5582	1.4413
12	$Zn_{0.50}Mg_{0.50}O$	3.3439	1.6555
13	$Zn_{0.45}Mg_{0.55}O$	3.1147	1.8847
14	$Zn_{0.40}Mg_{0.60}O$	2.8689	2.1305
15	$Zn_{0.35}Mg_{0.65}O$	2.6046	2.3948

Table 2.1 Weight of ZnO and MgO Powders taken for making $Zn_{1-x}Mg_xO$ pellets with different compositions

2.2 Substrate Preparation

In the present work, polished Si (100), Al_2O_3 (0001), and Fused Silica (Quartz) have been used as substrates for the deposition of thin films of various materials. Before loading into the vacuum chamber, Si (100) substrate was cleaned ultrasonically in 5% HF solution for 5 min and then using methanol for 30 min. Al_2O_3(0001) and Fused Silica substrates were cleaned ultrasonically twice using methanol before the deposition. Substrate cleaning was performed to remove native surface oxide layers which can be detrimental for growth of high quality thin films, particularly for AlN thin film.

2.3 Pulsed Laser Deposition of Thin Films

Figure 2.1 shows the schematic of PLD setup assembled to deposit the WBG oxide and nitride thin films. The second harmonic of Q switched Nd:YAG laser (Model-Quanta systems-HYL101) with 240mJ/pulse energy (in 2nd harmonic) and 8ns pulse duration at 10Hz repetition rate is focused on to the target with a lens of focal length of 35 cm.

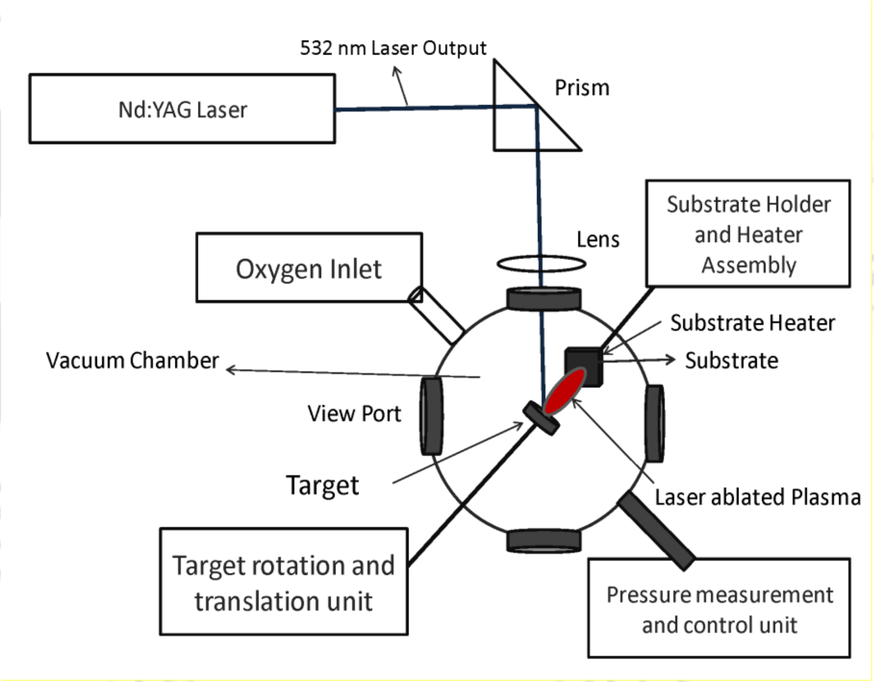

Fig. 2.1 Pulsed Laser Deposition Setup

The target was mounted inside an 8-port vacuum chamber (Figure 2.2) through a motorized vacuum compatible feed through from the top port of the chamber and continuously moved in order to avoid its piercing with the repeated shots of laser. The vacuum chamber was made of stainless steel in the form of a cylinder of 35 cm diameter and

30 cm height. The ports of the vacuum chamber were fitted with BK7 glass windows for plasma imaging and monitoring of the deposition process. It was mounted on the top of a movable steel rack with a diffusion pump attached below via 15 cm diameter baffle valve. The diffusion pump was oil based, filled with Silicone oil and capable of achieving base pressure below 10^{-5} mbar. The diffusion pump was backed by rotary pump. A roughing line was connected directly to the rotary pump for initial evacuation up to 10^{-3} mbar. The pressure measurement was performed using Pirani, Penning and capacitance gauges. The heating tapes were wrapped around the vacuum chamber to bake it during the evacuation. This has helped in removing the residual adsorbed oxygen molecules and water vapour from the chamber wall. For the deposition of AlN thin films, the chamber was baked and evacuated constantly for 2-3 days in order to minimize the oxygen content in the ambient as the Al plasma is very reactive to oxygen impurities during the deposition. For the oxide thin films, the chamber was baked and evacuated for 3-4 hrs only, to reach up to 10^{-5} mbar pressure before deposition.

The chamber was evacuated up to a base pressure of ≈ 10^{-5} mbar and then filled with required background gas ($N_2/O_2/Ar$) in the pressure range of 10^{-3} to 10^{2} mbar. The required gas cylinders were connected to the chamber via 25KF gate valve (on the neck of the ablation chamber) as shown in the Fig. 2.2. The background gas pressure was measured using capacitance gauge (Pfeiffer TPG 261 and MKS i-Baratron™).

The high power laser is focused on to the oxide or metal (Al) target at 45^{o} in the ambient of a reactive gas. The breakdown of target material in the focal region and the breakdown of gas in its neighborhood take place resulting into the plasma formation. This plasma, consisting of neutrals, ions and clusters of the target material as well as that of background gas, expands and undergoes the molecular formation under the suitable dynamics and is finally deposited on to the ultra sonically cleaned substrates [Si (100), Al_2O_3 (0001) and fused silica] placed parallel to and 2-5 cm distance apart from the target.

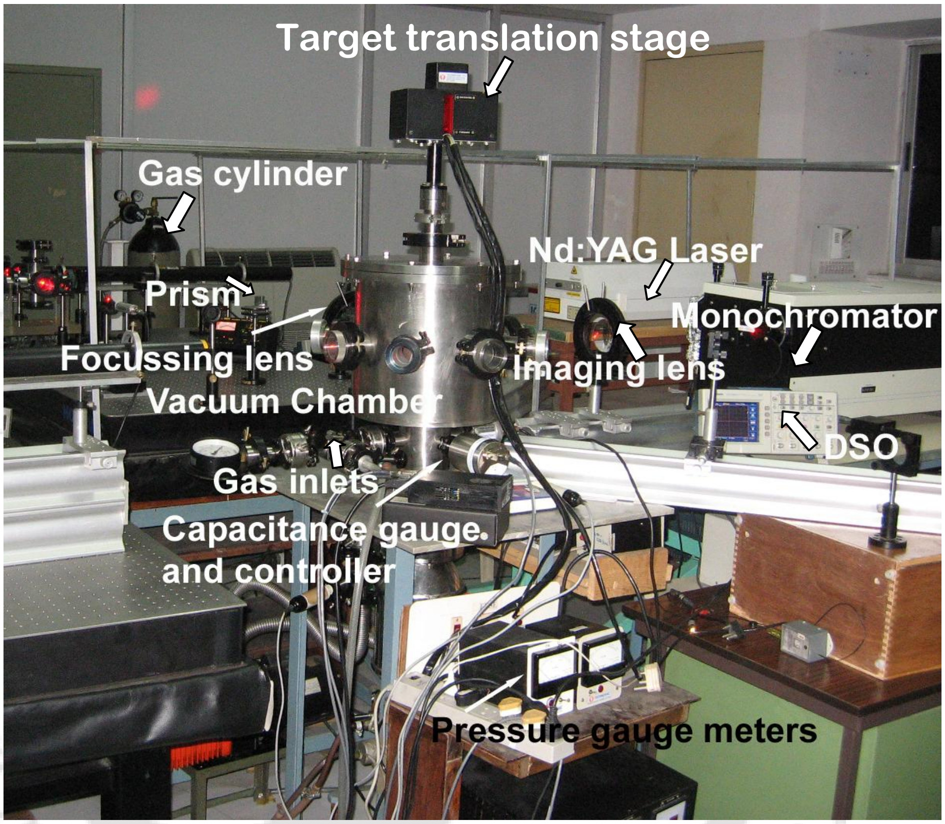

Fig. 2.2 Photograph of setup assembled for PLD and Plasma spectroscopy

The substrates were mounted on a substrate holder consisting of resistive heater to heat the substrate from room temperature to 750° C during depositions. This substrate holder was inserted via a Wilson feed through inside the ablation chamber. The heating of substrate during deposition helps in improving the crystalline properties and epitaxial growth of the thin films. The deposition time was varied in the range of 20-90 min for oxide and nitride thin films.

2.4 Plasma Spectroscopy

Upon laser irradiation on the targets (Al and ZnO) in different ambient, plasma, containing corresponding highly energetic neutral and ion species, was generated (for example, Al I, Al II, Al III, N II, and N III with Al target in N_2 ambient, Zn I, Zn II, and O I with ZnO target in O_2 environment). The laser ablated ZnO plasma in 0.1 mbar O_2 ambient is shown in Figure 2.3.

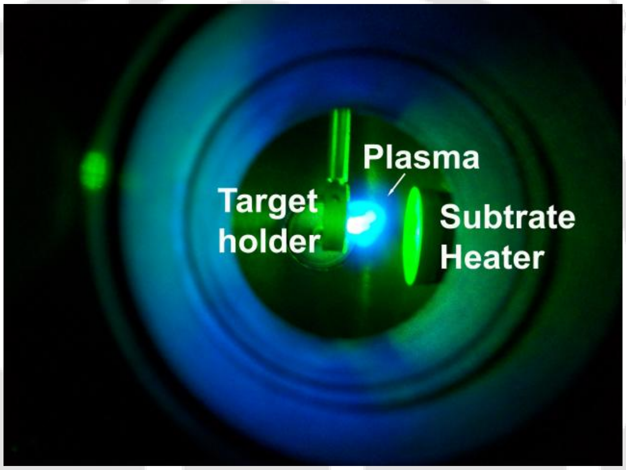

Fig. 2.3 Photograph of Laser ablated ZnO plasma

This plasma expanded adiabatically in a direction perpendicular to the target surface. As the plasma moves forward in the ambient, multiple complex processes takes place. The initial processes are laser plasma interaction and collision of plasma species with free electrons [23]. Further the ionization of plasma species and breakdown of background gas occurs. Finally, plasma cooling, recombination and chemical reaction takes place. The various excited species found in plasma plume emit out characteristic spectra. The emission spectra can provide important information about the dynamics of laser ablated plasma. To study the laser induced plasma (LIP) dynamics and to find correlation between LIP and the quality of thin films deposited via PLD, it is important to monitor and analyze the emission spectra of laser ablated plasma during the PLD process. The three important deposition parameters; background gas pressure, target-substrate distance, laser irradiance and substrate temperature can be optimized by studying the laser ablated plasma dynamics, to obtain the desired thin film. For this purpose, optical emission spectroscopy (OES) setup was assembled as shown in Figure 2.4.

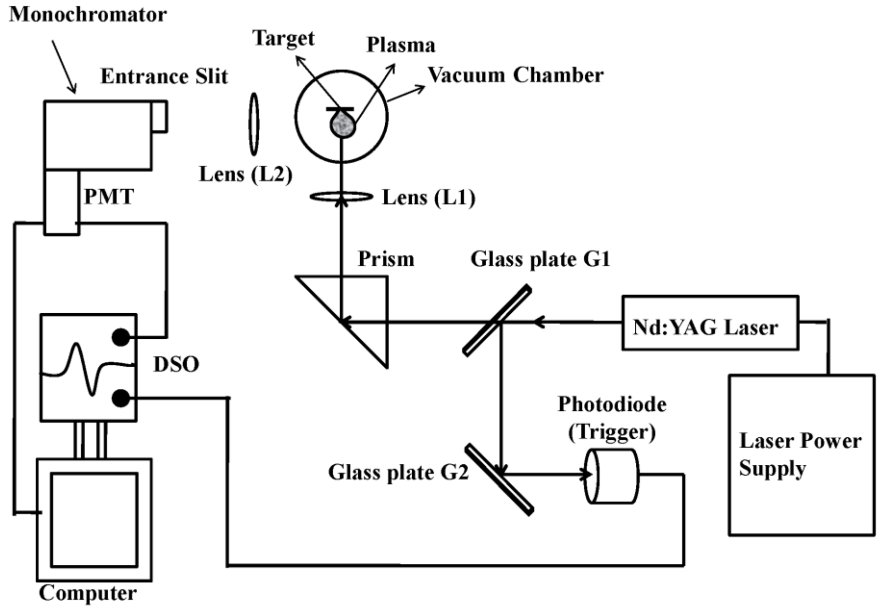

Fig.2.4 Experimetal setup to record the emitted spectrum from the laser ablated plasma

The expanding plasma in the direction perpendicular to the target surface was imaged in one to one correspondence using the lens (f = 25 cm) on to the entrance slit of the monochromator [SPEX 750M fitted with photomultiplier tube (PMT)]. The entrance and exit slit widths were kept fixed at 10 μm throughout the experiment. The controller of the monochromator (Data Scan 2 and Spex MSD 2) was interfaced with the computer installed with SpectraMax/Synergy software to facilitate the recording of plasma spectra. The laser ablated plasma spectra of different targets were recorded in the range of 300-850 nm. The spatially recorded plasma imaging was achieved by mounting the lens on a translation stage.

The lens was moved so as to image the different portions of the expanding plasma onto the entrance slit of the monochromator for recording.

The emission spectra of laser ablated Al plasma in N_2 ambient was recorded in the wavelength interval of 350-520 nm. The emission spectra of Al plasma recorded in 10^{-1} mbar N_2 pressure at a distance of 10 mm from the target surface and at 8×10^{11} W/cm^2 laser irradiance is shown in Figure 2.5. The observed transition lines of Al I, Al II, Al III, N II, N III and AlN band were identified using available database [154, 155] and listed in Table 2.1.

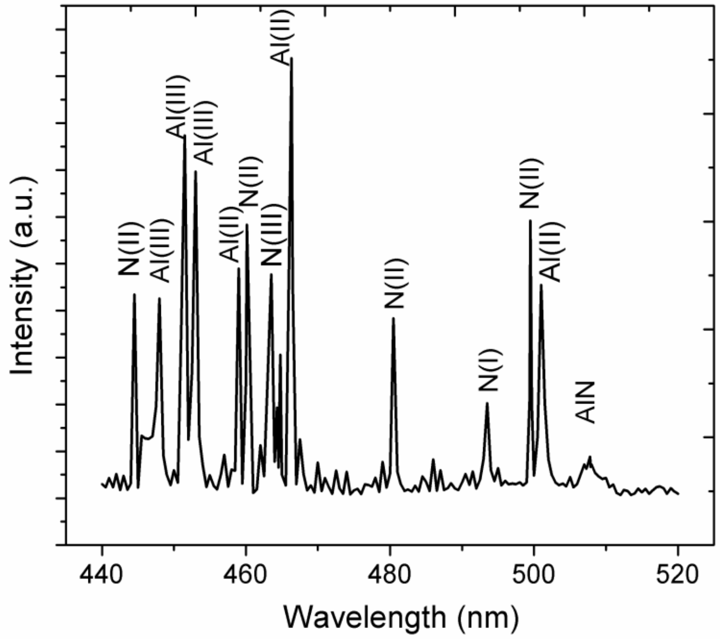

Figure 2.5 Emission spectra of Al plasma recorded at a distance of 10 mm from target surface in ambient N_2 pressure of 10^{-1} mbar and Laser irradiance of 8×10^{11} W/cm^2

Transitions	Wavelength (nm)	Configurations
Al I	396.15	$3s^2 3p(^2P^o)$-$3s_2 4s(^2S)$
Al II	358.65	$3s3d(^3D^o)$-$3s4f(^3F)$
	390.06	$3s3p(^1P^o)$-$3p^2(^1D)$
	445.13	$3s3p(^3P^o)$-$3s3p(^1P^o)$
	458.81	$3s4d(^3D)$-$3s7f(^3F^o)$
	466.30	$3p^2(^1D)$-$3s3p(^1P^o)$
	500.09	$3s4d(^1D)$-$3s8f(^1F^o)$
Al III	371.31	$2p^6 4p(^2P^o)$-$2p^6 5s(^2S)$
	447.98	$2p^6 4f(^2F^o)$-$2p^6 5g(^2G)$
	451.25	$2p^6 4p(^2P^o)$-$2p^6 4d(^2D)$
N I	493.51	$3s(^2P)$- $4p(^3S^o)$
N II	444.70	$2s^2 2p(2P^\circ)3p(^1P)$-$2s^2 2p(^2P^\circ)3d(^1D^\circ)$
	460.14	$(3s^3P^o$–$3p^3P)$
	464.30,	$2s^2 2p(^2P^\circ)3s(^3P^o)$ - $2s^2 2p(^2P^\circ)3p(^3P)$;
	480.32	$2s^2 2p(^2P^\circ)3p(^3D\ )$-$2s^2 2p(^2P^\circ)3d(^3D^\circ)$
	499.43	$2s^2 p^2(^4P)3s(^5P)$-$2s^2 p^2(^4P)3p(^5P^\circ)$
N III	463.41	$2s^2 3p(^2P^\circ)$- $2s^2 3d(^2D)$

Table 2.2 Identified atomic transition lines for laser ablated Al plasma in N_2 ambient

The emission spectra of laser ablated ZnO plasma was recorded in the range of 300 – 850 nm at 10^{-1} mbar O_2 pressure, 5 mm distance from the target surface and 3×10^{11} W/cm^2 laser irradiance is shown in Figure 2.6. The identified transition lines of Zn I, Zn II, and O I are listed in Table 2.2. Out of these identified lines, some selected lines were used for electron temperature estimations. Electron temperature was estimated using Boltzmann equation [Eq. 1.3] and Saha-Boltzmann equation [Eq. 1.4] by measuring intensity ratios of the transition lines of the same ionization state and of the successive ionization states of selected species, respectively.

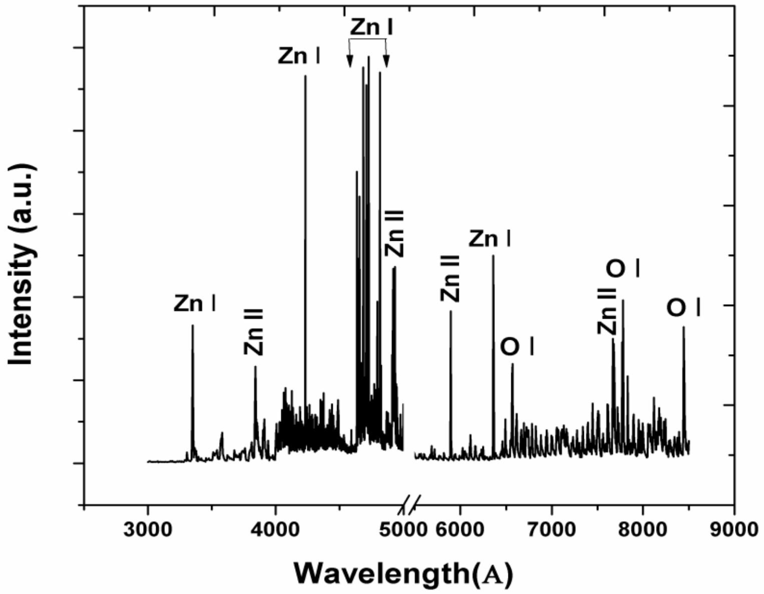

Figure 2.6 Emission spectra of laser ablated ZnO plasma in 0.1 mbar oxygen ambient

Transition	Wavelength (nm)	Configurations
Zn I	334.50	--
	396.54	--
	429.28	--
	460.00	--

	472.21	--
	480.05	--
	636.23	--
Zn II	384.02	--
	491.16	--
	430.00	--
	589.43	--
	747.78	--
	761.29	--
	773.25	--
O I	660.49	--
	777.19	3s($^5P^o$)-3p(^5P)
	799.50	3p(^3P)-3s($^3D^o$)
	822.18	3s($^3D^o$)-3p(^3D)
	844.63	3s($^3S^o$)-3p(^3P)

Table 2.3 Identified atomic transition lines for laser ablated ZnO plasma in O_2 ambient

For electron number density estimation, a well resolved line from the emission spectra was selected and re-scanned with the step size of 0.05 nm and 2s integration time within 2-5 nm wavelength interval. With the variation in deposition parameters, broadening in transition lines (stark broadening) was measured. Electron number densities were then calculated by using Eq. 1.7.

The molecular band spectra of AlN (0-0 system of $^3\pi$-$^3\pi$ transition at 507.8 nm) [133] and O_2 (Schumann-Runge system at 351.7 nm) [134] were recorded in the wavelength intervals of 5-10 nm around the respective peak.

2.5 Hydrothermal Growth of ZnO Nanorods

ZnO is known to have very high room temperature excitonic binding energy (60 meV) which can be used for room temperature laser action in ZnO nanostructures [98, 135, 136]. The well aligned ZnO nanorods were shown to be most promising for such applications [85]. In order to study the photo excited lasing action in such nanorods, vertically aligned ZnO nanorods were grown using a hydrothermal method [137].

For hydrothermal growth of ZnO nanorod arrays, 0.1 M precursor solution of Zinc Nitrate Hexahydrate [$Zn(NO_3)_2.6H_2O$] and Hexametheylenetetramine (HMT or Hexamine) in distilled water (H_2O) were prepared separately. Then 25 ml of each solution was mixed together in a borosil glass bottle. As a preheating process, the bottle was sealed and heated to 95^{o}C for 2-10 hrs. After preheating process, pulsed laser deposited ZnO thin films on fused silica substrates were immersed in the solution. The films were placed in an inclined position against the wall of the bottle with seed ZnO thin film facing down. The bottle was then sealed and heated at a constant temperature of 95^{o}C for 6-18 hrs for the growth of nanorods. The as-grown ZnO samples were thoroughly rinsed in deionized water and then annealed in air by heating up to 200^{o}C for 4 hrs.

2.6 Characterization of Thin Films

For the structural characterization of the AlN, TiO_2 and $Zn_{1-x}Mg_xO$ ($0 \leq x \leq 0.7$) thin films, XRD [Seifert 3003 T/T] technique was used. XRD measurements were performed in the grazing incidence angle mode (5^o) using 0.154 nm wavelength of Cu K_α. AFM imaging [NT-MDT Smena] was performed in tapping mode for surface morphological characterization of the thin films. The rms roughness and average grain sizes were also estimated using AFM analysis. Height histograms of the scanned AFM images were used to estimate average grain sizes using “Grain Analysis” program (provided by NT-MDT Co., Russia). To further investigate the surface morphology of the thin films, SEM imaging [Leo 1403vp] was performed. Thin films were gold coated using thermal evaporation technique prior to be inserted inside the vacuum chamber for the SEM imaging. Carbon tapes were used to mount the thin films on the sample stage. Cross-sectional SEM imaging of the films was performed to estimate the film thickness. The atomic composition of the thin films was determined using the EDX [Inca Oxford Instruments] technique attached with SEM. For the lattice structure characterization of ZnO NRs, TEM images were recorded using JEOL JEM 2000 fitted with Gatan image filter. For the bandgap determination of AlN, TiO_2 and $Zn_{1-x}Mg_xO$ ($0 \leq x \leq 0.7$) thin films, UV-VIS spectra was recorded in transmission mode [Shimadzu UV 3600] as well as reflection mode [Varian-Cary 50 Bio]. Photoluminescence spectra of the thin film samples were measured using PL spectrometers [Thermo Spectronic Aminco Bowman Series 2 and Edinburgh Instruments FLS 720p]. Micro Raman spectrometer [Horriba Jobin Yvon LabRAM HR] was used for lattice structure characterizations of ZnO and Mg-doped ZnO thin films.

2.7 Multiphoton Absorption Induced Laser Action in ZnO NRs

The experimental setup was assembled to record Multiphoton Absorption **(**MPA) induced lasing action in ZnO NR samples is shown in Figure 2.7. Fundamental (1064 µm) output of a Q-switched Nd:YAG laser (8 ns) was used as a excitation source (pump beam). The pump beam was focused on to the ZnO NR samples using a 30 cm focal length cylindrical lens at an incidence angle of about 30^o. This ultraviolet laser radiation, emitted as a result of 3-photon absorption induced emission, was imaged with a lens of 10 cm focal length on to the entrance slit of monochromator interfaced with a computer. The monochromator was scanned in the spectral range of 350 nm – 600 nm for different irradiance of the pump beam.

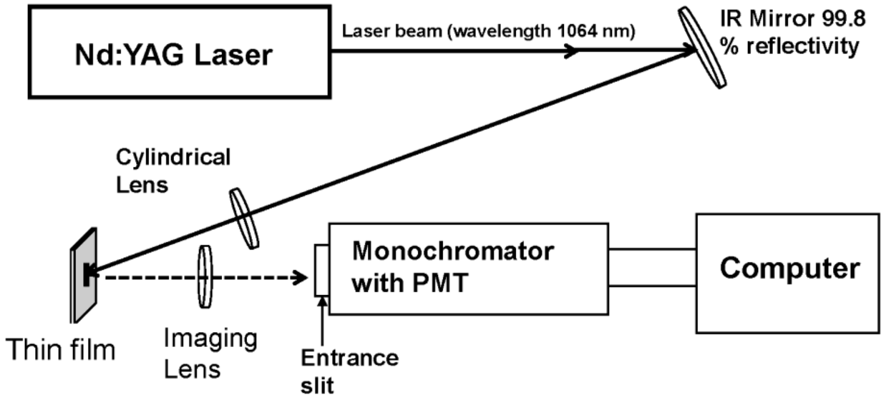

Fig. 2.7 Experimental setup for MPA induced random lasing action in ZnO thin films

2.8 Harmonic Generation in ZnO nanords and $Zn_{1-x}Mg_xO$ ($0\leq x\leq 0.7$) thin films

ZnO and ZnO based compounds possesses attractive non-linear properties that make them ideal candidate for frequency up-conversion based opto-electronic devices [88-92]. To study the second and third harmonic generation in pulsed laser deposited ZnO thin film, ZnO NRs and Mg-doped ZnO thin films on fused silica and quartz substrates, the same setup shown in Figure 2.7 was used. The monochromator was scanned in the range of 300 nm to 600 nm to record the THG at 355 nm, SHG at 532 nm and green band emission in the range of 540 nm to 580 nm.

2.9 Z-Scan Measurements for ZnO nanorods and $Zn_{1-x}Mg_xO$ ($0\leq x\leq 0.7$) thin films

To measure the non-linear absorption co-efficient, a single beam open z-scan technique employing two photon absorption (TPA) process was used [138]. A setup shown in Fig. 2.8 was assembled for this purpose. In this technique, second harmonic (532 nm) of 8 ns Nd:YAG laser was focused on to the $Zn_{1-x}Mg_xO$ ($0\leq x\leq 0.15$) thin films or ZnO nanorod samples positioned on motorized translation stage and the transmitted signal was recorded in the far field using a photo diode (PD1).

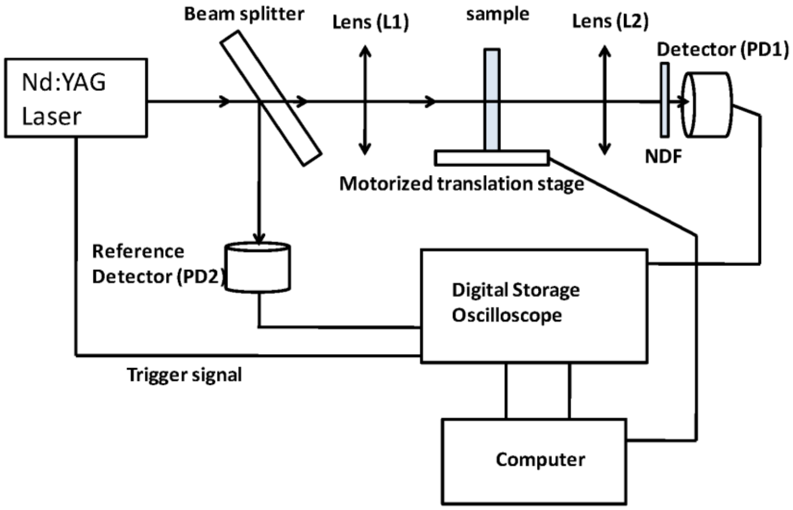

Fig. 2.8 Open Z-scan setup used for measurement of nonlinear absorption in thin films

ZnO thin films samples were translated along z-axis around the focal plane of focusing lens as shown in Fig. 2.8 in a step of 0.1 mm and corresponding transmitted signal was recorded on PD1 after focusing with another lens of 10 cm focal length. A neutral density filter was placed in front of PD1 to avoid the saturation of the photodiode. A reference signal from the incident laser beam was recorded on PD2 by using a beam splitter to compensate for fluctuations in laser beam on shot to shot basis. By fitting the open z-scan traces using eq. 2.5 [138], non linear absorption coefficient (β) for ZnO and $Zn_{1-x}Mg_xO$ ($0<x\leq 0.15$) thin films have been obtained.

For a temporally Gaussian pulse having FWHM pulse duration *t*, time integrated normalized energy transmittance through the sample in case of open aperture z-scan (S = 1) will be given by [139],

$$T(z,S=1)=\frac{1+\left(\frac{z}{z_0}\right)^2}{\sqrt{\pi}\beta L_{eff} I_0}\int_{-\infty}^{\infty}\ln\left[1+\frac{\beta L_{eff} I_0 \exp(-t^2)}{1+\left(\frac{z}{z_0}\right)^2}\right]dt \tag{2.1}$$

where z is the position of sample during scanning, z_o is Rayleigh length, β is the TPA coefficient, L_{eff} is the effective sample length and I_0 is the peak irradiance on the optic axis at the focus within the sample.

The effective sample length L_{eff} can be estimated using,

$$L_{eff}=\frac{1-\exp(-\alpha L)}{\alpha} \tag{2.2}$$

where α is the linear absorption coefficient of the sample which was estimated from the absorption spectra of the samples (Chapter 5). For pure ZnO thin film, α was experimentally found to be ~ 1.5×10^4 cm^{-1} at 532 nm. L is the actual film/sample thickness estimated using cross-sectional SEM imaging. The Rayleigh length z_o is given by,

$$z_0=\frac{\pi w_0^2}{\lambda}\approx 3.1\text{ mm} \tag{2.3}$$

where w_o is the beam diameter at the focus (z=0) which was calculated using the relation,

$$w_0 = \frac{f\lambda}{D} \approx 22.9\ \mu\text{m} \tag{2.4}$$

where f is the focus length of lens L1 (= 25cm), D is the laser beam diameter at lens (≈ 5.8 mm) and λ is the laser wavelength (= 532 nm).

For first order approximation, solution of eq.2.1 (for negligible non linear phase change $\Delta\phi<<1$ and far field condition $d >> z_0$, where d is the distance between sample and detector PD1), the normalized transmittance through the sample is given by [139, 140],

$$T = 1 - \frac{\beta I_0 L_{eff}}{(2)^{3/2}[1+(z/z_0)^2]} \tag{2.5}$$

The transmittance T was measured from the ratio of PD1 and PD2 signals as a function of z and normalized w.r.t. transmittance at $z>>z_0$. The normalized transmittance data was fitted using eq. 2.5 to estimate the value of non-linear absorption co-efficient β.

To estimate the value of non-linear refractive index n_2, a close z-scan setup (Fig. 2.9) was assembled. It is similar to open z-scan setup except an aperture was inserted in between sample and lens L2. The first order solution for the normalized transmittance through the sample under close z-scan is given by [139],

$$T = 1 - \frac{4\omega\beta n_2 I_0 L_{eff}(z/z_0)}{c[(z/z_0)^2+1][(z/z_0)^2+9]} \tag{2.6}$$

where ω is the angular frequency of laser, c is the speed of light and n_2 is the nonlinear refractive index.

The transmittance T was measured from the ratio of PD1 and PD2 signals (normalized w.r.t to transmittance at $z>>z_o$). Theoretical fitting of the transmittance data using eq. 2.6 was performed to estimate non-linear refractive index n_2.

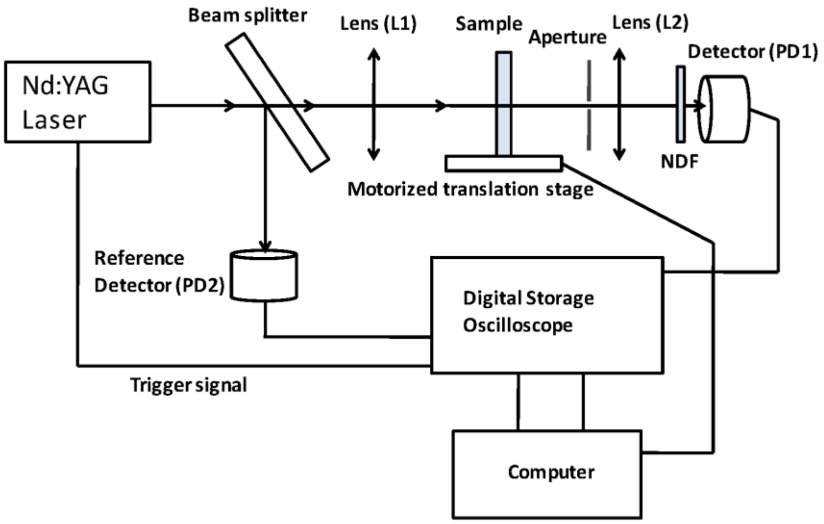

Fig. 2.9 Close Z-scan setup used for measurement of nonlinear refractive index of thin films

Further real and imaginary part of third-order susceptibility $\chi^{(3)}$ was obtained using relation 2.7 and 2.8. Finally $\chi^{(3}$ was estimated using eq. 2.9 [141].

$$\mathrm{Im}(\chi^{(3)}) = \frac{n_o^2 c^2 \beta}{240\pi^2 \omega} \qquad \text{(esu)} \tag{2.7}$$

$$\mathrm{Re}(\chi^{(3)}) = \frac{n_o^2 c n_2}{120\pi^2} \qquad \text{(esu)} \tag{2.8}$$

$$\chi^{(3)} = \sqrt{[\mathrm{Re}(\chi^{(3)})]^2 + [\mathrm{Im}(\chi^{(3)})]^2} \tag{2.9}$$

where n_o is the linear refractive index.

Chapter 3

Pulsed Laser Deposition and Characterization of AlN Thin Films

High quality AlN thin films are finding multifold of applications in the semiconductor industry [71, 142, 143]. AlN has a wide band gap (6.2 eV), high thermal conductivity (320 W.m^{-1}K^{-1}), high resistivity (10^{13} Ω/cm^{2}) and exhibits a negative electron affinity [80]. It exhibits piezo-electric properties and is widely used in surface acoustic wave (SAW) devices for high frequency sensor applications [78, 79]. It can be used as a light emitting device in the green-blue-UV spectral range and as UV photodetector [83, 84, 144].

In the present work, PLD technique was used for the deposition of AlN thin films using pure Al as a target. The main advantages of PLD technique include non-equilibrium growth, possibility of room temperature deposition due to high temperatures associated with the laser induced target plasma and direct film growth avoiding use of any harmful precursors. The crystal orientation of AlN flms deposited via PLD depends upon deposition parameters and properties of laser ablated plasma. For this reason, it is imperative to study the effect of N_2 pressure, deposition time, and substrate temperature as well as laser induced target plasma dynamics in N_2 ambient, on the structural, morphological and optical properties of AlN thin films.

3.1 Experimental Details

The PLD setup used in the present work to deposit AlN thin film is shown in Fig.2.1 (Chap.2, Sec. 2.3). The laser beam was focused using a lens (35 cm focus length) onto the metal Al target to a spot size of 3.08×10^{-5} cm^2 (spot size was measured using SEM) in N_2 ambient with in the pressure range of 10^{-2} to 10^2 mbar. The ultra sonically cleaned single crystalline p-type Si (100) wafers placed parallel to and 3 cm apart from the target were used as substrates. The deposition time was varied in the range of 20 to 60 min at room temperature. In order to study the effect of plasma dynamics on to the quality of pulsed laser deposited thin film, spatial evolution of emitted spectrum from plasma was recorded to estimate the plasma temperature and electron density (Sec 1.3 and 2.4).

3.2 XRD measurements

XRD measurements confirmed that the thin film of AlN in (002) orientation can be efficiently deposited via PLD at certain optimized laser intensity, target-substrate distance, and the background N_2 pressure. Fig. 3.1 (a) shows the XRD pattern of PLD thin films of AlN deposited at laser intensities of 4.3×10^{11} W/cm^2, 6.4×10^{11} W/cm^2 and 8×10^{11} W/cm^2, keeping the target distance and background pressure fixed at 3 cm and 0.05 mbar, respectively. It clearly shows the formation of (002) oriented AlN film in single phase at laser intensity of 8×10^{11} W/cm^2 with a weak appearance of pure Al phase. Above this intensity, the deposition of liquid droplets of ablated Al was observed on to the substrate. At the laser intensity of 6.4×10^{11} W/cm^2 there was a weak appearance of AlN in (100) orientation along with pure Al phase. Though at lower intensities, Al was ablated as is obvious from the appearance of pure Al phase in XRD of Fig. 3.1. (a) (Plot A) but the reactive plasma dynamics condition in laser induced breakdown was not sufficient for the formation of molecular AlN. Thus it can be concluded that optimum laser intensity for the present experiment was 8 × 10^{11} W/cm^2 and rest of the studies were confined at this optimum value of laser intensity.

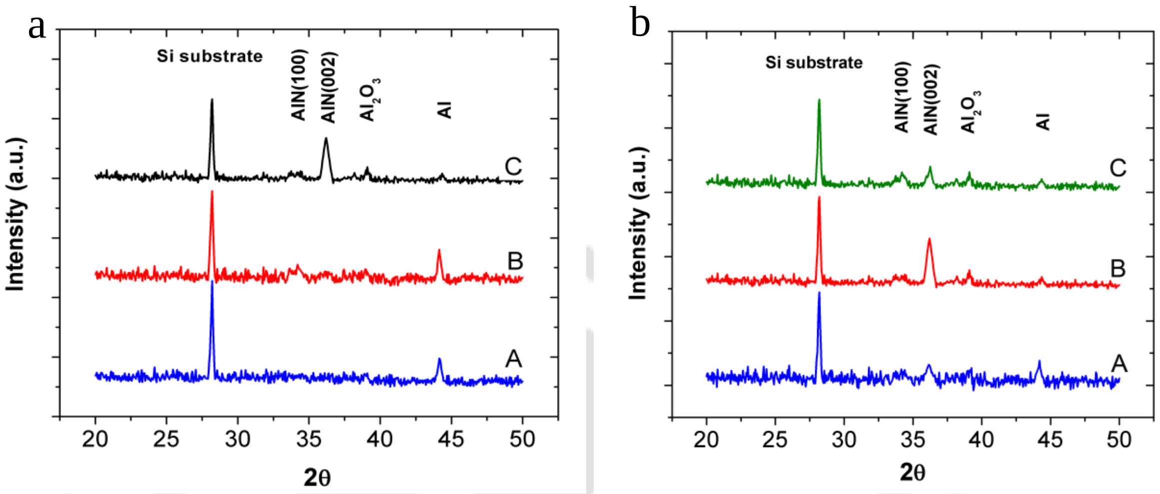

Figure 3.1 XRD pattern of AlN thin films deposited at (a) three different laser irradiances[A - 4.3 × 10^{11} W/cm^2, B - 6.4 × 10^{11} W/cm^2, C - 8 × 10^{11} W/cm^2] (Target substrate distance 3 cm and N_2 pressure 5 × 10^{-2} mbar); (b) three target substrate distances [A- 2 cm, B- 3 cm, C- 4 cm] (laser irradiance 8 × 10^{11} W/cm^2 and N_2 pressure 5 × 10^{-2} mbar)

Fig. 3.1 (b) shows the XRD pattern of AlN thin films deposited at three different target-substrate distances [A (2 cm), B (3 cm) and C (4 cm)] at 8 × 10^{11} W/cm^2 laser irradiance and 5 × 10^{-2} mbar N_2 pressure. Maximum intensity of AlN (002) peak was observed for films deposited at 3 cm distance. At target-substrate distance lower than 3 cm, intensity of AlN (002) peak decreased rapidly, and intensity of Al peak increased. This can be attributed to re-sputtering of adatoms from the film surface due to impingement by high energy electrons near the target surface. For the films deposited at larger distances (4 cm), intensity of both AlN (002) and Al peaks decreased, probably due to falling of the laser ablated plasma density as a result of expansion. Hence, the target-substrate distance was fixed at the optimum value of 3 cm for rest of the experiment.

XRD measurements for AlN thin films deposited in N_2 ambient in the pressure range of 5×10^{-2} mbar to 100 mbar are shown in Fig.3.2. At the higher pressure (100 mbar and 10 mbar), pulsed laser deposited AlN thin films were highly (101) oriented. With decrease in pressure there was a gradual shift from (101) orientation to (002) orientation.

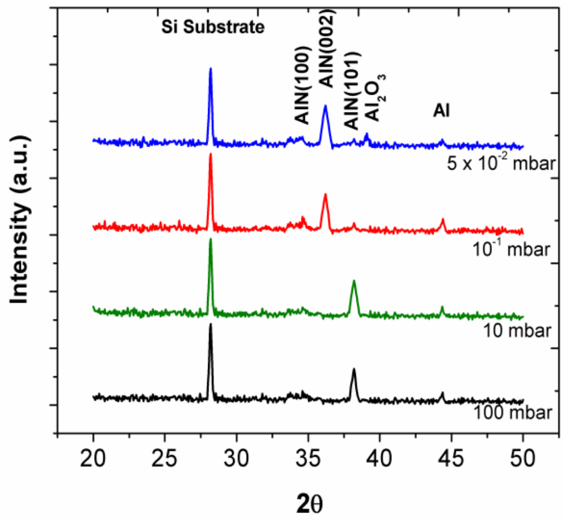

Figure 3.2 XRD pattern for AlN films deposited on to Si (100) substrates at different N_2 pressure (target substrate distance 3 cm and laser irradiance 8×10^{11} W/cm^2)

XRD measurements for the films deposited at low N_2 pressure (10^{-1} mbar and 5×10^{-2} mbar), showed the (002) preferred orientation of AlN thin films. The deposition of metallic Al and Al_2O_3 was also observed at low N_2 pressures ($\leq 10^{-1}$ mbar). Impurities such as oxygen play a major role at low ambient pressure leading to formation of Al_2O_3.

3.3 Surface Morphology (AFM/SEM analysis)

The AFM scans of AlN thin films deposited at various N_2 pressure is shown in Fig.3.3. Fig 3.3 (a) and (b) correspond to AlN thin films deposited at higher N_2 pressure of 100 mbar and 10 mbar respectively. It showed the formation of pebble like structure.

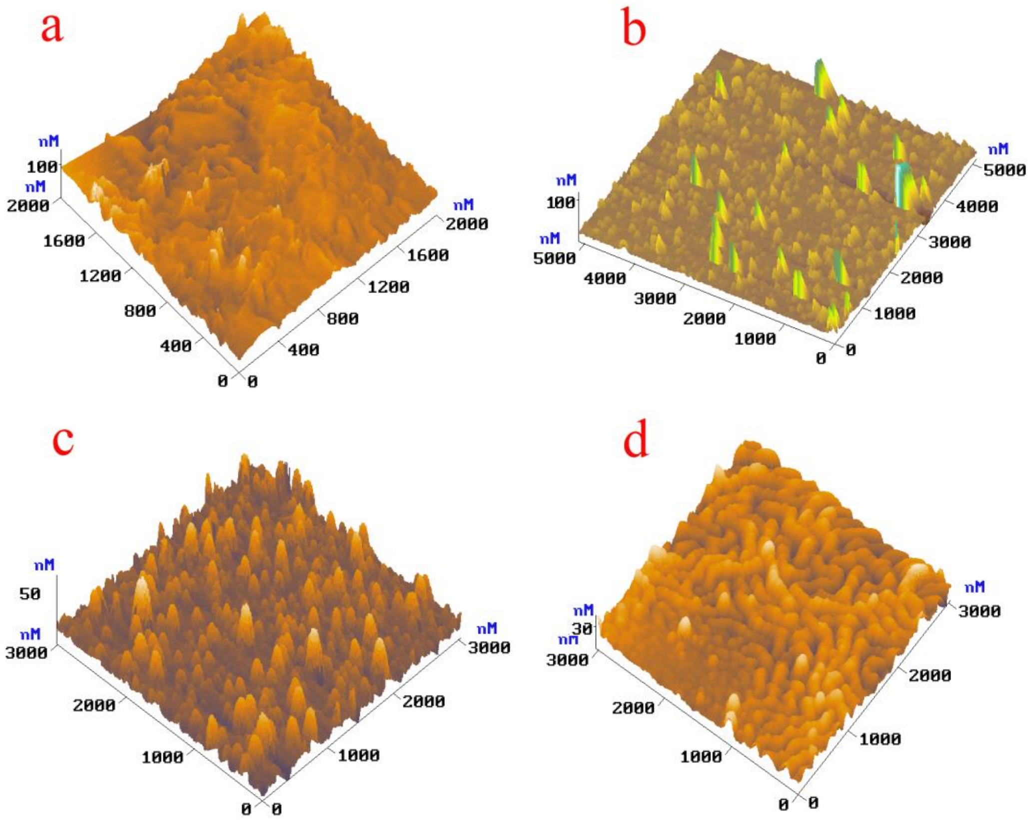

Figure 3.3 *AFM scanned images of AlN thin films deposited at various N_2 pressures; (a) 100 mbar (2 µm × 2 µm); (b) 10 mbar (5 µm × 5 µm); (c) 10^{-1} mbar (3 µm × 3 µm); (d) 5 × 10^{-2} mbar (3 µm × 3 µm)*

Fig.3.3 (c) and (d) corresponds to AFM scan of films deposited at lower N_2 pressure of 10^{-1} and 5 × 10^{-2} mbar respectively. The deposition at lower N_2 pressure confirmed the nano structured growth of AlN.

The increase in particle size with N_2 pressure was due to coagulation of particulates at higher pressure. Surface roughness of deposited AlN thin films decreased at lower N_2 pressure, from 150 nm rms value for AlN thin films deposited at 100 mbar N_2 pressure to 20-30 nm rms value for AlN thin films deposited at 5 × 10^{-2} mbar. This improved surface quality was due to more uniform expansion of plasma at lower N_2 pressure.

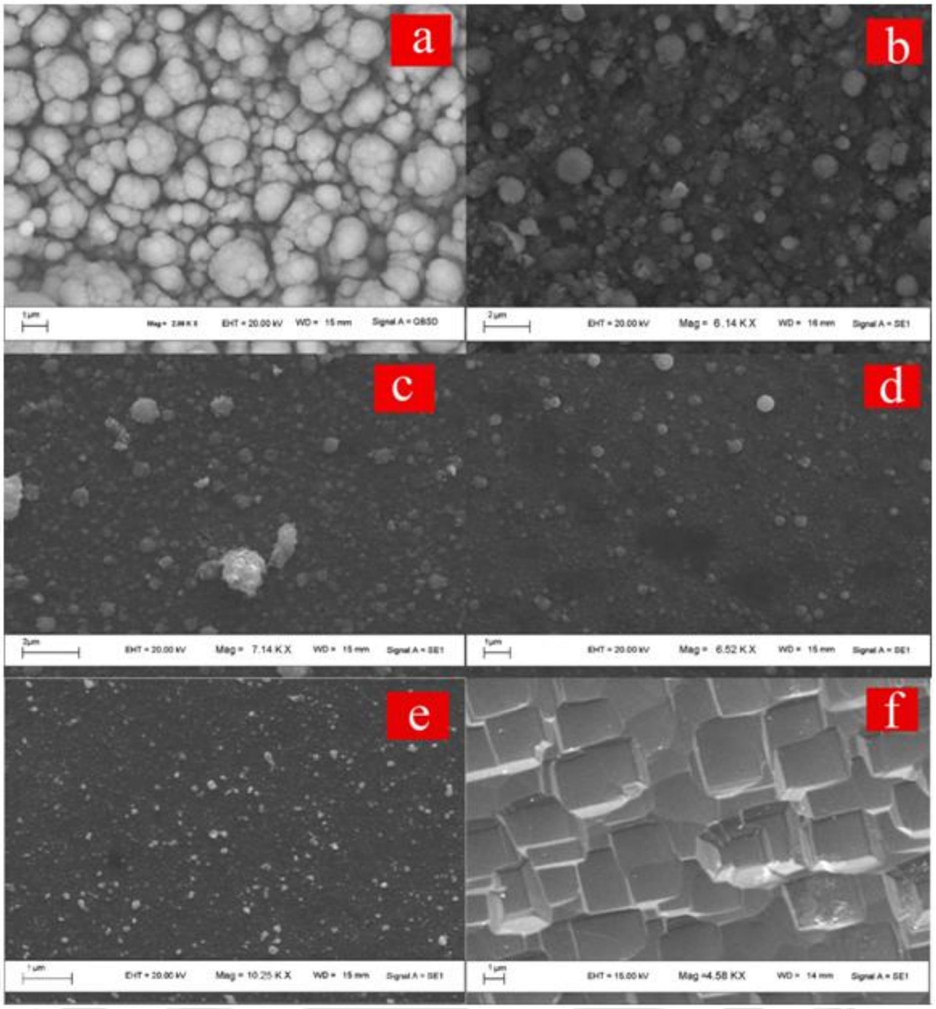

Figure 3.4 SEM images of AlN thin films deposited at various pressures; (a) 100 mbar; (b) 50 mbar; (c) 10 mbar; (d) 1 mbar; (e) 10^{-1} mbar ; (f) 5 × 10^{-2} mbar

SEM images for AlN thin films deposited at various N_2 pressure is shown in Fig.3.4. Fig 3.4 (a), (b) (c) and (d) corresponds to AlN thin films deposited at higher N_2 pressure, 100 mbar , 50 mbar, 10 mbar and 1 mbar respectively. Fig.3.4 (e) and (f) corresponds to scanning of films deposited at lower N_2 pressure, 10^{-1} and 5 × 10^{-2} mbar respectively.

Fig.3.5 (a) and (b) shows cross sectional images of AlN thin films deposited at 10^{-1} and 5 × 10^{-2} mbar N_2 pressure respectively, confirming the c-axis (002) columnar growth of AlN thin films. There was initial columnar growth observed at 10^{-1} mbar N_2 pressure [Fig. 3.5

(a)] that becomes prominent for AlN thin films deposited at 5 × 10^{-2} mbar N_2 pressure [Fig. 3.5 (b)]. Due to columnar growth at 5 x 10^{-2} mbar N_2 pressure, formation of smooth micro craters and hillocks can be observed on top surface of AlN thin films in Fig.3.4 (f). The thickness of pulsed laser deposited AlN thin films (deposition time – 60 mins) was measured to be 3.8 μm at 10^{-1} mbar and 3.2 μm at 5 × 10^{-2} mbar.

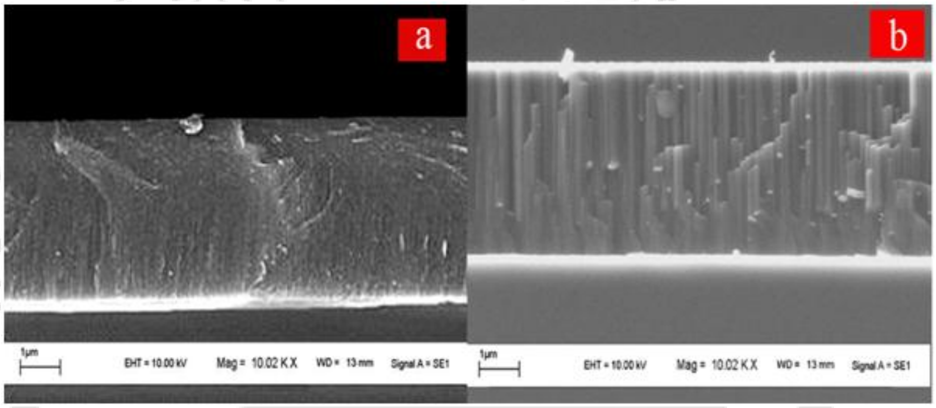

*

Figure 3.5 Cross-sectional SEM images of AlN thin films deposited at; (a) 10^{-1} mbar; (b) 5 × 10^{-2} mbar

The dependence of the roughness and orientation of the AlN thin film on N_2 pressure is most likely related to the collisions between the ablated species and nitrogen gas. At low N_2 pressure, mean free path of Al ions via laser ablated plasma was increased due to decrease in collisions with the ambient nitrogen species, hence particles in plasma can easily deliver their kinetic energy to the adatoms at the growing film surface. With the repeated laser shots for longer deposition time, atomic bombardment at the film surface caused the film densification by decreasing the voided regions in the microstructure as atoms with sufficient kinetic energy at the film surface may rearrange themselves under thermal equilibrium condition. Thus atomic mobility at the film surface was augmented due to the increase in energy transfer at the film surface. The wurtzite phase of AlN is more stable due to its close-packed stacking than the zincblende phase and possesses the lowest surface energy [145-147]. As a result, islands corresponding to the lowest surface energy can nucleate and grow in c-axis (002) orientation of wurtzite AlN as shown in Fig 3.4 (f). At higher pressures, increased number of collisions in gaseous phase may lead towards the AlN thin film growth in random orientations.

Further c–axis oriented AlN thin films grown by PLD at N_2 pressure of 5×10^{-2} mbar was found to have much better surface morphology compared with films deposited at much lower or higher pressure. There was no deposition of AlN below 10^{-2} mbar of N_2 pressure. Probably the laser intensity used in the present experiment was low enough so as not to dissociate/breakdown N_2 gas molecules below 10^{-2} mbar. Therefore one concludes that optimum N_2 pressure for deposition of (002) oriented AlN thin films at room temperature lies in the range of 10^{-2} mbar.

N_2 Pressure (mbar)	**Grain Size (nm)**		
	Scherer Formula XRD	SEM	AFM
0.05 mbar	110 nm ± 7 nm	128 nm ± 10 nm	120 nm ± 5 nm
0.01 mbar	145 nm ± 13 nm	162 nm ± 10 nm	138 nm ± 5 nm
10 mbar	187 nm ± 20 nm	196 nm ± 10 nm	178 nm ± 5 nm
100 mbar	210 nm ± 26 nm	240 nm ± 10 nm	201 nm ± 5 nm

Table 3.1 Variation of average grain size of pulsed laser deposited AlN thin films with N_2 pressure

Table 3.1 summarizes the average grain size distribution obtained from SEM imaging, AFM analysis and from XRD data using Scherer’s formula. From AFM analysis, average grain size was found to be increased with N_2 pressure, from 120 nm at 0.05 mbar to 200 nm at 100 mbar. Similar trend has been observed using SEM and XRD analysis.

3.4 Photoluminescence spectra of the pulsed laser deposited AlN thin films

Photoluminescence spectra of reactive pulsed laser deposited AlN thin films recorded using Photoluminescence spectrometer (Thermo-spectronic Aminco Bowman Series 2) with 250 nm excitation wavelength at room temperature is shown in Figures 3.6 (a) and (b). Fig.3.6 (a) shows the PL of AlN thin films deposited for 20 minutes at different pressures and Fig. 3.6 (b) shows that of AlN thin films deposited for different deposition time for deposition pressure of 100 mbar.

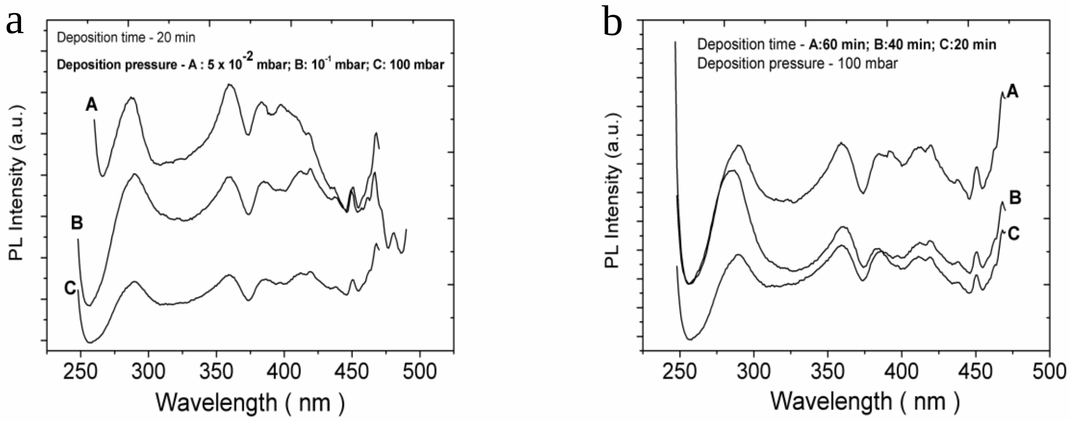

Fig. 3.6 Photoluminescence of AlN thin films deposited (a) at various N_2 pressure; (b) *with different deposition time*

A broad PL emission spectrum in the range from 270 nm to 471 nm was observed [145, 148] with major peaks around 286 nm (~ 4.33 eV) and 362 nm (~ 3.42 eV). The visible emission from AlN thin films was due to impurities and surface defects. The oxygen impurities would produce defects including oxygen point defects (O_N^+), nitrogen vacancies (V_N) and ($V_{Al}^{3-} - 3\times O_N^+$) defect complexes. Thus the visible emission may results from radiative recombination of a photo-generated hole with an electron occupying the nitrogen vacancies and/or from transition between the shallow level of V_N and deep level of $(V_{Al}^{3-} - 3\times O_N^{+})$ defect complexes [149-151]. Increase in PL intensity with decrease in N_2 pressure as shown in Fig.3.6 (a) was attributed to deposition of highly c – axis oriented films and nanostructured growth of AlN at low N_2 pressure. The increase in PL intensity with deposition time as shown in Fig.3.6 (b) was due to increase in film thickness for higher deposition time. Shift of emission peak (at 286 nm) towards higher wavelength region was observed with increase in deposition time and N_2 pressure. It may be attributed to development of local strain in the AlN film deposited at higher N_2 pressure and for longer deposition time which leads to non-uniform growth of the film.

3.5 FTIR spectra of the pulsed laser deposited AlN thin films

Fig.3.7 shows the FTIR transmission spectra of AlN thin films deposited via PLD. Graph A in Fig.3.7 shows FTIR spectra of AlN thin films deposited at 10^{-1} mbar of N_2 pressure and graph B shows that of at 100 mbar N_2 pressure. FTIR spectrum of Si (100) substrate is also shown by Graph C. The dominant absorption peak at ~ 674 cm^{-1} in FTIR spectra correspond to the AlN transverse optical [E_1(TO)] phonon mode [152, 153]. The peak at 611 cm^{-1} was due to Si substrate. AlN A_1(TO) mode was also expected at 610 cm^{-1} but not visible distinctly due to overlapping with Si peak. It was observed that FWHM of AlN [E_1(TO)] mode for films deposited at lower N_2 pressure is small compared to those deposited at higher pressure. This could have been due to increase in disorder at higher pressure. The FTIR spectra were in good agreement with the XRD and SEM results, which confirmed the formation of large AlN crystallites at high N_2 pressure.

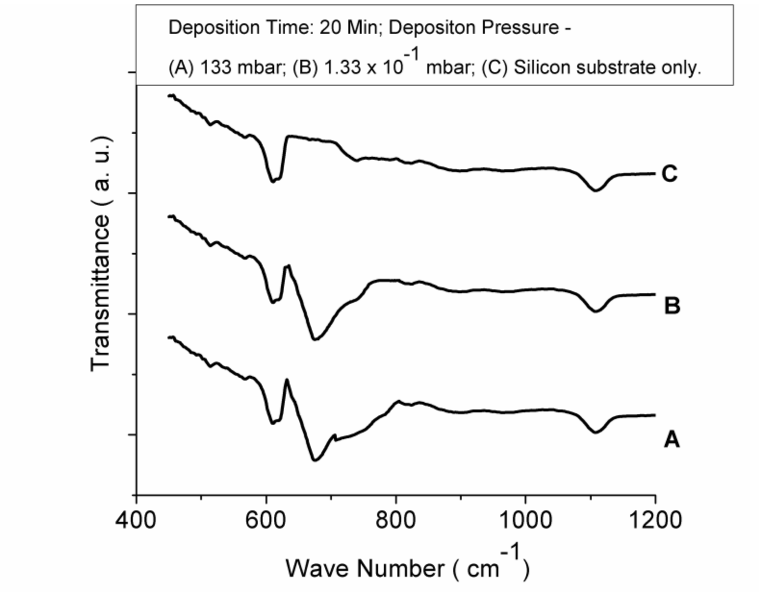

Figure 3.7 FTIR spectra of AlN thin films and Si substrate

3.6 Plasma dynamics studies of Al plasma during pulsed laser deposition of AlN thin film

In order to understand the effect of PLD parameters on the properties of AlN thin films, it was necessary to monitor and study the dynamics of laser induced target plasma during deposition.

In this section, plasma dynamics of laser induced Al plasma in ambient N_2 is presented. Further an attempt has been made to correlate the properties of pulsed laser deposited AlN thin films with the plasma parameters.

3.6.1 Emission spectroscopy of laser ablated Aluminium plasma and calculation of plasma parameters

The wavelength dispersed emission spectrum of the LIP plume during laser ablation of the Al target in 0.1 mbar N_2 pressure and recorded at a distance of 10 mm from the target surface is shown in Fig.2.4 (Chap.2). Strong emission lines corresponding to Al I, Al II, Al III, N I, N II and N III transitions were identified. In addition, the band spectrum of AlN was also observed. Fig.3.8 shows the AlN band spectra at 507.8 nm (0-0 band system of $^3\pi$-$^3\pi$ transition) [133] recorded at 3 cm distance from target surface in 0.05 mbar N_2 pressure and 8 × 10^{11} W/cm^2 laser irradiance.

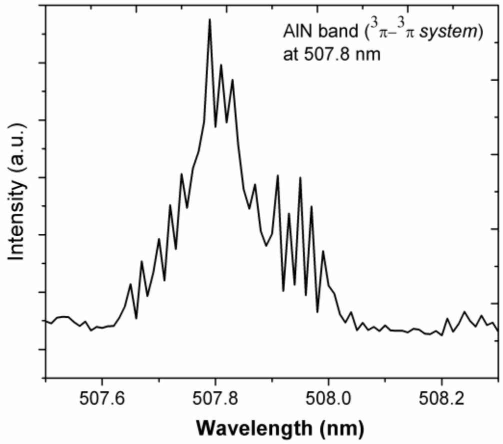

Figure 3.8 Band spectra of AlN in LIP of Al in N_2 pressure of 10^{-1}mbar, observed at 10 mm distance from target and laser irradiance of 8 × 10^{11} W/cm^2

The Al II and Al I (Fig.2.5 and Table 2.2) lines were used to estimate the electron number density and electron temperature, the two important parameters to understand the dynamics of laser induced plasma.

The electron temperature was estimated by using Saha-Boltzmann equation (eq. 1.4, Chapter 1, Sec 1.2.2.1). For this, the line intensities corresponding to emission lines of 466.30 and 396.15 nm, respectively, of Al II [$3p^2(^1D)$- $3s4p(^1P°)$] and Al I [$3s^23p(^2P°)$-$3s^24s(^2S)$] have been used. The electron number density was estimated from the FWHM, $\Delta\lambda_{1/2}$, of the stark broadened emission line of Al II at 466.3 nm, given by eq. 1.7 (Chapter 1, Sec 1.2.2.2). All other contributions like instrumental broadening, resonance broadening and Doppler broadening were found to be negligible and hence were ignored. The value of electron impact parameter W used for electron density calculations was taken from literature [54]. The optical data required for the above calculations were taken from literature and standard database [54, 154, 155].

3.6.2 Spatial Dependence of the plasma parameters

Fig. 3.9 (a) shows the variation of electron temperature and electron density as a function of distance from the target surface at N_2 pressure of 0.1 mbar and laser irradiance of 8 x 10^{11} W/cm^2. With laser ablated plasma expanding away from the target surface, the electron temperature has fallen down from 2.75 eV at 1 mm to 0.96 eV at 30 mm, while the electron density decreased from 1.57×10^{18} cm^{-3} at 1 mm to 4.7×10^{16} cm^{-3} at 30 mm.

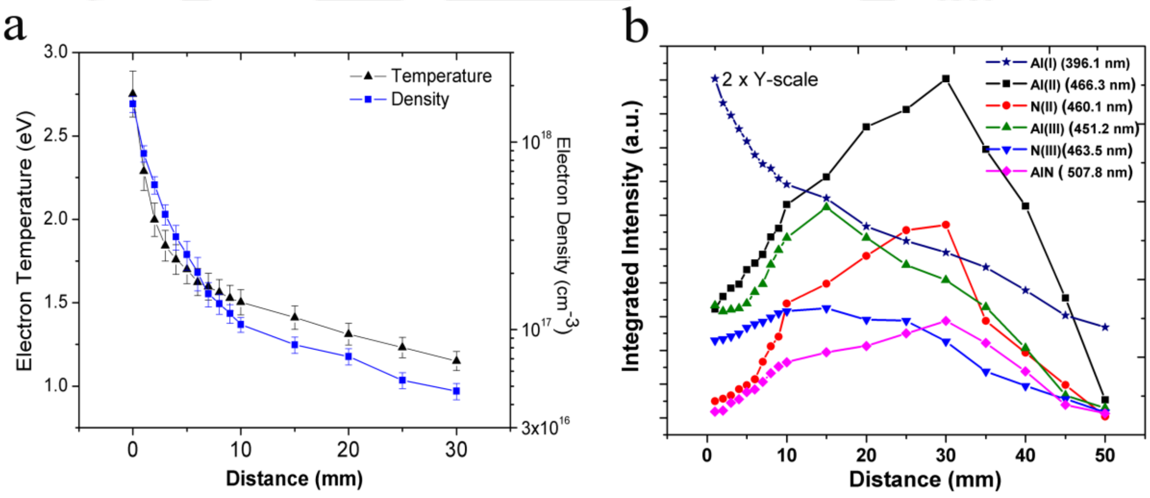

Figure 3.9 Spatial variation of (a) electron temperature and electron density; (b) integrated intensities of Al I, Al II, Al III, N II, N III transitions and AlN band [at 0.1 mbar N_2 pressure and 8 × 10^{11} W/cm^2 laser irradiance] (The integrated intensity of Al I neutrals is 2 times of the Y-scale value shown here)

The electron temperature as well as electron density showed rapid fall with distance from the target surface up to 6 mm. The variation of electron density as a function of distance (*z*) followed approximately a 1/*z* law at short distances, indicating that the initial expansion was one dimensional, which was in good agreement with an adiabatic expansion model [32].

This behavior was attributed to the three body recombination process taking place during the plasma expansion in ambient as well as formation of AlN. In three body recombination, during plasma expansion, local heating occurs through the release of ionization energy as electron and ions recombine to produce successive lower ionized species. This compensates the loss of energy due to adiabatic expansion and also into the formation of AlN [156]. Beyond 10 mm, the dependence of both the parameters on to the distance w.r.t. target is relatively weak. The fall in electron density was from 9.8×10^{16} cm^{-3} at 10 mm to 4.7×10^{16} cm^{-3} at 30 mm and that of electron temperature was from 1.56 eV to 0.96 eV over a distance of 10 mm to 30 mm. This was also supported by the increasing intensity of AlN with distance in the range of 10 mm to 30 mm from the target surface as shown in Fig. 3.9 (b).

Fig. 3.9 (b) shows intensity variation of AlI, AlII, NII, AlIII and NIII transitions along with AlN band at 507.8 nm. The intensity of the transitions, AlIII and NIII increased initially (<10 mm) due to multi-photon ionization process but for distances more than 15 mm from the target surface, rapid decrease in intensities was observed mainly due to recombination process which yield the lower ionization stages as well as formation of AlN molecule. The intensity of the transitions, AlII at 466.3 nm, NII at 460.1 nm amd AlN band was found to increase with distance up to 30 mm. This confirmed that the reaction between AlII and NII leads to the formation of AlN and maximum yield can be obtained at a distance of 30 mm from the target surface.

3.6.3. Dependence of electron temperature and plasma density on N_2 pressure

Fig. 3.10 (a) shows the variation of electron temperature and density with N_2 ambient pressure at a distance of 10 mm from the target surface and at a laser irradiance of 8×10^{11} W/cm^2. The presence of Al target lowers the breakdown threshold of N_2 gas because energetic electrons emitted from the target facilitate the dissociation of gas. Nearby the target surface, multi-photon ionization, inverse bremsstrahlung absorption and cascade ionization played crucial role as the incident laser energy was absorbed by the expanding plasma [157]. The density of free electrons can grow exponentially by electron impact (EI) ionization or Cascade ionization which is the dominant process in high ambient pressure. It leads to very high electron density (~ 10^{18} cm^{-3}) of laser ablated Al plasma at 100 mbar N_2 pressure, Fig. 3.10 (a).

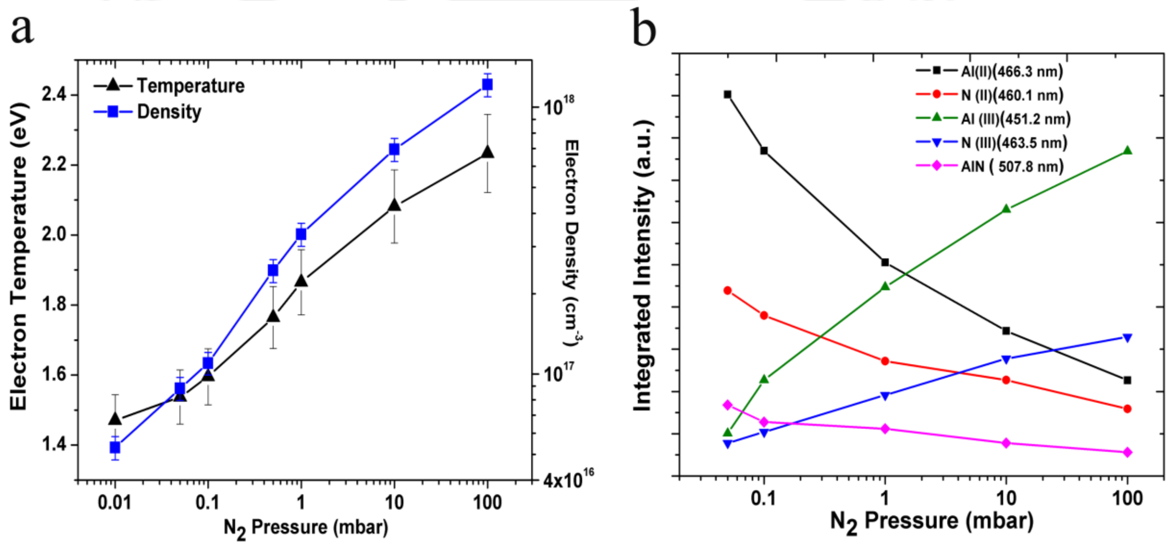

Figure 3.10 Pressure variation of (a) electron temperature and electron density and (b) integrated intensities of Al II, Al III, N II, N III transitions and AlN band [at 10 mm distance and 8 x 10^{11} W/cm^2 laser irradiance]

Fig. 3.10 (b) shows the intensity variation of ionized species Al II, N II, Al III, N III, and AlN band with N_2 pressure at an optimum distance of 3 cm from target surface and 8 × 10^{11} W/cm^2 laser irradiance. It is clear that intensities of Al II and N II decreased with increase in N_2 pressure and that of Al III and N III increased. Intensity of AlN band decreased marginally with increase in N_2 pressure. Therefore there was the deposition of AlN throughout this pressure range (5×10^{-2} mbar to 100 mbar) but (002) and (101) orientations dominated in different pressure regimes. Wurtzite AlN with (002) orientation have the lowest surface energy. In low N_2 pressure regime ($\leq 10^{-1}$ mbar), AlN thin films with (002) preferred orientation were deposited due to reactive recombination of Al II and N II ions which were formed via direct ionization and having low kinetic energy. While in the high pressure regime ($\geq$10 mbar), due to confinement of laser ablated plasma, cascade ionization played a dominant role leading to generation of highly energetic Al III and N III states [Fig. 3.10 (b)]. As the plasma further expanded, recombinative collision between free electrons and these ions (Al III and N III) took place which lead to lower ionization states, Al II and N II respectively, of higher kinetic energy. The recombination between such Al II and N II ions with high kinetic energies may be responsible for (101) oriented AlN formation which required higher surface energy compared to (002) orientation.

3.6.4 Dependence on the laser irradiance

The laser irradiance is an important factor in determining the efficiency of AlN formation via the recombination of different ionized species contained within the plasma. Fig. 3.11 (a) shows the variation of electron temperature and electron density of laser ablated Al plasma in N_2 ambient with laser irradiance. Sharp increase in both electron temperature and electron density was observed as the laser irradiance increased above 4.3×10^{11} W/cm^2.

Fig. 3.11 (b) shows the intensity variation of Al II, Al III, N II, N III transitions and AlN band with laser irradiance. Intensity of Al II and NII transitions increased with laser irradiance up to 8×10^{11} W/cm^2. The increase in AlN band intensity is more pronounced at ≥

6.4×10^{11} W/cm^2 laser irradiance. At low intensity, AlN molecule intensity was probably not enough for the film growth onto the substrate which was also confirmed by XRD, Fig 3.1 (a).

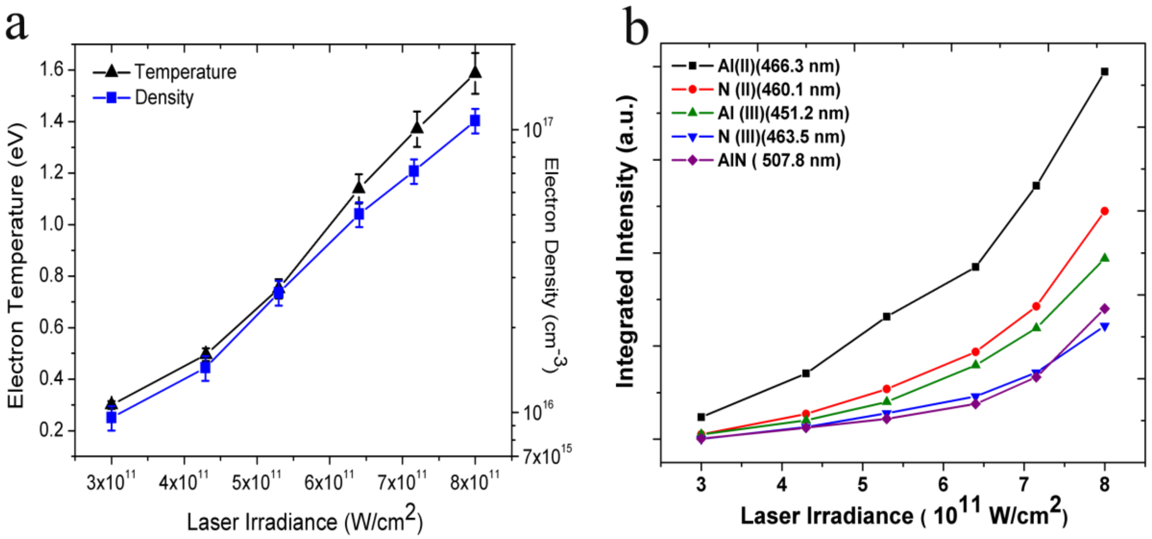

Figure 3.11 Variation with laser irradiance of (a) electron temperature and electron density; (b) integrated intensities of Al II, Al III, N II, N III transitions and AlN band [at 10 mm distance and 10^{-1} N_2 pressure

3.7 Conclusion

AlN thin films with c-axis orientation were deposited at room temperature using PLD technique. It was observed that orientation of deposited AlN thin films changed from (002) at low N_2 pressure (< 10^{-1} mbar) to (101) at high N_2 pressure (≥10 mbar). The optimum N_2 pressure, target substrate distance and laser irradiance for the deposition of (002) oriented AlN thin films were found to be 10^{-2} mbar, 3 cm and 8×10^{11} W/cm^2, respectively. The emitted spectra of LIP of Al in N_2 ambient consisted of Al II, Al III, N II, N III transitions and AlN band at 507.8 nm. The observation of AlN band confirmed the reactive recombination between Al and N ions to form molecular AlN. Electron temperature and electron density of the LIP of Al was estimated in the range of 1.2 – 2.1 eV and 4.5×10^{16} – 8×10^{17} cm^{-3}

respectively, with variation of N_2 pressure (10^{-2} – 100 mbar) at 30 mm distance from the target surface and 8×10^{11} W/cm^2 laser irradiance. From the parametric intensity variation of various ionic lines of LIP spectra, it was concluded that recombination of Al^+ and N^+ ions may be responsible for growth of AlN thin films with (002) preferred orientation and that of Al^{2+} and N^{2+} ions for AlN thin films with (101) preferred orientation.

One of the salient features of this chapter was the use of pure Al as the PLD target compared to that of AlN ceramic target for AlN thin film deposition [125, 152]. The Al target makes the PLD technique comparatively simple and cost effective. This is due to higher cost of AlN ceramic powder and subsequent tedious process to make oxygen free target for PLD.

Chapter 4

Pulsed Laser Deposition and Characterization of TiO_2 thin films

TiO_2 is an important n-type wide band gap (~ 3 eV), II-VI semiconductor with high refractive index and high dielectric constant [158, 159]. TiO_2 thin films have drawn a great deal of attention in recent years due to numerous applications in solar cells, photo catalyst, self cleaning windows [160-162], multilayer optical filter [163], anti reflection coating [164] and metal–insulator-semiconductor (MIS) devices [165]. Room temperature grown TiO_2 thin films can have three structural forms anatase (tetragonal), rutile (tetragonal) and brookite (orthorhombic). Annealing at temperatures between 300^0C to 800^0C initiates a transition from primary anatase to the rutile phase [166-168] as former being thermodynamically unstable.

Pulsed Laser Deposition (PLD) provides the easy manipulation of the properties of thin films of TiO_2 by controlling the deposition parameters [169-174]. The phase formation, morphology and microstructures and optical properties of pulsed laser deposited TiO_2 thin films depend onto oxygen pressure during deposition and post-deposition annealing temperature. The effect of ambient pressure on the microstructure of TiO_2 thin films deposited via PLD at high temperatures has been reported earlier [175, 176]. But for room temperature deposited TiO_2 thin films using PLD, the effect of ambient pressure and post-annealing is not well documented in the literature. In this chapter effect of ambient pressure and post-deposition annealing temperature on the properties of pulsed laser deposited TiO_2 thin films is discussed.

4.1 Experimental Details

TiO_2 thin films were deposited on to glass substrates in Ar and O_2 atmosphere at room temperature using the PLD setup [Chap.2, Sec. 2.3]. The sintered rutile TiO_2 was used as PLD target. The XRD and EDX spectra of TiO_2 target are shown in Fig. 4.1 (a) and (b), respectively. Only rutile phase diffraction peaks was observed in XRD spectra and an atomic ratio of 66.3:33.7 between Ti:O was confirmed by the EDX spectra. The substrate was placed at a distance of 3 cm from the target. The deposition time was kept fixed for 30 min for all the samples.

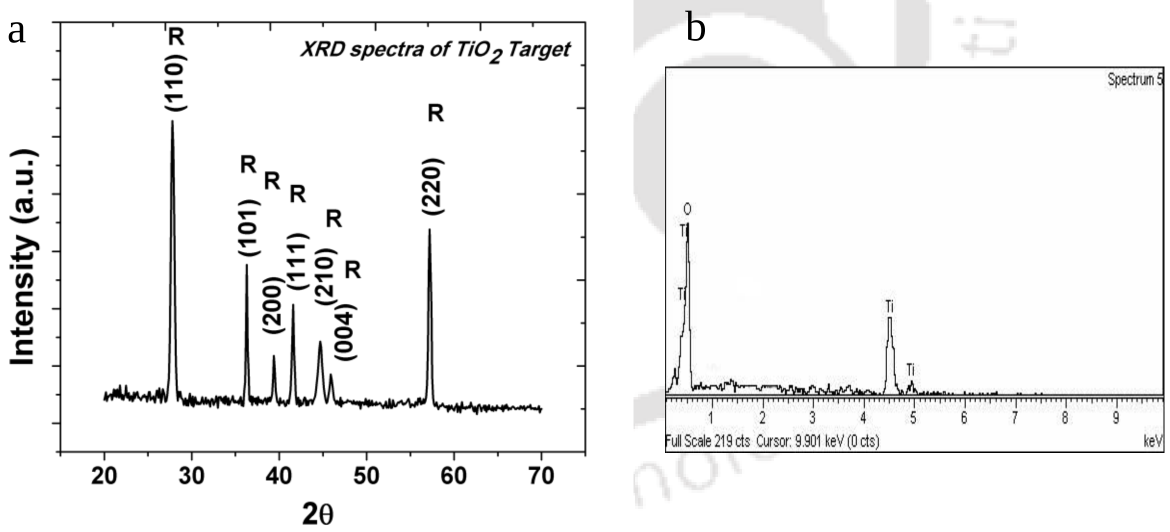

Figure 4.1 (a) XRD spectra of rutile TiO_2 target; (b) EDX spectra of rutile TiO_2 target

Laser irradiance on to the target surface was around 7 × 10^{10} W/cm^2. After deposition, TiO_2 thin films were annealed in a furnace (air ambient) for 6hrs at different temperatures in the range of 400 – 650^{o} C.

4.2 Effect of annealing and ambient pressure on the properties of pulsed laser deposited TiO_2 thin films

The effect of ambient (O_2 or Ar), pressure and post-annealing on the structural phase, optical properties and hydrophilic properties of TiO_2 films is presented in this section.

4.2.1 XRD spectra of TiO_2 thin films

Fig 4.2 (a) and (b) shows the XRD spectra of TiO_2 thin films deposited via PLD at room temperature in Ar ambient at 0.1 mbar and 1 mbar pressure, respectively. It can be observed that the as-deposited TiO_2 thin films were predominantly having amorphous anatase phase.

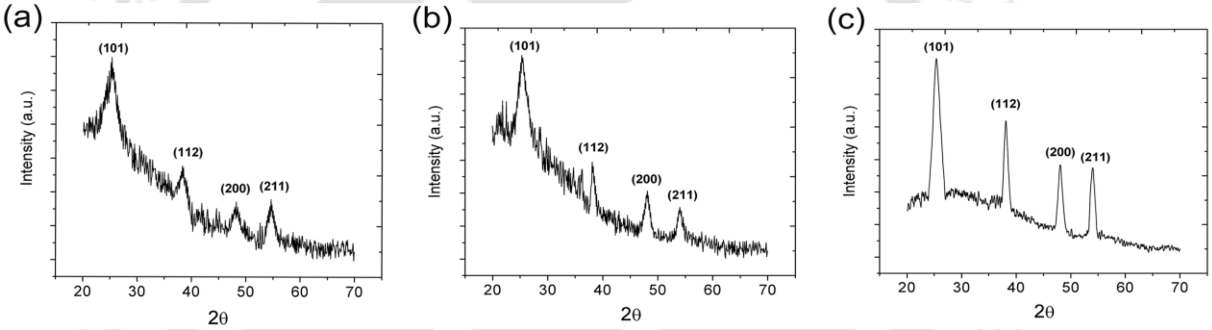

Figure 4.2 XRD pattern for room temperature deposited TiO_2 thin films at different Ar pressure (all the peaks correspond to anatase phase of TiO_2); (a) 10^{-1} mbar; (b) 1 mbar and (c) after annealing in air at 500^oC for films deposited at 1 mbar pressure

Broad FWHMs for anatase TiO_2 peaks corresponding to (101), (112) and (211) were observed. Due to highly amorphous nature of room temperature deposited films in Ar ambient, rutile phase was not observed even after annealing in air at 500^o C [Fig. 4.1 (c)]. After the annealing, TiO_2 films showed anatase phase only, with better crystallanity.

Figure 4.3 shows XRD pattern for PLD grown TiO_2 thin films deposited on glass substrate at room temperature at 10^{-1} mbar O_2 ambient with different annealing temperatures. In Figure 4.3 (a), it is clearly visible that as-deposited TiO_2 thin films showed mixed amorphous-crystalline nature with anatase phase. Fig.4.3 (b), (c) and (d) shows the effect of post annealing of the films at temperatures of 400^o C, 500^o C and 650^o C, respectively. With the increase in annealing temperature, crystallinity of the films was improved.

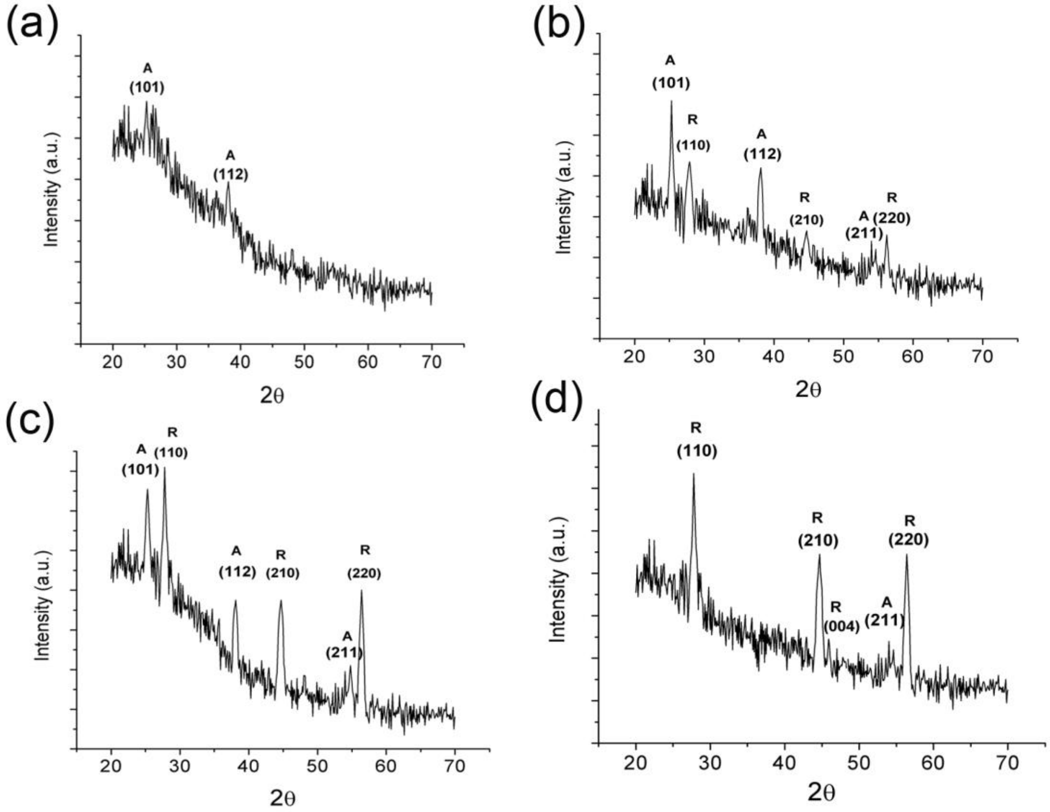

Figure 4.3 XRD pattern for TiO_2 *thin films deposited at* 10^{-1} *mbar* O_2 *pressure at room temperature; (a) as-deposited; and post- annealed at (b)* 400^oC *(c)* 500^oC *and (d)* 650^oC

At the annealing temperature of 400^o C, rutile phase started appearing as marked in Figure 4.3 (b). With further increase in temperature, rutile phase started dominating, Fig.4.3 (c) and at 650^oC almost complete phase transition has taken place from anatase to rutile, Fig. 4.3 (d), with corresponding dominant peaks of (110), (210) and (220) orientations.

Figure 4.4 shows XRD patterns of post-annealed (at 500^0C) TiO_2 thin films deposited at room temperature at different pressures of O_2 ambient.

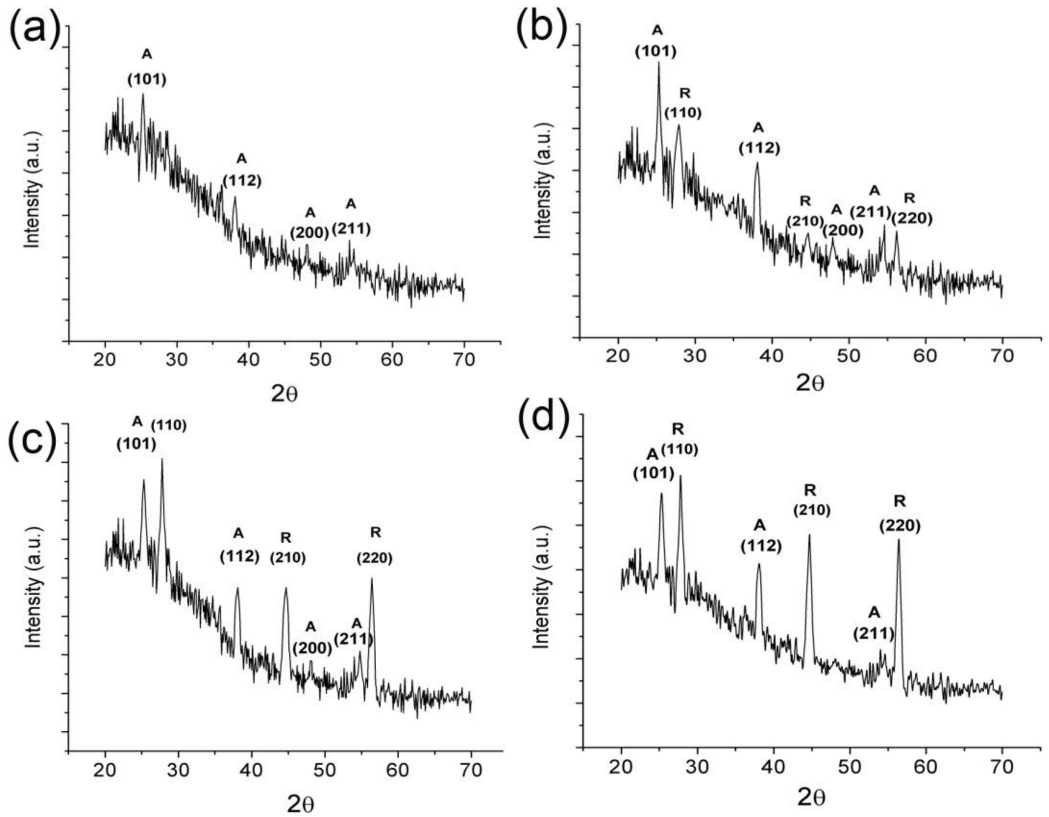

Figure 4.4 XRD pattern for 500^oC post-annealed TiO_2 thin films deposited at different O_2 pressure at room temperature; (a) 10^{-3} mbar (b) 10^{-2} mbar (c) 10^{-1} mbar (d) 1 mbar

It is clear from the XRD patterns that the crystalline nature of pulsed laser deposited TiO_2 films improved with increasing pressure of oxygen. TiO_2 films deposited at oxygen pressure of 10^{-3} mbar were having anatase phase. With the increase in O_2 pressure, rutile phase started emerging and at 1 mbar O_2 pressure, the films were predominantly having rutile phase, Fig. 4.4 (d).

4.2.2 Surface Morphology

Fig. 4.5 shows the SEM images and corresponding EDX spectra of pulsed laser deposited TiO_2 thin films in Ar ambient. The amorphous nature of films deposited at 0.1 and 1 mbar Ar pressure is clearly visible from Fig. 4.5 (a) and 4.5 (b), respectively. For the TiO_2 film deposited at 1 mbar Ar ambient, nanocone like structures appeared on film surface after annealing in air at 500° C, Fig 4.5 (c).

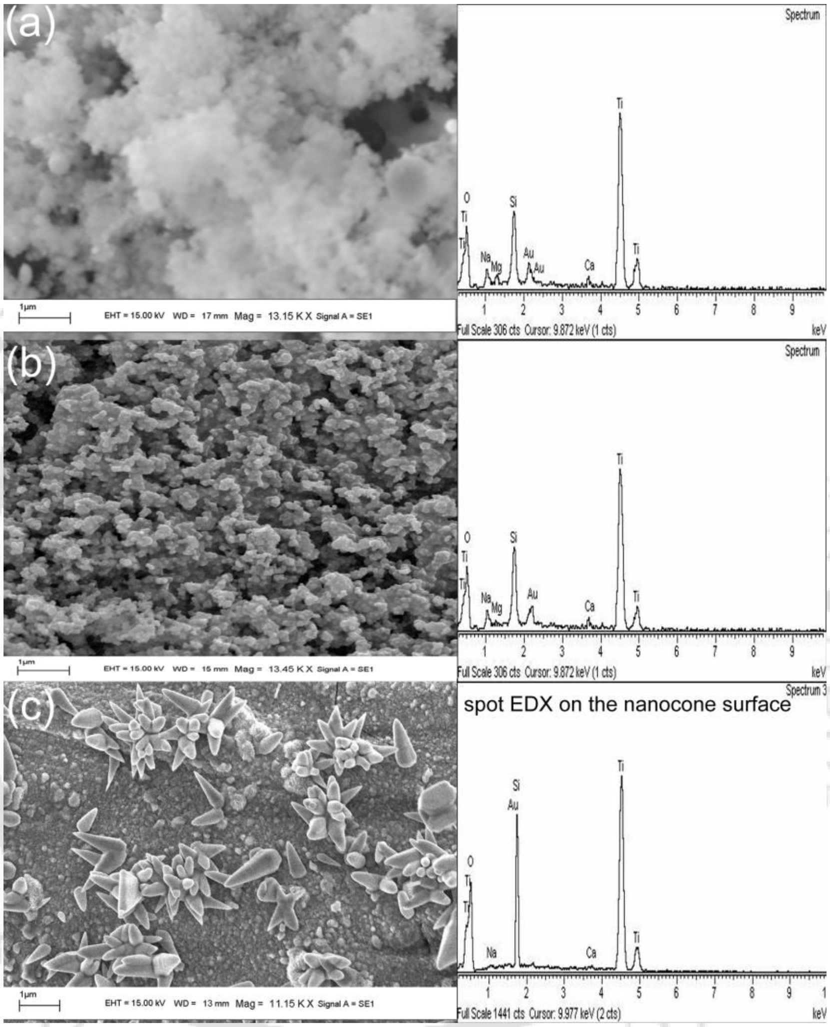

Figure 4.5 SEM image and EDX spectra of room temperature deposited TiO_2 thin films in Ar ambient at a pressure of (a) 10^{-1} mbar; (b) 1 mbar and (c) Annealed at 500°C after deposition at 1 mbar

The important difference was the stoichiometric ratio (Ti:O) and structural phase of the pulsed laser deposited TiO_2 films which was predominantly anatase as observed by XRD studies [Fig. 4.2 (c)]. The Ti:O ratio for unannealed thin films, deposited at 1 mbar Ar, Fig. 4.4 (b), was 40.4:59.6. During annealing in air, films absorbed oxygen, thereby improving the stoichiometric ratio (Ti:O = 37.9:62.1) for anatase nanocones which was still below the stochiometric ratio for rutile TiO_2 target, Fig 4.1 (b).

Figure 4.6 shows SEM images of pre- and post-annealed (at 650°C) TiO_2 thin films deposited at room temperature at 10^{-1} mbar O_2 ambient.

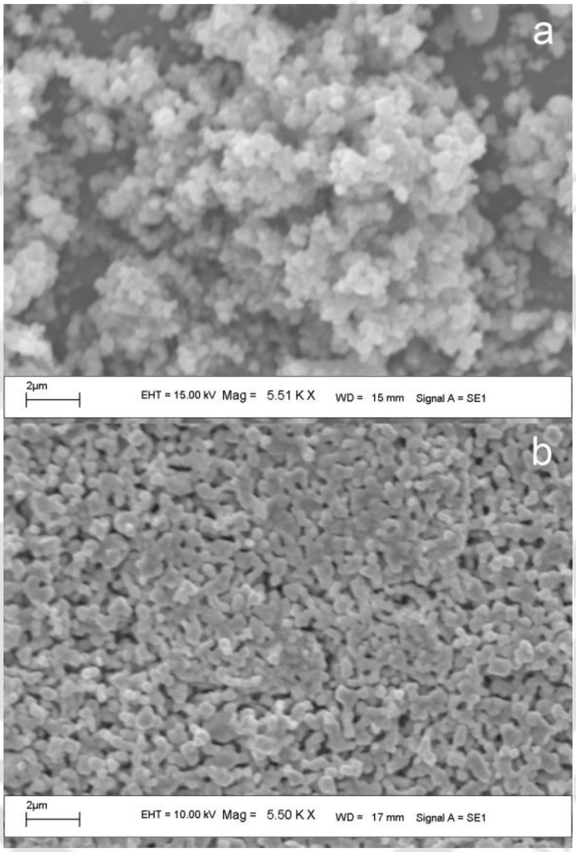

Figure 4.6 SEM image of room- temperature deposited TiO_2 thin films at 10^{-1} mbar O_2 pressure (a) as-deposited, (b) annealed at 650°C

Surface morphology of as-deposited TiO_2 thin film was amorphous like while post-annealing changed the surface morphology into crystalline structures.

Figure 4.7 (a) and (b) shows SEM images of post-annealed at 650°C TiO_2 thin films deposited at two different O_2 ambient pressures (10^{-3} mbar and 1 mbar respectively).

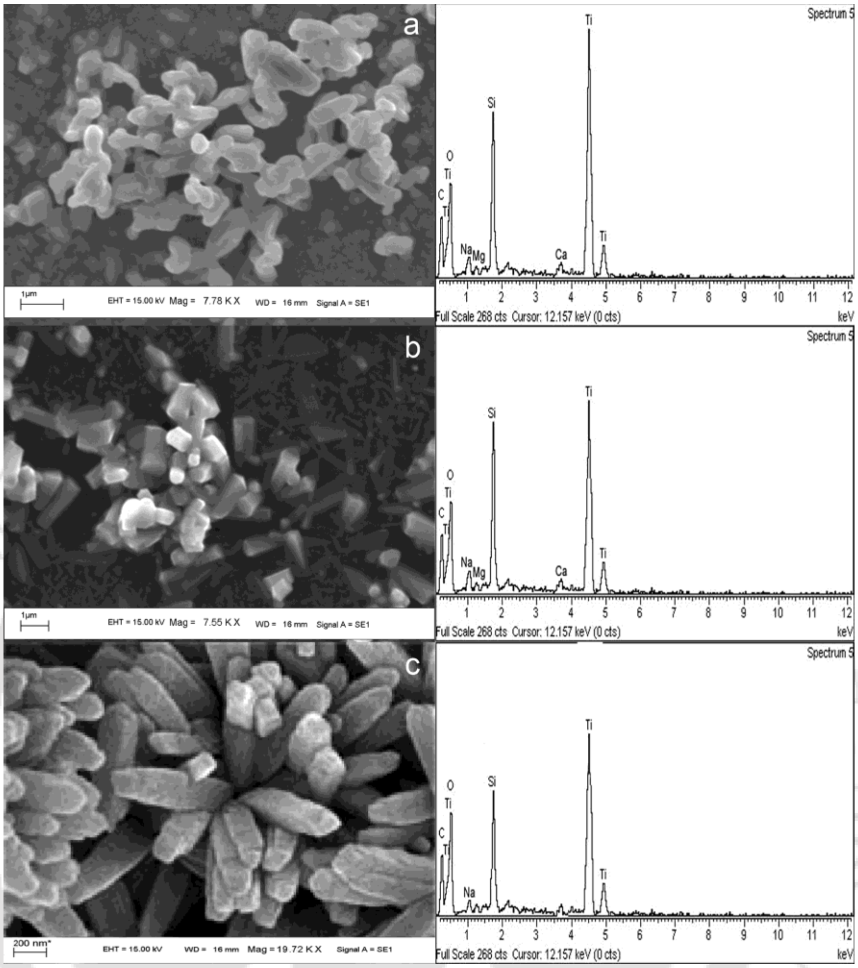

Figure 4.7 SEM image and EDX spectra of 650^{o}C post-annealed TiO_2 thin films deposited at (a) 10^{-3} mbar O_2, (b) 1 mbar O_2 pressure and (c) 1 mbar O_2 pressure (high resolution image).

High O_2 pressure favors the rod like surface morphology of crystalline TiO_2 thin films [Figure 4.7 (b)]. Fig. 4.7 (c) shows high resolution SEM image of TiO_2 nanorods arranged in flower like pattern, deposited at 1 mbar O_2 pressure.

From EDX spectra of Fig 4.7 (c), the average atomic percentage was found to be 33.2:66.8 (Ti:O) for TiO_2 nanorods which was very close to that of rutile TiO_2 target, Fig. 4.1 (b), confirming highly stoichiometric deposition.

Figure 4.8 (a) and (b) shows cross – sectional SEM images of room-temperature deposited TiO_2 thin films at 10^{-2} mbar and 1 mbar respectively. The film thickness was increased from 1340 nm to 2150 nm with increase in O_2 pressure from 10^{-2} mbar to 1 mbar, respectively. At high pressure of the background gas, the expansion of laser produced plasma was suppressed and hence the density of TiO_2 plasma propagating towards substrate was higher during PLD at higher O_2 pressures.

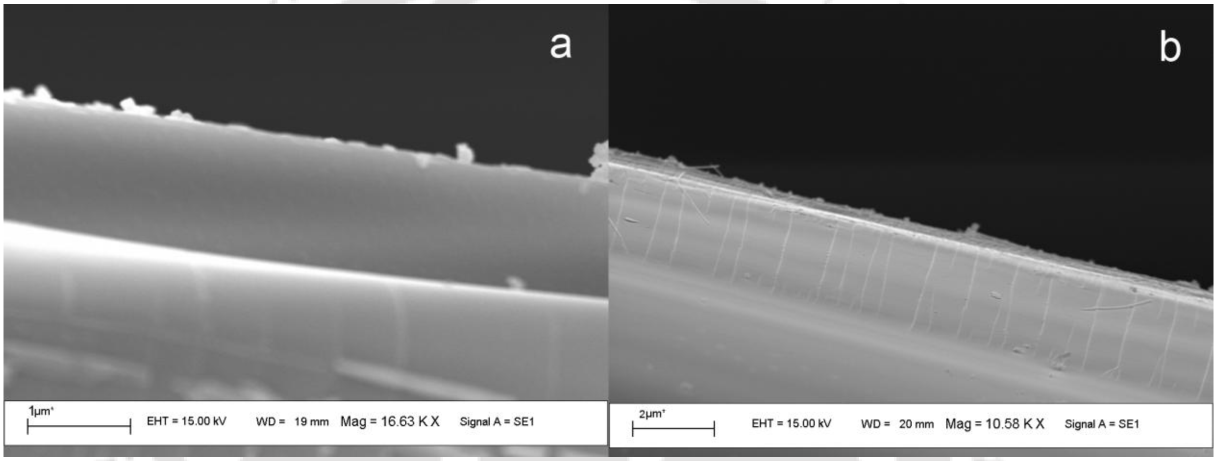

Figure 4.8 Cross sectional SEM image of TiO_2 thin films (a) 10^{-2} mbar O_2; (b) 1 mbar O_2 pressure

This also gave rise to more and more nucleation centers available for the transformation into rutile phase upon annealing [167]. At low O_2 pressure, the expansion velocities of different species contained within the laser ablated TiO_2 plasma were very high which resulted into the bombardment of ablated particles on to the substrate surface with high energy. This incoming flux of high energy particles may have disrupted the nucleation of adatoms on the substrate surface and spoiled the lattice structure making the film less crystalline in nature.

4.2.3 Optical Properties

The absorption edge for unannealed TiO_2 film, curve A of Fig.4.9, was observed at 380 nm corresponding to a bandgap of ~ 3.26 eV matching with that of anatase TiO_2 [177, 178]. With increase in annealing temperature to 650°C, a red shift in absorption edge from 380 nm to 407 nm was observed (curve D of Fig. 4.9). The TiO_2 films annealed at 650° C were having a band gap of ~ 3.04 eV, close to bandgap of rutile TiO_2 (3.03 eV) [177, 178]. This observation further confirmed formation of rutile phase at higher annealing temperatures in accordance with the XRD results, Fig. 4.3.

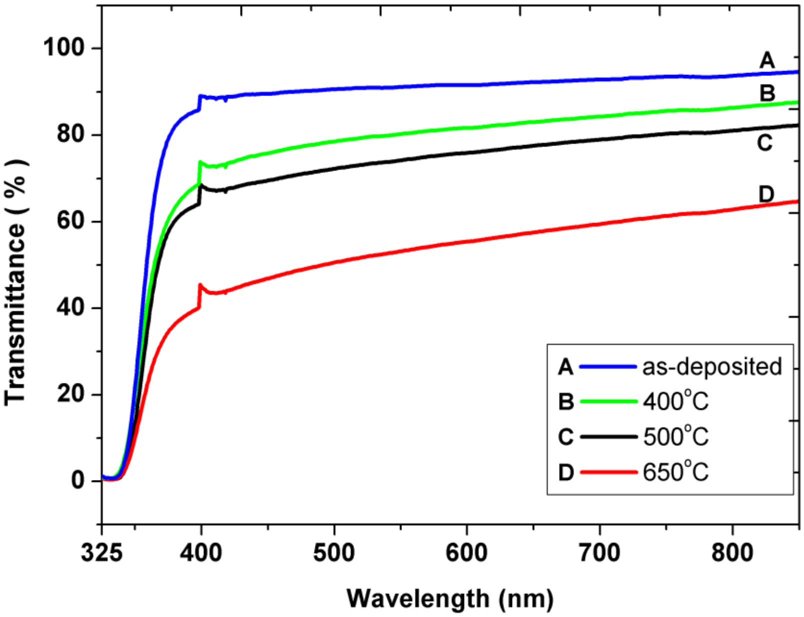

Figure 4.9 Transmission spectra of as-deposited and annealed TiO_2 thin films

The transmission of TiO_2 thin films in ultraviolet-visible region decreases with the increase in annealing temperature as shown in Fig 4.9. The average transmittance in visible region, of TiO_2 film annealed at 500°C was ~ 70%. When the annealing temperature was raised to 650°C, the transmittance of TiO_2 film was decreased to ~ 50%. A separate UV-VIS spectrophotometer with an integrating sphere was used to record UV-VIS diffuse reflectance spectra (DRS). Figure 4.10 shows the diffuse reflectance spectra of annealed TiO_2 thin films in UV-VIS region. It can be seen that the reflectance of TiO_2 thin films increased with increase in annealing temperature. Room temperature deposited TiO_2 thin films (unannealed) at 0.1 mbar O_2 ambient showed only about 10% reflectance, which can be very useful for anti reflection coating applications . For films annealed at temperatures as high as 650^{o}C, reflectance increased up to 20%.

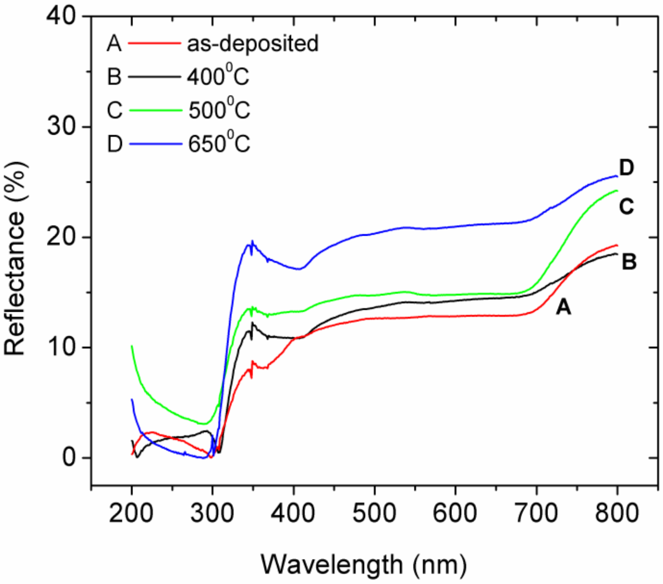

Figure 4.10 Diffuse reflectance spectra of as-deposited and annealed TiO_2 thin films

Figure 4.11 shows Photoluminescence (PL) spectra of TiO_2 thin films deposited at 0.1 mbar O_2 pressure. The PL was found to increase slightly with increase in annealing temperature as crystalline structure of deposited films improved. A large red shift in PL from 396 nm to 415 nm was observed in annealed thin films due to the formation of rutile phase which has band gap of about 3.03 eV while that of anatase phase has a band gap of about 3.26 eV [177, 178].

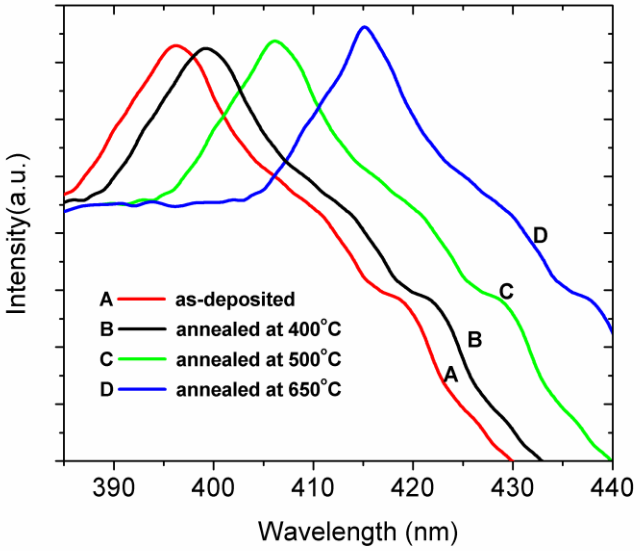

Figure 4.11 PL spectra of as-deposited and annealed TiO_2 thin films (deposited at 0.1 mbar O_2 pressure)

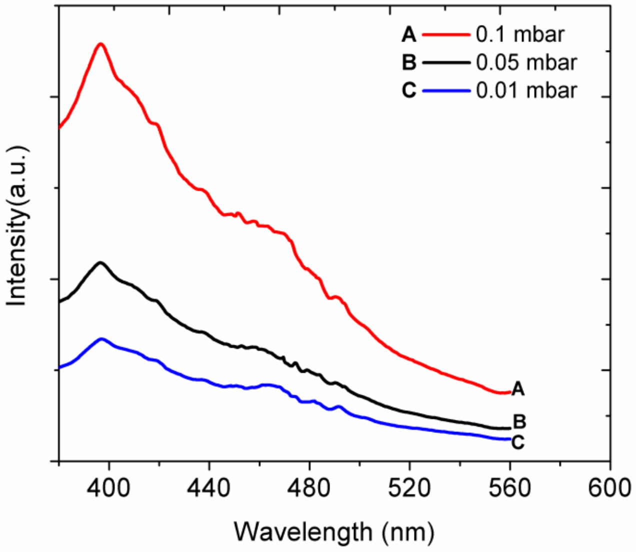

Figure 4.12 PL spectra of 500°C annealed TiO_2 thin films deposited at different O_2 pressures

Figure 4.12 compares the PL spectra of TiO_2 thin films deposited at different O_2 pressures, annealed at 500°C. The PL of TiO_2 thin films increased with O_2 pressure. This behavior was attributed to the increase in thickness [Figure 4.8 (a) and (b)] and crystalline quality of TiO_2 thin films at high O_2 pressures.

Figure 4.13 shows FTIR spectra of pulsed laser deposited TiO_2 thin films at different annealing temperatures. FTIR spectra further confirmed formation of mixed anatase-rutile TiO_2 phase at higher temperatures. The peak at 448 cm^{-1} was attributed to anatase TiO_2 phase and denoted by A-TiO_2.

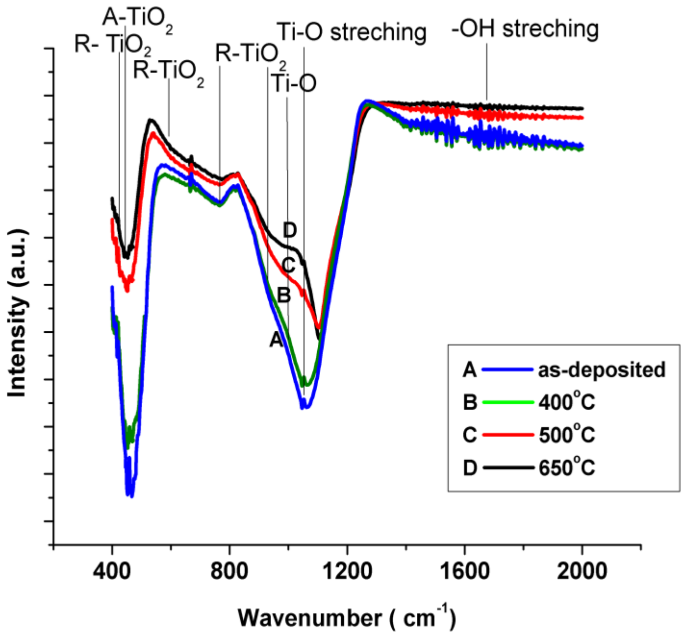

Figure 4.13 FTIR spectra of as-deposited and annealed TiO_2 thin films

The peaks at 423 cm^{-1}, 608 cm^{-1}, 765 cm^{-1} and 917 cm^{-1} were attributed to rutile phase of TiO_2 while peak at 990 cm^{-1} corresponds to TiO [179-181]. The peak at 1052 cm^{-1} was attributed to Ti-O bond stretching while broad peak centered around 1622 cm^{-1} is attributed to –OH bond stretching [180, 182] responsible for hydrophilic nature of TiO_2 thin films. The decrease in –OH peak intensity at high temperatures of annealing was due to water desorption from TiO_2 films upon annealing. FWHM of TiO_2 and Ti-O peaks decreased with increased annealing temperature. This can be attributed to increased crystalline structure and increased grain size at higher annealing temperature.

4.2.4 Effect of annealing temperature on hydrophobic properties of TiO_2 thin films

Hydrophilicity and hydrophobicity of the TiO_2 film have been reported to have relationship with the stoichiometry. It has been reported that anatase phase shows the lower angle and thus higher hydrophilicity [183]. Table 4.1 lists the contact angle between water and typical TiO_2 thin film surface deposited at 10^{-1} mbar O_2 pressure at room temperature followed by post-annealing at different temperatures.

Annealing temperature (^{o} C)	**Contact angle (^{o})**
as-deposited	36
0	56
50	60
500	65

Table 4.1 Variation of contact angle of TiO_2 with water for different annealing temperatures

The contact angles between water drop and TiO_2 film surface, measured by drop shape analysis, were found to increase from 36^o to 65^o with increase in the annealing temperature. This shows that the films were fairly hydrophobic in nature and tend towards more hydrophobic in nature after annealing. This behavior of TiO_2 films was also in accordance with decrease in –OH peak intensity at high temperatures of annealing as revealed by FTIR measurements, Fig 4.13.

4.3 Conclusion

TiO_2 thin films deposited via PLD technique in Ar ambient were predominantly having amorphous anatase phase which upon annealing at 500° C changed to crystalline anatase phase. Enhanced crystalline structure and change in phase from anatase to rutile with annealing temperature was observed for TiO_2 thin films deposited in O_2 ambient. Higher O_2 pressure during deposition helped in improving the crystalline nature of the film. TiO_2 nanorods were obtained after post-annealing at 650° C of the films deposited at 1 mbar O_2 pressure. The Ti:O ratio was found to be more stochiometric for films deposited in O_2 ambient as compared to Ar ambient. The PL spectra of TiO_2 films showed red shift with increase in annealing temperature with peak position at 3.03 eV for as-deposited film to 3.26 eV for 650°C annealed film. As–deposited TiO_2 thin film showed 10% reflectance in UV-VIS range which may be suitable for anti-reflection coating applications. The UV-VIS spectra showed decrease (increase) in transmittance (reflectance) of TiO_2 films with annealing temperature, respectively. FTIR spectrum showed decrease in FWHM of TiO_2 and Ti-O peaks due to increase in crystalline behavior and increase in grain size upon annealing. The contact angle measurements confirmed the higher hydrophobicity of TiO_2 thin films with the increase in annealing temperature. The post-annealed films deposited in oxygen ambient were observed to be highly stable due to rutile nature of the films. The above results show the control on the quality of pulsed laser deposited thin films of TiO_2 using different deposition and annealing conditions.

Chapter 5

Pulsed Laser Deposition and Characterization of ZnO and $Zn_{1-x}Mg_xO$ ($0<x<0.7$) thin films

Zinc oxide (ZnO) is a very promising wide band gap (3.37 eV) material for different technological applications because of its unique optical and electronic properties [87]. The high conductivity of ZnO, together with broad optical transparency of its thin films finds applications in transparent electrodes for flat-panel displays [184], thin film transistors [185], light emitting diodes [186], gas sensors [187] and solar cells [188]. The bandgap of ZnO can be tuned up to 6.0 eV by forming the ternary alloy of $Zn_{1-x}Mg_xO$ for applications in deep UV range [99-101] due to their excellent excitonic properties [97, 189, 190]. In most of the ZnO based optoelectronic devices requiring bandgap tunability, it is essential to synthesize the lattice-matched heterojunction of $Zn_{1-x}Mg_xO$ /ZnO which requires fabrication of hexagonal wurtzite $Zn_{1-x}Mg_xO$ thin films while keeping their excitonic properties intact.

In contrast to the extensive literature relating to ZnO thin films produced by PLD [191, 192], relatively little effort has been directed towards characterization of the laser ablated plasma plume from which such films are produced and its effect on to the properties of ZnO thin films [193-195].

In this chapter, pulsed laser deposition of c-axis oriented wurtzite ZnO thin films on Si (100) and Al_2O_3 (0001) substrates is presented. Studies on laser ablated ZnO plasma in O_2

ambient were performed. The effect of plasma parameters on to the properties of pulsed laser deposited ZnO thin film was studied. The tuning of band gap and room temperature excitonic emission from pulsed laser deposited $Zn_{1-x}Mg_xO$ thin films as a function of Mg concentration (x) is reported. Wurtzite hexagonal single phase was obtained up to 34% of Mg doping while mixed hexagonal and cubic phases were obtained for above 40% Mg doping. $Zn_{1-x}Mg_xO$ thin films with cubic single phase were obtained for Mg concentration of 60% and above. Effect of Mg doping on the room temperature Raman spectra of wurtzite ZnO is also presented. Room temperature absorption spectra of $Zn_{1-x}Mg_xO$ (x=0.0 to x=0.34) thin films were recorded and modeled to determine exciton band gaps, binding energies and broadening parameters. The dependence of substrate temperature on to these parameters was studied. Further to improve the quality of $Zn_{1-x}Mg_xO$ films grown by pulsed laser deposition, annealing effects of the sapphire substrate prior to deposition on the structural and optical properties of $Zn_{1-x}Mg_xO$ thin films were studied.

5.1 Experimental Details

Detailed experimental setup for the recording of plasma emission spectra and spatio-temporal variations of emitted species during ZnO thin film deposition via PLD is described in the Chap. 2, Sec. 2.4. The laser ablated ZnO plasma, consisting of ions and neutrals of Zn and O, expands in the background of oxygen, undergoes the reaction dynamics and is finally deposited onto ultrasonically cleaned Si(100) and sapphire (0001) substrates placed 3 cm apart from the ZnO target (prepared from ZnO powder, Sec 2.1). ZnO films were deposited in O_2 ambient at room temperature for a deposition time of 30 min. The O_2 pressure was varied in the range of 10^2 mbar to 10^{-5} mbar. Laser irradiance was kept fixed ~ 3 × 10^{11} W/cm^2

during PLD as well as spectroscopic analysis of ZnO plasma. At larger intensities, large particulates came out of ZnO target and deposited on to the substrate. Thus, deteriorating the quality of deposited film. While below this irradiance level, ZnO plasma expansion was small and partially reaching up to substrates placed at 3 cm distance from the target surface. This resulted in the deposition of ZnO thin films with poor crystalline quality.

For the deposition of $Zn_{1-x}Mg_xO$ thin films, MgO-ZnO composite targets with MgO contents from 0 mol. % to 70 mol. % were used (Sec 2.1). Ultrasonically cleaned and polished sapphire (0001) was used as a substrate, placed at a distance of 4 cm from the target. $Zn_{1-x}Mg_xO$ thin films were deposited at different substrate temperatures ranging from room temperature to 700^0C and deposition time was kept fixed for 30 min. To study the effect of pre-annealing, (0001) oriented sapphire substrate, were annealed in a furnace at temperatures in between 800^oC and 1200^oC in air for 2 hrs before mounting inside the ablation chamber for deposition.

5.2 Pulsed Laser Deposition of ZnO thin films and Effect of ZnO plasma dynamics on the properties of pulsed laser deposited ZnO thin films

With the aim to investigate the laser-induced plasma and the probable role of gas-phase reactions in ZnO formation, the dynamics of the chemical species produced by laser ablation of ZnO targets in an oxygen environment was recorded and analyzed. The properties of the plasma plume were investigated by acquiring spatial and temporal profiles of emitted spectra as function of distance from the target surface in presence of oxygen gas; pressures in the range of 10^{-5} mbar to 10^{2} mbar. Analysis of these data provides information on the nature of the ejected particles, their density, and temperature in the vicinity of the target surface. An attempt is made to correlate the characteristics of the ZnO thin films deposited by laser ablation with the properties of laser induced ZnO plasma.

5.2.1 Estimation of electron temperature and density in laser induced ZnO plasma

The wavelength dispersed emission spectrum of the plasma plume during the ablation of the ZnO target at 0.1 mbar of O_2 pressure and recorded at a distance of 5 mm from the target surface is shown in Figure 2.6 (Chap. 2 Section 2.4). The strong emission lines of Zn I, Zn II, and O I were identified [Table 2.3] and marked in Figure 2.6. The lines used to estimate the electron number density and electron temperature, the two important parameters to understand the dynamics of laser induced plasma are listed in table 5.1. The electron number density was estimated from the stark broadening of transition lines, given by eq.1.7 (Chap.1, Sec 1.2.2.2).

Transition	**Wavelength λ (nm)**	**Transition probability A_{ki} (s^{-1})**	**Lower level energy E_i(cm^{-1})**	**Upper level energy E_k(cm^{-1})**	**Log g_f**	**J_i - J_k**
Zn I	480.05	7.0e+07	32890.352	53672.280	-0.137	2 - 1
Zn II	491.16	1.6e+08	217846.80	238205.50	-0.213	1 - 2
O I	777.19	3.69e+07	73768.20	86631.45	0.324	2 - 3

Table 5.1 List of parameters of the transition lines used for electron temperature and electron number density calculations

Figure 5.1 shows the broadened spectral profiles of O I (777.19 nm) line at different ambient pressures measured at a distance of 5 mm from the target surface and fitted with Lorentzian profile.

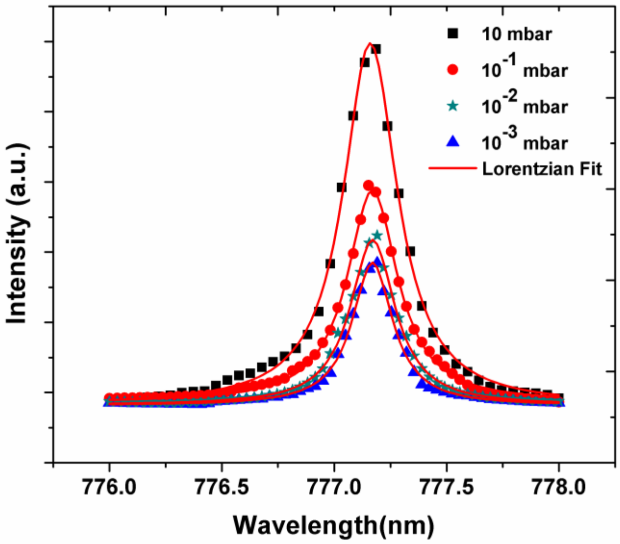

Figure.5.1 Stark broadened profile of O I (777.19 nm) spectral line at different pressures

The electron temperature was estimated by using Saha-Boltzmann equation (eq. 1.4, Chap. 1, Sec. 1.2.2.1) For temperature calculations, the line intensities corresponding to emission lines of 480.05 and 491.16 nm, respectively, of Zn I and Zn II have been used (Table 5.1). The optical data required for the above calculations were taken from literature and standard database [55, 154, 155].

5.2.2 Comparison of pre- and post- laser exposure of ZnO target

The surface of the polycrystalline ZnO pellet used in the present work was insulating and pale yellow in colour. After laser irradiation at 10^{-5} mbar base pressure, the ZnO target surface became gray in colour and conducting, both within the focal region as well as its immediate surroundings. Figure.5.2 shows the scanning electron microscope images of the (a) virgin ZnO target surface and (b) ZnO target surface in the surroundings of the focal region after laser irradiation. SEM images clearly show that crystalline structure of ZnO target surface changed into ripples and semi spherical droplet like structure upon laser irradiation due to local heating, melting and ablation of photoexcited region. From EDX analysis, it was observed that the laser irradiated ZnO target surface exhibit a higher composition of Zn than that in the virgin ZnO target, suggesting formation of a Zn-rich top layer upon irradiation probably due to back-deposition of sputtered zinc from the ablation plume itself. This observation suggests that there is a requirement to optimize background gas pressure of O_2 during the pulsed laser deposition of crystalline and stoichiometric ZnO thin films, in order to interact with the excess Zn in the ablation plume.

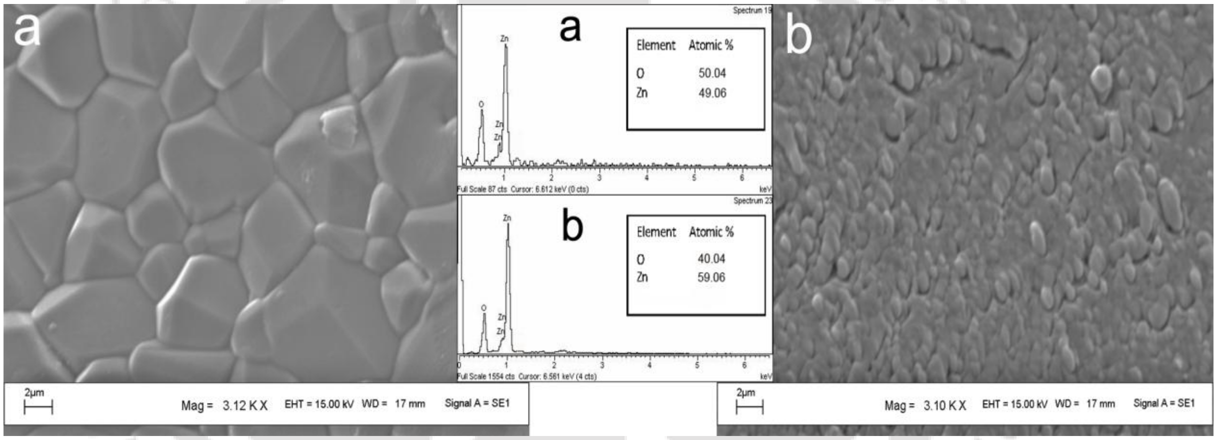

Figure.5.2 SEM and EDX spectra of (a) virgin ZnO target (b) ablated ZnO target in the neighbourhood of the focal region.

5.2.3 Spatial and pressure dependence of electron temperature and density in laser produced ZnO plasma

The electron temperature and electron density of the ZnO plasma at 10^{-1} mbar O_2 pressure as a function of distance from the target surface is shown in Fig.5.3 (a). With increasing distance from the target surface, the electron temperature falls down exponentially from 1.43 eV at 1 mm to 0.36 eV at 10 mm. Beyond 10 mm distance the electron temperature is almost constant. Electron density decreases from 5.4×10^{17} cm^{-3} to 1.1×10^{17} cm^{-3} over a distance of

10 mm from the target surface and there after it is nearly stabilized. Initially, when the laser pulse strikes a solid surface, ions and excited neutral atoms are emitted during the laser pulse. The free electrons in the rapidly expanding plasma, in the initial phase, grow by multi photon ionization. When a high electron concentration approaches a critical electron density, the further growth is slowed down by the onset of electron-ion recombination process, along with the rapid cooling of plasma due to expansion [196, 197].

At larger distances, the free expansion of the plasma plume is curtailed because of the presence of surrounding gas as well as adiabatic cooling [198] resulting into redistribution of kinetic and thermal energy and particle flux [199, 200], which finally stabilizes the electron temperature and the electron density to certain extent beyond 8-10 mm distance from the target, as shown in Fig.5.3.

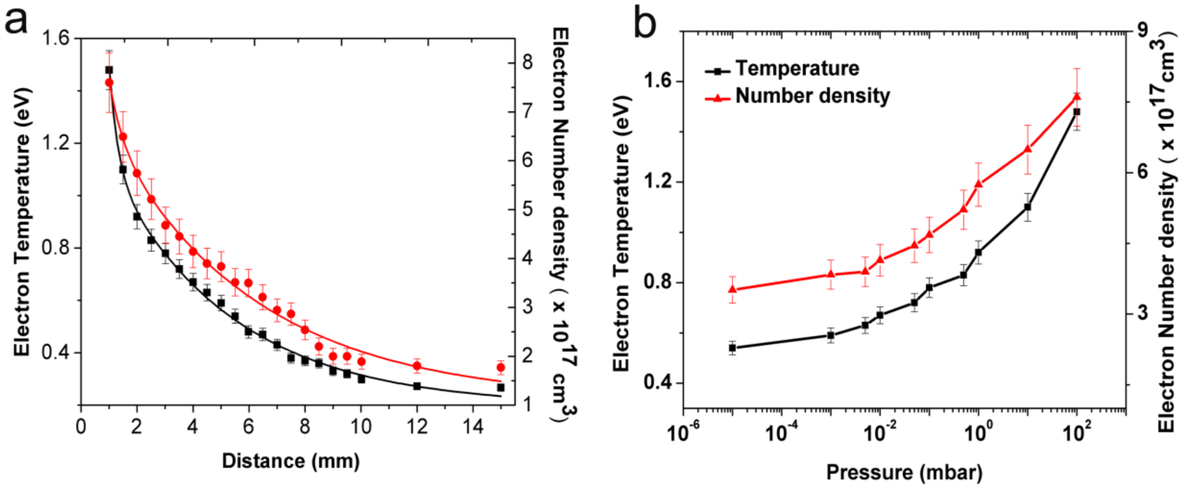

Figure.5.3. Variation of electron temperature and electron number density (a) with distance at 10^{-1} *mbar* O_2 *pressure; (b) with* O_2 *pressure at a distance of 5 mm from the target*

Figure.5.3 (b) shows the variation of electron density and electron temperature with ambient pressure at 5 mm distance from target surface. Under vacuum and at low background pressures ($<10^{-2}$ mbar), the expansion (as well as cooling) of the plasma is like a free expansion and so little away from the target, the electron temperature and density are small compared to those of at relatively higher pressures in the range of 1 mbar - 100 mbar, where plasma expansion is suppressed due to high O_2 pressure. Thus the electron temperature and density increased with background pressure, slightly away from the target surface as shown in Fig.5.3. The integrated emission intensity of Zn II (491.1 nm), Zn I (636.6 nm) and O I line (777.1 nm) at 0.1 mbar O_2 pressure as a function of distance from the target surface is shown in the Fig.5.4 (a). The integrated yield was obtained by integrating the area under the emission profile of the particular lines under consideration. This gives a measure of the amount of excited species within the plume, arriving at a given point. The integrated intensity of O I emission generated during the ZnO ablation showed steady increase up to 12 mm distance from the target and then a monotonic decrease with further increase in distance. This is attributed to the increased amount of the excited oxygen atoms due to dissociation of oxygen molecules upon collision with the particles in the plume in the neighborhood of the target surface. While in the later stage, due to plasma expansion, the mean free path for the individual species increases and the collision probability decreases, which results into reduction of O I intensity. As shown in Fig.6, intensity of Zn II ions increases initially with distance from target surface due to dissociation of ZnO molecules at high electron temperatures. With further expansion, at larger distances (> 5 mm) reduction in plasma temperature and density favours the recombination of Zn II ions with electron to form Zn neutrals. Therefore the intensity of Zn II emissions start decreasing beyond 5 mm distance where as that of Zn I continues to increase till ~ 10 mm and then falls down due to the further expansion and formation of ZnO molecule back. Due to high density of Zn ions near the target surface, ZnO thin films with 1:1 stoichiometry cannot be obtained at very small target to substrate distances. This is also confirmed by target composition measurements after laser irradiation, shown in Fig.5.2.

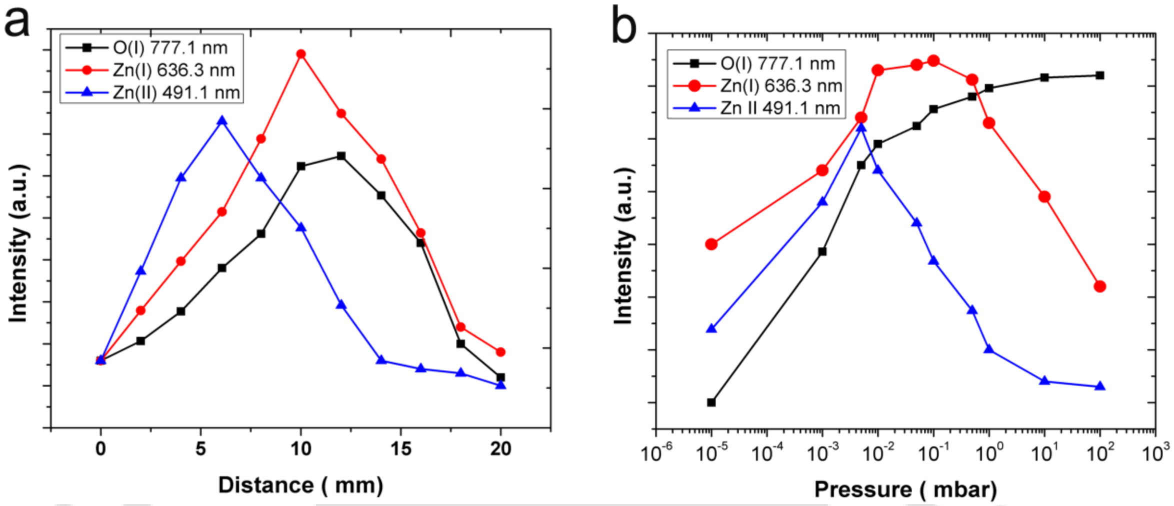

Figure.5.4 Variation of Zn I, Zn II and O I integrated intensities (a) with distance at 10^{-1} *mbar* O_2 *pressure (b) with* O_2 *pressure at 10 mm from the target surface*

Fig.5.4 (b) shows the variation of Zn I, Zn II and O I integrated intensity with O_2 pressure at 10 mm distance from the target surface. It can be observed that the increase in oxygen pressure increases the emission intensity of O I line.

The emission line intensities of the neutral Zn and neutral oxygen were enhanced at higher O_2 pressure while the emission line intensities of Zn ions decreased after 5×10^{-2} mbar O_2 pressure. Increase in O_2 pressure reduces the mean free path of particles in the plume, thereby increasing the probability of collision of Zn ions with electrons in the plume resulting into increased number of the excited zinc atoms due to electron-ion recombination. Zn I line intensity exhibited a steady behavior in the pressure range of 5×10^{-2} mbar to 5×10^{-1} mbar. In the same pressure range, sharp decrease in Zn ions intensity can be observed. This indicates that recombinative generation of excited Zn neutrals efficiently compensates for their loss due to plasma expansion in this pressure range. At very low O_2 pressures ($<10^{-3}$ mbar) intensity of Zn ions is large and intensity of oxygen neutrals is comparatively small [Fig.5.4 (b)], indicating stochiometric ZnO can not be obtained at very low ambient pressures, in agreement with the previous observations of other researcher's [193].

5.2.4 Correlation of Plasma parameters with the properties of pulsed laser deposited ZnO thin films

Fig.5.5 shows XRD spectra of ZnO thin films deposited on to Si (100) substrates at different O_2 pressures ranging from 10^{-5} mbar to 10 mbar, at a distance of 3 cm from target using pulsed laser deposition technique.

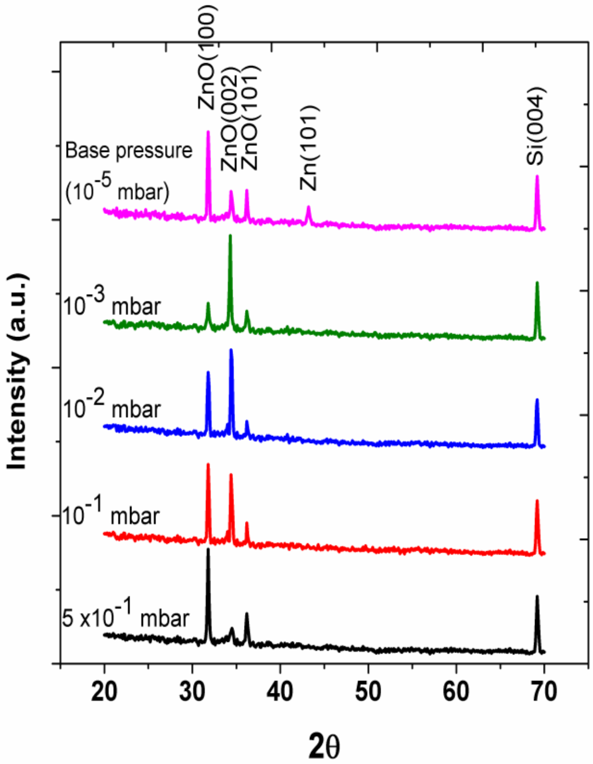

Figure.5.5 XRD spectra of ZnO thin films deposited on to Si (100) at different O_2 pressures

It has been observed that at high O_2 pressures (>10^{-1} mbar), deposition of polycrystalline ZnO films take place with relatively low c-axis orientation. With decrease in O_2 pressure intensity of ZnO (002) peak increased and at 10^{-3} mbar O_2 pressure highest ZnO (002) peak intensity can be observed, indicating deposition of highly c-axis oriented ZnO films. At very low O_2 pressures (~ 10^{-5} mbar), metallic Zn peaks has been also observed. This behavior indicates Zn rich nature of plume at low O_2 pressures which was also confirmed by spectroscopic measurements as discussed in the previous section.

Fig.5.6 shows SEM images of ZnO thin films deposited at different O_2 ambient pressures in the range of 10^{-5} mbar to 10^{-1} mbar

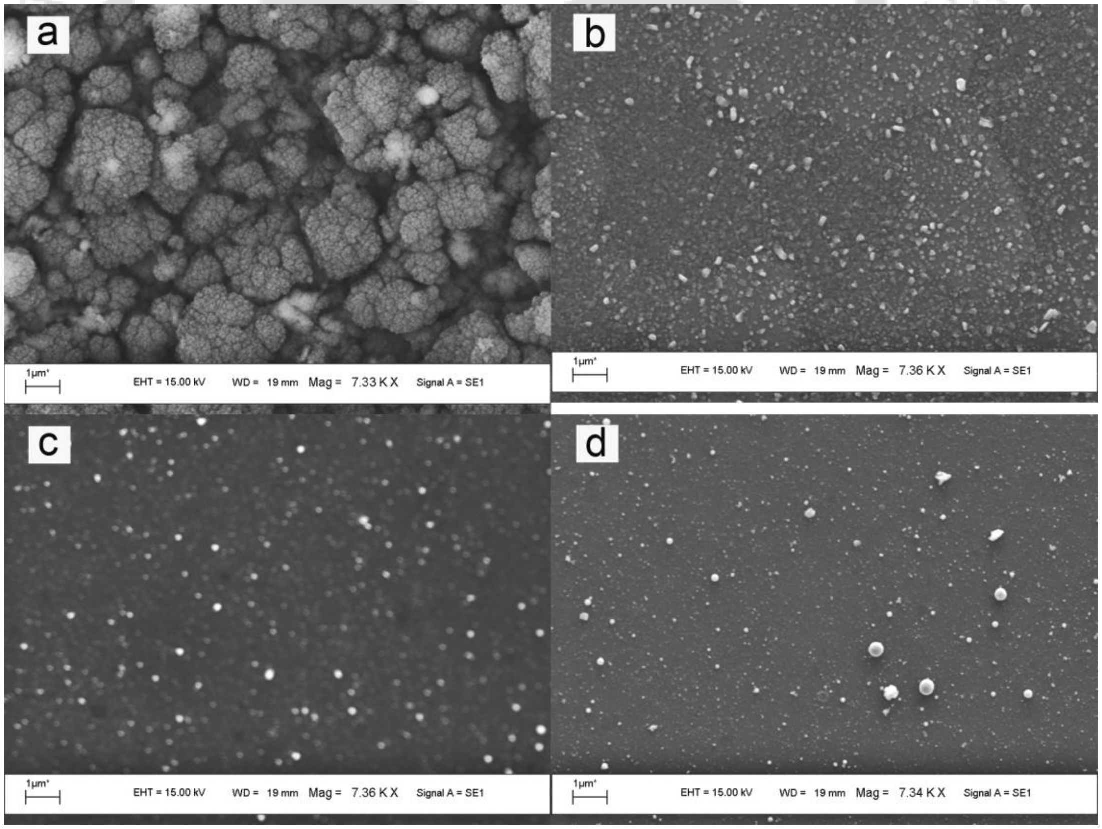

Figure.5.6 SEM images of ZnO thin films deposited at (a) 5×10^{-1} mbar, (b) 10^{-2} mbar, (c) 10^{-3} mbar and (c) 10^{-5} mbar base pressure

The average grain size increases at high O_2 pressures ($\geq 10^{-1}$mbar) as well as very low O_2 pressures ($<10^{-3}$ mbar). This behavior can be attributed to clustering of vapour phase particles at high O_2 pressure and high adatom energies at very low O_2 pressures [201]. Thus, it can be concluded that to obtain the smooth cluster free ZnO films the background oxygen pressure should be in the range of 10^{-3} mbar to 10^{-1} mbar.

Figure.5.7 shows the PL spectra of the ZnO films deposited on to (0001) sapphire substrates at different ambient pressures. The excitation wavelength used was 300 nm from Xe lamp.

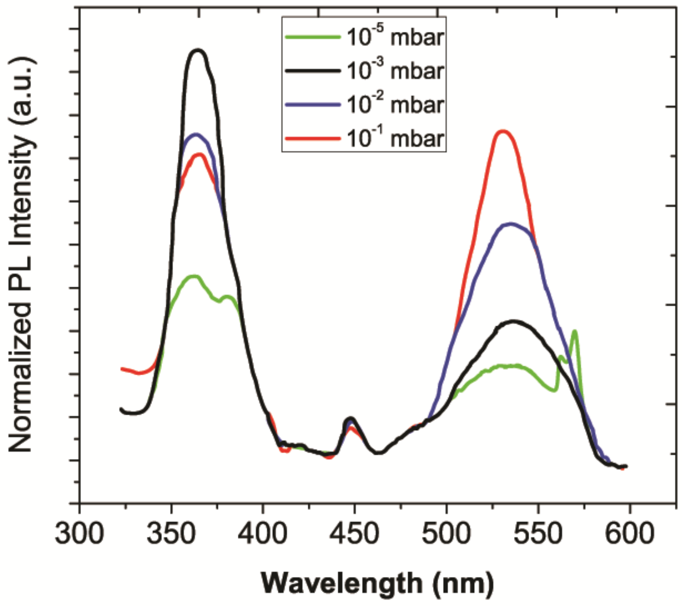

Figure.5.7 PL spectra of ZnO thin films deposited on to Si (100) at different O_2 pressures

It can be observed that with increasing O_2 pressure, there was a considerable increase in defect related green band emission as compared to that of band edge UV emission. The excess oxygen at high pressures (confirmed by increased intensity of O I line) may replace zinc atoms in the crystal lattice and form a defect state known as O_{Zn}. Band edge UV emission intensity decreases for ZnO films deposited at low O_2 pressures, most probably because of deposition of metallic Zn as confirmed by XRD measurements shown in Fig.5.5.

The steady behavior of electron density, electron temperature and integrated intensities of Zn and Zn ions, and high oxygen line intensities above 10 mm distance from the target surface suggest that high quality ZnO thin films can be expected when substrate is placed beyond this distance. The reports show that stoichiometric and crystalline films are formed at a few centimeters away from the target surface [202]. Even at relatively low laser intensities, near the threshold for ablation, it has been observed that the ablated materials are significantly ionized [203-205], and the ions in the plasma plume can have energies ranging up to several hundred eV [206]. So at small target to substrate separation there is a chance of sputtering from the substrate by these highly energetic particles and thereby affecting the qualities of the thin film. Hence for proper nucleation and growth of crystalline thin films, larger target to substrate distance and heating of substrate is recommended.

5.3 Effect of Mg doping and substrate temperature on the properties of pulsed laser deposited epitaxial $Zn_{1-x}Mg_xO$ thin films

The direct band gap of ZnO (3.37 eV) can be tuned up to 7.2 eV by alloying with MgO. The Mg^{++} ions can replace Zn^{++} ions in the ZnO lattice while maintaining the hexagonal structure due to the similar ion radius of Mg^{++} (0.057 nm) and Zn^{++} (0.060 nm) [207]. The solid solubility of Mg in ZnO lattice is limited to only 4 % (by atomic weight) maximum with the unit cell retaining its hexagonal structure [208]. This problem can be overcome by using PLD technique due to the non-equilibrium nature of PLD process which makes it possible to fabricate composite thin films well above the thermodynamic solubility limit [35]. Still, hexagonal $Zn_{1-x}Mg_xO$ composites can only be obtained up to around 40 % of Mg concentration (x) due to cubic structure of MgO.

In this section, the tuning of band gap of $Zn_{1-x}Mg_xO$ ($0.0 \leq x \leq 0.7$) thin films as a function of Mg concentration (x) is reported. The $Zn_{1-x}Mg_xO$ thin films upto 34% of Mg content, deposited via PLD on to (0001) Al_2O_3 substrate, were having hexagonal structure. Above 34% of Mg concentration, mixed hexagonal and single cubic phases were observed. Effect of Mg concentration and substrate temperature on the structural, surface morphological and optical properties of $Zn_{1-x}Mg_xO$ thin films was analyzed [209].

5.3.1 XRD Characterization of $Zn_{1-x}Mg_xO$

Fig.5.8 shows XRD patterns of pulsed laser deposited $Zn_{1-x}Mg_xO$ thin films at 700^0C with x ranging from x=0.0 to x=0.60. XRD results showed that the thin films with Mg content of upto x=0.34 have hexagonal wurtzite structure. Only (*0002*) reflections were observed in the XRD pattern for these films, indicating the films were textured with c-axis perpendicular to the substrate surface. The position of (*0002*) reflection was found to shift toward higher angles w.r.t. to that of pure ZnO peak with the increasing concentration of Mg. According to Bragg's rule, this corresponds to decrease in c- axis lattice constant. As more Mg was introduced into the ZnO lattice, it lodged into the interstitial positions, leading to a decrease in the lattice constant. The lattice constant, c, of $Zn_{1-x}Mg_xO$ thin films with Mg concentration varied almost linearly, from 0.5212 nm (x=0.00) to 0.5146 nm (x=0.34) [Fig.5.9]. Above 40% of Mg content in the films, mixed phase reflections corresponding to both hexagonal wurtzite and MgO cubic phase appear, as shown in XRD pattern for 48% Mg doped ZnO film. With further increasing the Mg content in the films, cubic phase dominated and above 60% Mg doping, peaks corresponding to single MgO cubic phase were clearly observed.

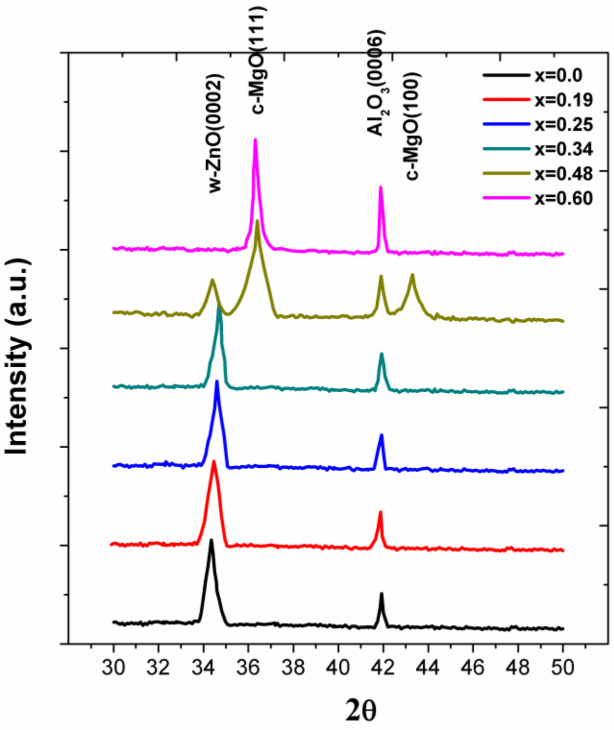

Figure.5.8 XRD pattern of $Zn_{1-x}Mg_xO$ (x =0.00, x=0.19, x=0.25, x=0.34, and x=0.60) thin films deposited via PLD at 700^oC in 10^{-1} mbar O_2 pressure

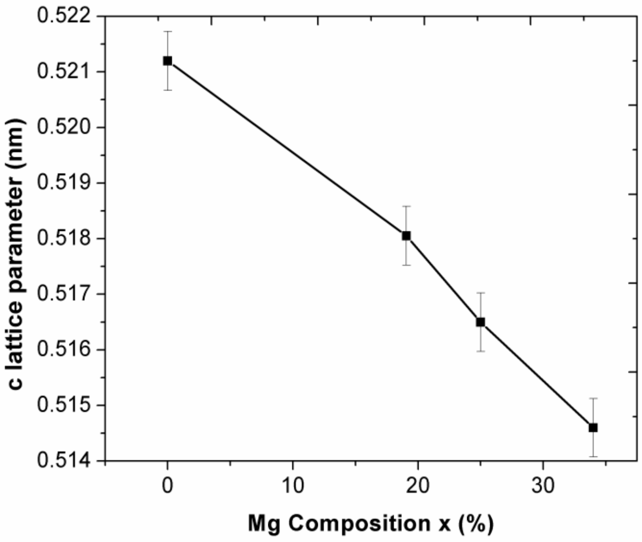

Figure5.9 Variation of c-axis lattice parameter with Mg composition for hexagonal $Zn_{1-x}Mg_xO$ *(*$0.0 \leq x \leq 0.34$*) thin films*

Fig.5.10 shows XRD patterns of $Zn_{1-x}Mg_xO$ thin films deposited at different substrate temperatures for x=0.19. It is clear that intensity of (0002) peak corresponding to ZnO hexagonal structure increases with substrate temperature showing improvement of the crystalline quality of the $Zn_{1-x}Mg_xO$ films. The $Zn_{1-x}Mg_xO$ thin films deposited at 300^0C and lower substrate temperatures showed polycrystalline nature. The inset of Fig.5.10 shows the variation of the full width at half maximum (FWHM) of (0002) peak as a function of temperature. The FWHM value increases from 0.22^o to 0.48^o with increasing deposition temperature in the range of 400^o C to 700^oC indicating decrease in crystallite size. Decrease in crystallite size at higher deposition temperature is due to enhanced surface diffusion of adatoms.

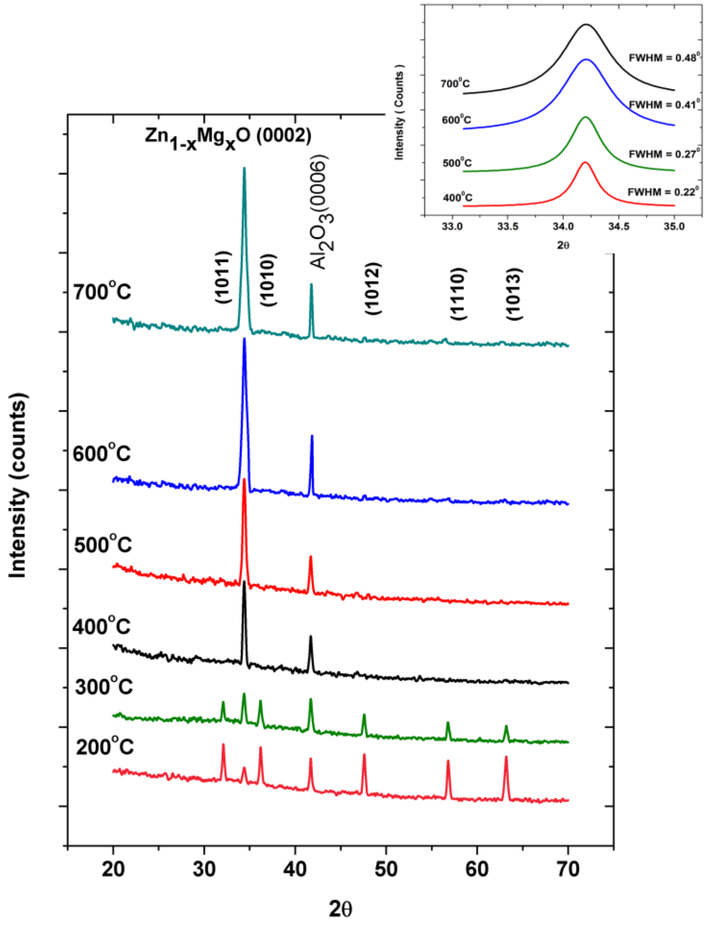

Figure.5.10 XRD pattern of $Zn_{1-x}Mg_xO$ thin films (with x =0.19) deposited at different substrate temperatures. (Inset: expanded view of (0002) peak showing increase in FWHM).

5.3.2 Raman Spectra of pulsed laser deposited $Zn_{1-x}Mg_xO$ thin films

Figure 5.11 (a) shows the room-temperature Raman spectrum of the pure ZnO (x=0.0) and $Zn_{1-x}Mg_xO$ thin films (deposited at 700°C) for x = 0.10, 0.19, 0.25 and 0.34. The peaks at 99 and 438 cm^{-1} are attributed to ZnO nonpolar optical phonon E_2^{low} and E_2^{high} modes, respectively [210]. The peak at 413 cm^{-1} corresponds to the $E_1(TO)$ mode [210]. The characteristic peak of hexagonal wurtzite ZnO, the E_2^{high} at 438 cm^{-1} is very intense and has a full-width at half-maximum of 8 cm^{-1} [Fig.5.13 (b)]. The asymmetrical and line-broadening characteristics of $E_1(TO)$ increases with Mg doping and merged with E_2^{high} as well as $A_1(TO)$

mode at higher Mg concentrations as shown in Fig.5.11 (b). Mg-doping induces microscopic structural disorders in periodic ZnO lattice and it is characterized by asymmetric line broadening and shift in ZnO Raman modes.

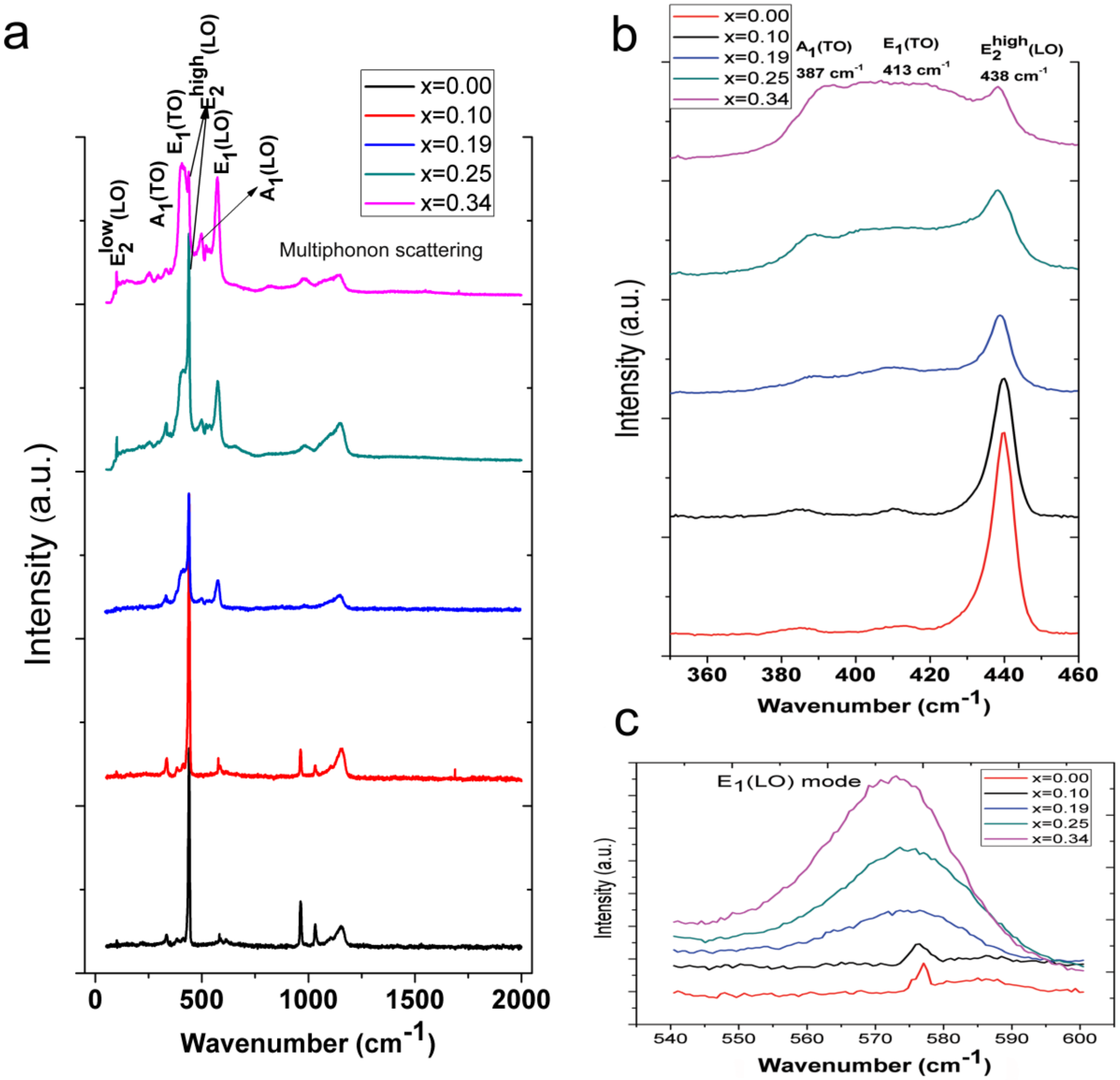

Figure.5.11 (a) Raman spectrum of $Zn_{1-x}Mg_xO$ (x =0.00, x=0.10, x=0.19, x=0.25, and x=0.34) thin films deposited at 700°C in 10^{-1} mbar O_2 pressure, excited using 488 nm Ar-ion laser. (b) asymmetric broadening and red shift in E_2^{high} mode at 438 cm^{-1} (c) asymmetric broadening and large red shift in E_1 (LO) mode at 576 cm^{-1}

The substitution of Mg^{2+} in ZnO lattice results in the slight reduction of lattice due to difference in ionic radii of Mg^{2+} and Zn^{2+}. This shifts the particular Raman modes towards lower frequency side depending upon amount of Mg substitution [211]. The E_2^{high} mode shifts from 438 cm^{-1} (x=0.00) to 435 cm^{-1} (x=0.34) with Mg doping concentration (x), as shown in Fig.5.11 (b). The FWHM of E_2^{high} mode increased due to asymmetric line broadening from 8 cm^{-1}(x=0.00) to 14 cm^{-1}(x=0.34). These changes with Mg content (x) are marginal and indicating highly oriented wurtzite structure of Mg-doped ZnO without any phase segregation as was also confirmed by the XRD. The intensity of E_2^{high} mode was decreased with Mg doping due to slight disorientation in growth and increase in c-lattice constant. The forbidden mode E_1 (LO) at 576 cm^{-1} was observed with increasing intensity and broadening as a function of x as shown in Fig.5.11 (c). This could be attributed to defects arising due to oxygen vacancies, zinc interstitials or their complexes and free carriers [212].

The peaks at 387 and 537 cm^{-1} corresponding to A_1(TO) and A_1(LO) phonons, respectively were also observed [Fig. 5.11 (a)]. The Raman spectra showed two additional modes at 333 and 1147 cm^{-1}. These peaks have been attributed to multiphonon scattering processes [213]. The broadening in these multiphonon Raman modes with increasing Mg concentration can also be related to activation/formation of structural defects in doped ZnO. For cubic phase films with higher Mg content ($x \geq 0.60$) no first order Raman modes were observed. $Zn_{1-x}Mg_xO$ ($x \geq 0.60$) thin films shows rock-salt-type cubic crystal structure, and thus belong to the space group O_h known to have no first order Raman modes [214].

5.3.3 Surface Morphology

SEM images of $Zn_{1-x}Mg_xO$ (x=0.1) deposited at 300° C, 400° C, 500° C and 700° C are shown in Fig.5.12 (a), (b), (c) and (d) respectively. From SEM measurements, it was observed that the crystallite size of $Zn_{1-x}Mg_xO$ thin films decreases with increase in substrate temperature, which is in agreement with XRD results. Average crystallite size for $Zn_{1-x}Mg_xO$ thin film deposited at 300° C was found to be 260 nm [Fig. 5.12 (a)] which was decreased to 150 nm for $Zn_{1-x}Mg_xO$ film deposited at 700° C [Fig. 5.12 (d)].

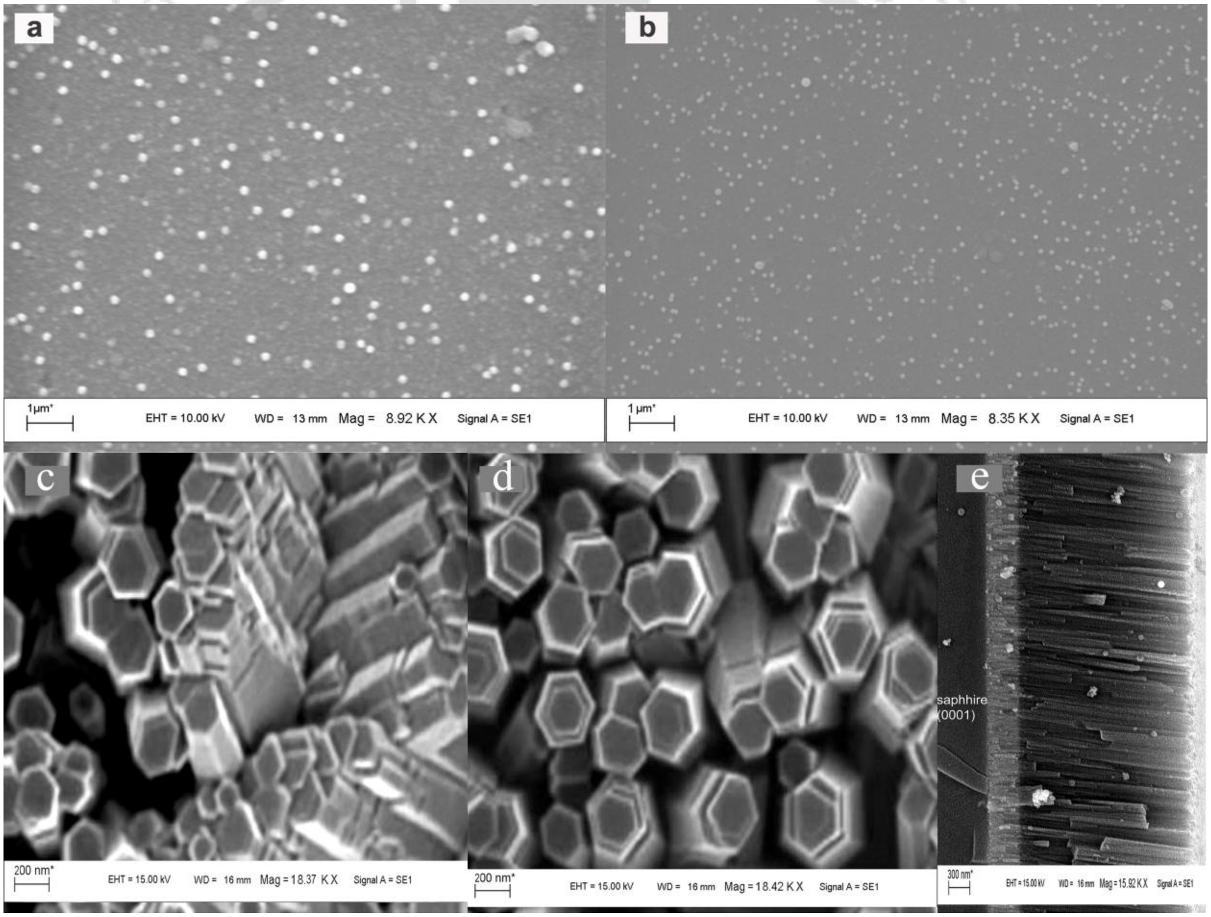

Figure.5.12 SEM image of $Zn_{1-x}Mg_xO$ thin films (with x = 0.1) deposited at (a) 300°C; (b) 400°C; (c) 500°C; (d) 700°C; and (e) Cross section SEM image of thin films deposited at 700°C

At low deposition temperatures, slanted growth of nano columns of $Zn_{1-x}Mg_xO$ was observed [Fig. 5.12 (c)]. This might have led to increased strain in the film structure, which in turn resulted into poor film quality. The films deposited at substrate temperature of 700° C showed highly columnar growth and rod like structures as shown in the cross-sectional SEM image, Fig 5.12 (d). For the films deposited below 500° C substrate temperature, columnar growth was not evident [Fig. 5.12(b)] rather spherical balls of $Zn_{1-x}Mg_xO$ were observed on the film surface, Fig 5.12 (a). Compositional analysis using EDAX was performed for all the samples and very good agreement has been observed between atomic composition of $Zn_{1-x}Mg_xO$ target and that of deposited films (Table 5.2). Hence the stoichiometric growth of $Zn_{1-x}Mg_xO$ films using PLD was confirmed.

Mg concentration x (%) in the $Zn_{1-x}Mg_xO$ target	**Atomic percentage in $Zn_{1-x}Mg_xO$ films calculated using EDAX data**		
	Zn	**Mg**	**O**
0.00	49.93	0.00	50.07
10.00	45.03	4.92	50.05
19.00	40.36	9.47	50.17
25.00	37.35	12.46	50.19
34.00	32.85	17.04	50.11

Table.5.2 EDAX composition analysis for $Zn_{1-x}Mg_xO$ films with different Mg content

Figure 5.13 shows the AFM images of $Zn_{1-x}Mg_xO$ (x=0.1) films deposited at different temperatures. For the $Zn_{1-x}Mg_xO$ films deposited at 300^o C [Fig. 5.13 (a)], the surface morphology was rough having the rms roughness of 21 nm in a scan area of 1μm × 1μm. This was attributed to the fact that the surface diffusion was insufficient due to the low deposition temperature. As the deposition temperature increased, the rms roughness was reduced. The rms roughness was observed to be around 10 nm, 7 nm, and 6 nm at 500^o C, 600^o C, and 700^o C of deposition temperatures respectively [Fig. 5.13 (b), (c) and (d)].

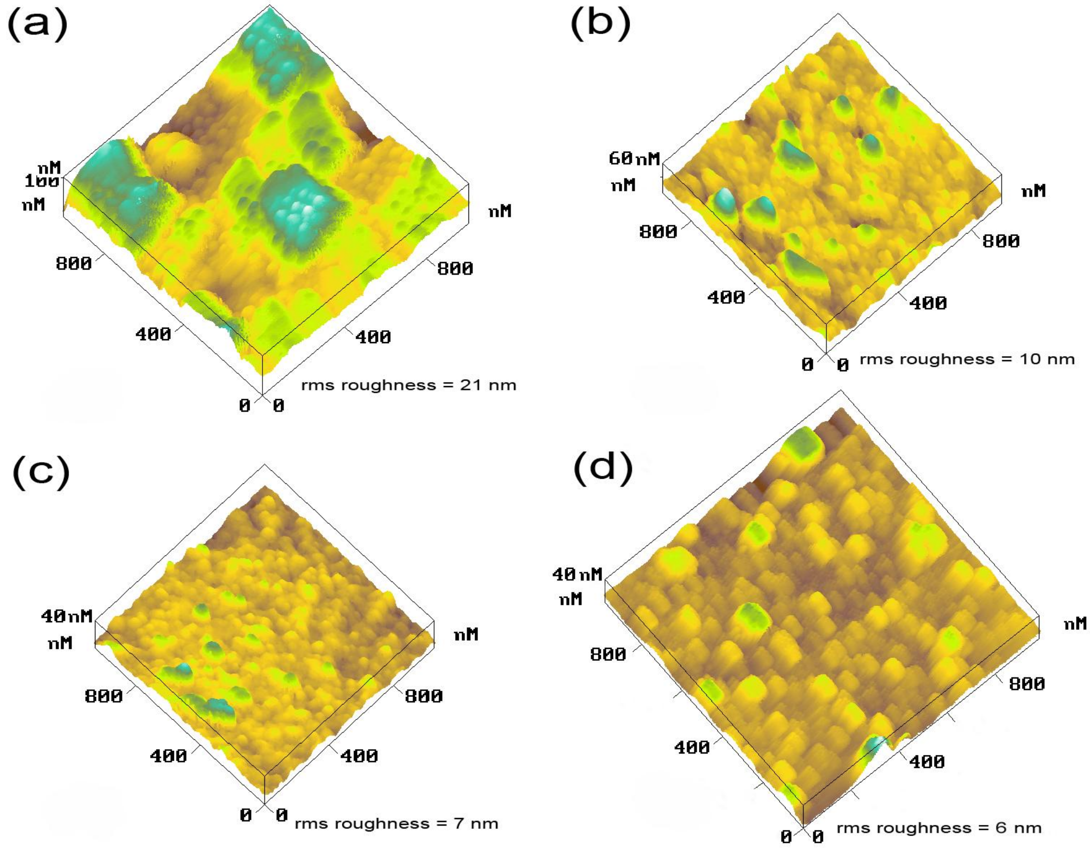

Figure.5.13 AFM images of $Zn_{1-x}Mg_xO$ thin films (with x = 0.1) deposited at (a) 300^{o}C; (b) 500^{o}C; (c) 600^{o}C; (d) 700^{o}C.

With the increase in deposition temperature, the diffusion and alignment of atoms on the surface of sapphire substrate was enhanced, resulting in a smooth surface with the rms roughness of ~ 6 nm with the vertically aligned columnar growth [Fig. 5.13 (d)] in agreement with the SEM results shown in Fig. 5.12.

5.3.4 *Room temperature excitonic emission from $Zn_{1-x}Mg_xO$ thin films*

Absorption spectra of $Zn_{1-x}Mg_xO$ thin films were recorded using a UV-VIS spectrophotometer at room temperature. Absorption coefficient α was estimated from absorption spectra using Beer-Lambert relation,

$$\alpha = \frac{2.303 \times A}{l}, \qquad \text{………………………...……. (5.1)}$$

where A is the absorbance obtained from the absorption spectra, and l is the thickness of the film. The film thickness was estimated using cross-sectional SEM imaging and found to be around 1500 nm for all the films reported in this chapter.

Fig.5.14 (a) shows the variation of room temperature absorption coefficients deduced from the absorption spectra of the $Zn_{1-x}Mg_xO$ (x=0.19, 0.25, 0.34 and 0.60) films with photon energy. The excitonic nature of the pulsed laser deposited $Zn_{1-x}Mg_xO$ films (for $x \leq 0.34$) is clearly apparent at the room temperature. For the cubic phase $Zn_{1-x}Mg_xO$ films ($x \geq 0.60$) no excitonic transition in the absorption spectra was observed.

The wurtzite ZnO conduction band is mainly constructed from the *s*-like state having Γ_7^c symmetry, whereas the valence band is a *p*-like state, which splits into three bands due to the influence of crystal-field and spin-orbit interactions [215]. The near-band-gap intrinsic absorption and emission spectrum is therefore dominated by transition between these three valence bands and the conduction band.

The related free-exciton transitions from the conduction band to these three valence bands or vice versa are usually denoted by *A* (referred to as the heavy hole), *B* (referred to as the light hole), and *C* (referred to as crystal-field split band). In the pure ZnO film (x=0), even at room temperature, A, and B, excitons are clearly distinguished. In the $Zn_{1-x}Mg_xO$ wurtzite phase ($0 \le x \le 0.34$), the exciton peaks are broadened due to alloying but still the individual excitons can be clearly distinguished. The excitonic feature in the absorption spectra is a consequence of the high binding energy (~60 meV) of the exciton in $Zn_{1-x}Mg_xO$ alloys and the high crystalline quality of the films [216]. In the previous reports on pulsed laser deposited $Zn_{1-x}Mg_xO$ thin films [217-219], the exciton peak at room temperature was only visible in the unalloyed ZnO film. In the alloy films, the absorption edge was broad and the exciton structure was not apparent. The excitonic emission from $Zn_{1-x}Mg_xO$ ($x \le 0.2$) nanowire arrays grown using HPLD (high pressure pulsed laser deposition) technique is reported earlier [220]. In the present work, as shown in Figure 5.14 (a), the exciton peaks remains present for all alloy compositions having (0002) orientation even though alloy broadening reduces the slope of the absorption edge with increasing Mg concentration.

The optical transitions are allowed for A-, B- and C- excitons if the electric field **E** of the electromagnetic wave is perpendicular to the c-axis (**E⊥c)**. When electric field is parallel to the c-axis (**E║c)**, the transitions are forbidden for the B-exciton, and allowed for A- exciton and C- exciton. During absorption measurements in the present case, the incident beam was normal to the sample surface and electric field **E** of the incident radiation was perpendicular to the c-axis of the thin films. All the three exciton series contributed to the absorption spectra having large oscillator strength of A- and B-excitons and small oscillator strength of C-exciton [221]. The absorption spectra of ZnO and $Zn_{1-x}Mg_xO$ thin films with exciton contributions can be modeled as [222, 223],

…………………..……. (1)

where n is the index of the valence bands, E_{0n} is the bandgap energy, R_n is the exciton binding energy, $\Gamma_{ex,m}$ is a broadening parameter of the m*th* excited exciton state, and A_{0n}^{ex} is an adjustable fitting parameter.

For the continuum absorption above the bandgap, the Absorption coefficient can be summed as [223],

…….. (2)

The last term in the bracket is broadening function, in which Γ_n is an additional parameter used to smooth the discontinuity at the band gap. The exciton energy gap, binding energy, and broadening parameter were obtained for different compositions by fitting the above equations for the respective absorption spectrums. The variation in exciton band gap, binding energy and broadening parameter with Mg content is shown in Fig. 5.14 (b), (c) and (d) respectively. The bandgap of the hexagonal $Zn_{1-x}Mg_xO$ thin films found to be increasing with Mg content from 3.3 eV (x=0.0) to 4.2 eV (x=0.34) as shown in Fig. 5.14 (b). The exciton binding energies, Fig.5.14 (c), decreased with the Mg content from 61 meV (x = 0.00) to 46 meV (x = 0.34) in case of B-exciton, from 54 meV (x = 0.00) to 35 meV (x = 0.34) for A-exciton and from 50 meV (x = 0.00) to 26 meV (x = 0.34) in case of C-exciton.

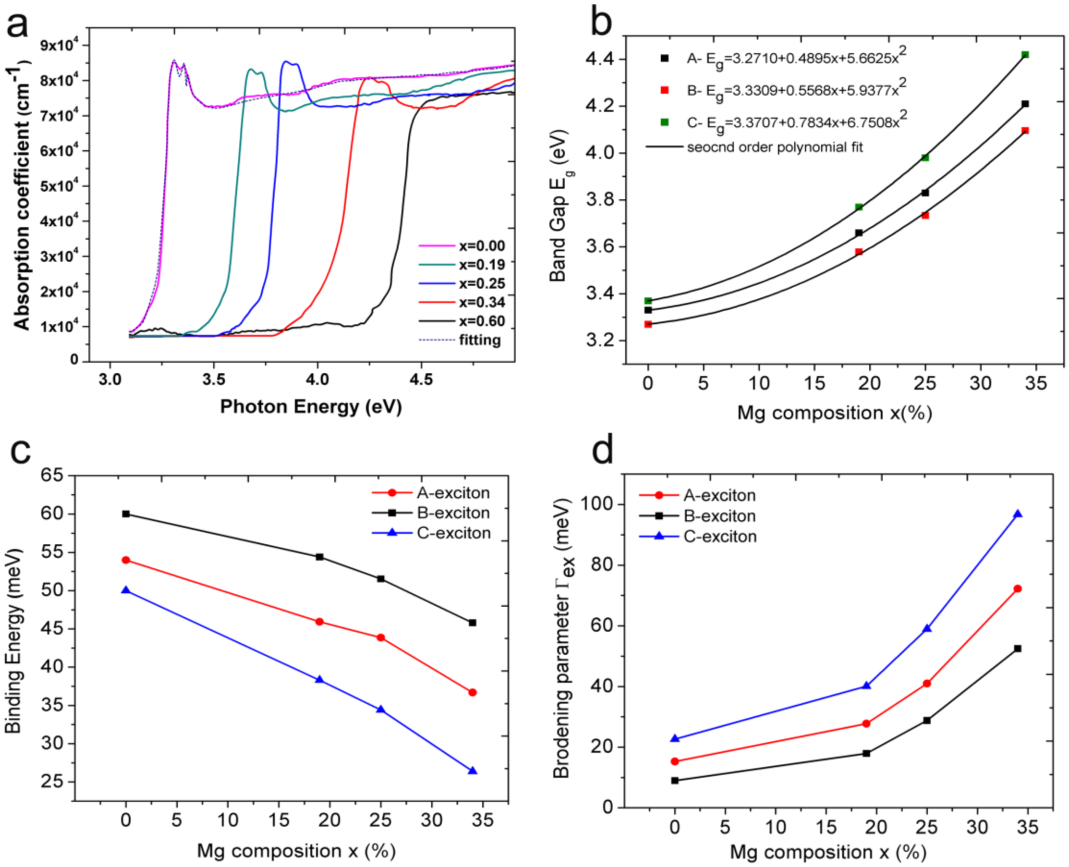

Fig.5.14 Variation of (a) absorption coefficients of $Zn_{1-x}Mg_xO$ (x =0.00, x=0.19, x=0.25, x=0.34, and x=0.60) thin films deposited via PLD at 700°C in 10^{-1} mbar O_2 pressure, with photon energy. (Theoretical fit for pure ZnO using eq.1 and 2 is shown by dotted line); (b) bandgap energy (solid line represents second order polynomial fitting); (c) exciton binding energy; (d) broadening parameter, of $Zn_{1-x}Mg_xO$ thin films with Mg composition (x)

The decrease in excitonic binding energies with Mg doping can be attributed to lattice disorder induced due to lodging of Mg at interstitial positions and creation of additional oxygen defect centers as shallow donors. Due to increasing cloud of such defects within the lattice, the attraction between photoexcited carriers with opposite charge i.e. the coulomb attraction will be reduced because of Vander Waals interaction with neutral defect centers. This additional interaction will reduce the exciton binding energy between a free electron and a free hole and efficiently traps excitons to form bound excitons. Also, the broadening parameter $\Gamma_{ex,m}$ was increased for $Zn_{1-x}Mg_xO$ films having higher Mg content due to alloy broadening as shown in Fig.5.14 (d) for all the three excitons.

Fig.5.15 (a) shows absorption spectra of $Zn_{1-x}Mg_xO$ (x=0.25) thin film deposited at different substrate temperatures. A blue shift in absorption edge of $Zn_{0.75}Mg_{0.25}O$ thin films is observed with increase in substrate temperature. At high substrate temperature substitution ratio of Mg on Zn sites increases and so the bandgap energy and hence the absorption edge is blue shifted. Fig.5.15 (b), (c) and (d) shows the variation of exciton energy gap, binding energy, and broadening parameter, respectively, of $Zn_{0.75}Mg_{0.25}O$ thin films with deposition temperature. The exciton energy gap of $Zn_{1-x}Mg_xO$ thin films enhanced from 3.47 to 3.59 eV (A exciton), 3.50 to 3.62 eV (B exciton) and 3.54 to 3.64 eV (C exciton) with increase in deposition temperature, as shown in Fig.5.15 (b). The exciton binding energy increased from 24 to 52 meV (A exciton), 28 to 60 meV (B exciton), and 22 to 48 meV (C exciton) while broadening parameter decreased from 102 to 23 meV (A exciton), 81 to 12 meV (B exciton), and 130 to 34 meV (C exciton) with increase in deposition temperature from 400^o C to 700^o C, respectively [Fig.5.15 (c) and (d)]. This can be attributed to highly oriented nature and good crystalline quality of $Zn_{1-x}Mg_xO$ thin films deposited at higher temperatures.

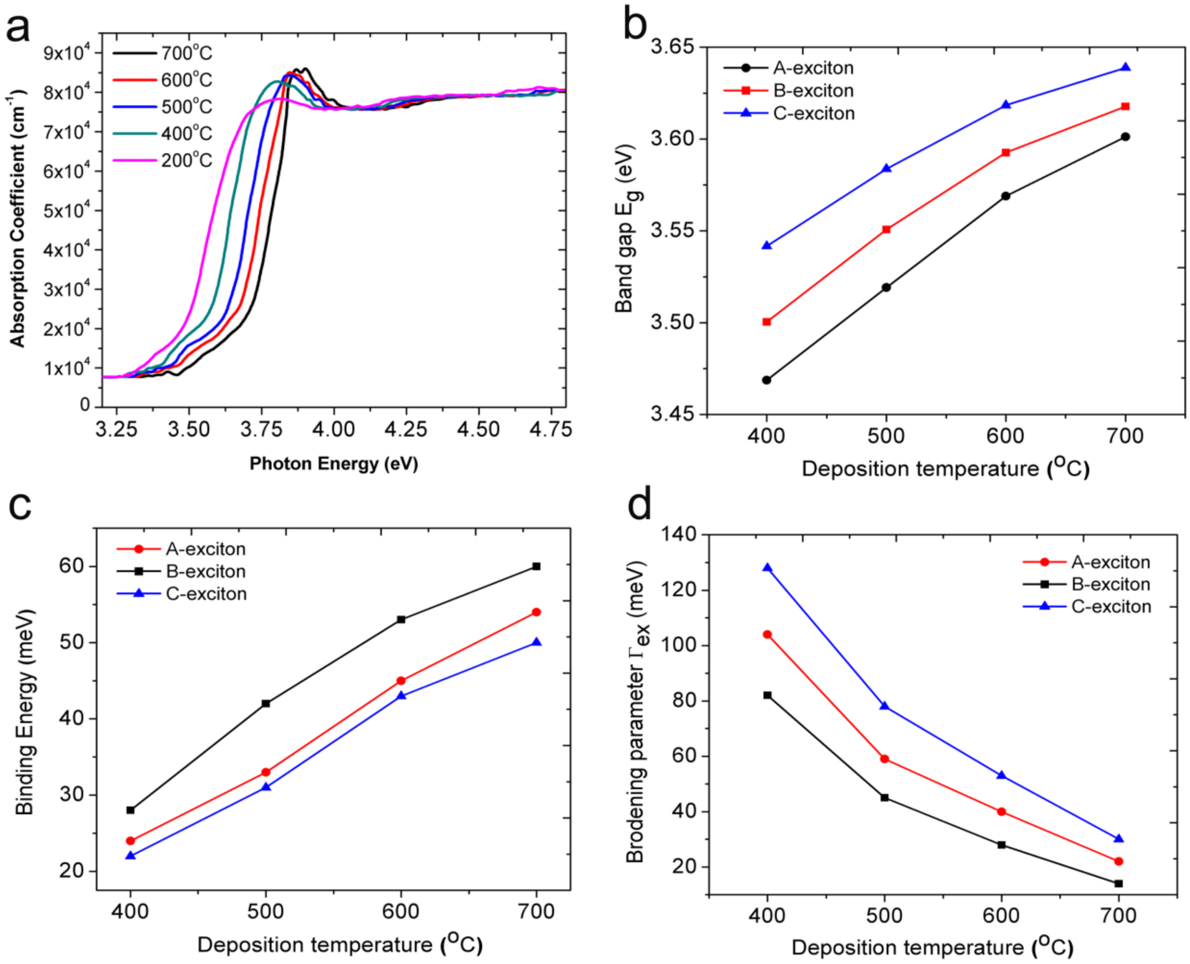

Fig.5.15 Variation of (a) absorption coefficients; (b) bandgap energy (solid line represents second order polynomial fitting); (c) exciton binding energy; (d) broadening parameter, of $Zn_{1-x}Mg_xO$ (x=0.25) thin films with deposition temperature

Fig.5.16 (a) shows the photoluminescence (PL) spectra of the $Zn_{1-x}Mg_xO$ thin films for different Mg content (x=0 to 0.34). The excitation wavelength and intensity were kept same for all the PL measurements. The photoluminescence from the alloyed samples was of comparable intensity to that of unalloyed ZnO (0002) oriented thin films deposited via pulsed laser deposition technique. The excitonic emissions were observed in all the $Zn_{1-x}Mg_xO$ thin films. For clarity, Lorentzian fit for all the three excitons is shown by broken lines in Fig.5.16 (a) for pure ZnO. The peak position of the emission band increases to the higher energy side with Mg concentration in the film due to increase in the band gap. The FWHM of PL band increases with Mg content from 22 nm (x=0.00) to 43 nm (x=0.34). PL broadening mechanism may be related to lattice disorder caused by Mg doping and scattering of the excitons with the defects.

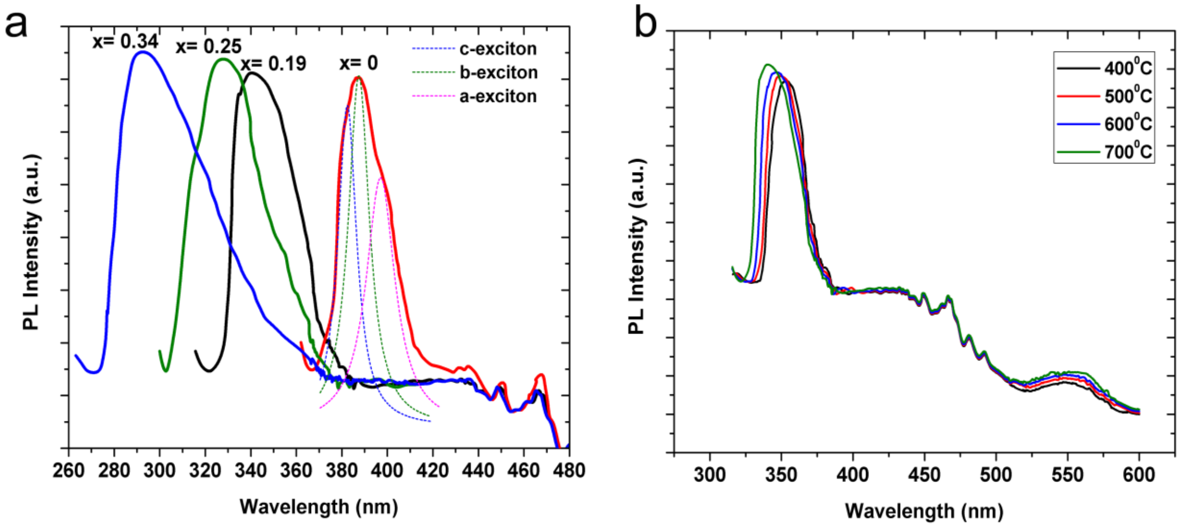

Figure.5.16 Photoluminescence spectra of (a) $Zn_{1-x}Mg_xO$ thin films deposited at 700^{o}C with varying Mg content (x); (b) $Zn_{1-x}Mg_xO$ (x = 0.19) thin films deposited at different substrate temperatures.

Fig.5.16 (b) shows Photoluminescence spectra of $Zn_{1-x}Mg_xO$ (x=0.19) thin films deposited at different temperatures. Similar to absorption spectra, a blue shift in PL peak position is observed with increase in substrate temperature. Intensity of PL in UV region was found to be increasing with substrate temperature. Increase in UV peak intensity can be attributed to better crystalline structure and columnar growth of $Zn_{1-x}Mg_xO$ thin films at higher substrate temperatures. In addition to UV emission, a broad green luminescence was also observed centered around 540 nm which is related to the oxygen vacancies in ZnO crystals [224]. This deep level defect-related luminescence is caused by radiative transitions between shallow donors (related to oxygen vacancies) and deep acceptors (Zn vacancies) [225]. As the substrate temperature increases, the density of oxygen vacancies as shallow donors increases. With the increase of oxygen vacancies, the zinc vacancies may also increase resulting in the pronounced emission of the green luminescence due to the donor (oxygen vacancy)-acceptor (zinc vacancy) transition.

5.4 Effect of substrate annealing on the quality of pulsed laser deposited $Zn_{1-x}Mg_xO$ thin films

In order to further improve upon the epitaxial growth and surface quality of $Zn_{1-x}Mg_xO$ thin films, sapphire substrates were annealed prior to the deposition of the film. The annealing of substrates results into the ultra-smooth surfaces with atomic steps [226, 227]. These well defined atomic steps acts as a nucleation center, facilitating the hexagonal growth of the thin film.

Figure.5.17 (a) and (b) shows the AFM images of the surface of the polished unannealed and annealed sapphire substrates respectively. For the substrate without annealing, there were irregular small corrugations ranging over the entire surface, as shown in Fig. 5.17 (a). The AFM image of sapphire substrate annealed at 1200 ◦C for 2 hr shows the drastic change in surface morphology as shown in Fig.5.17 (b). The terrace like structure on the substrate surface with atomic steps was formed after annealing. The possible mechanism of step formation over annealed sapphire surface can be explained as follows: the lattice structure of α-Al_2O_3 along <0001> direction can be described by a succession of distorted hexagonal compact layers of oxygen atoms sandwiching between two close layers of aluminium atoms. The hexagonal unit cell height comprises of six layers of oxygen and six such double layers of aluminium. Upon high temperature annealing, total surface energy of (0001) Al_2O_3 surface tend to increase. In order to maintain a lowest surface energy state, atomic layers of Al and O shift in a direction determined by the miscut orientation of α-Al_2O_3. Initially at low annealing temperatures, formation of monosteps with c/6 height takes place, where c is the lattice constant of Al_2O_3. Further increase in temperature gives rise to coalescence process which involves "zipping" of monosteps into a double height step.

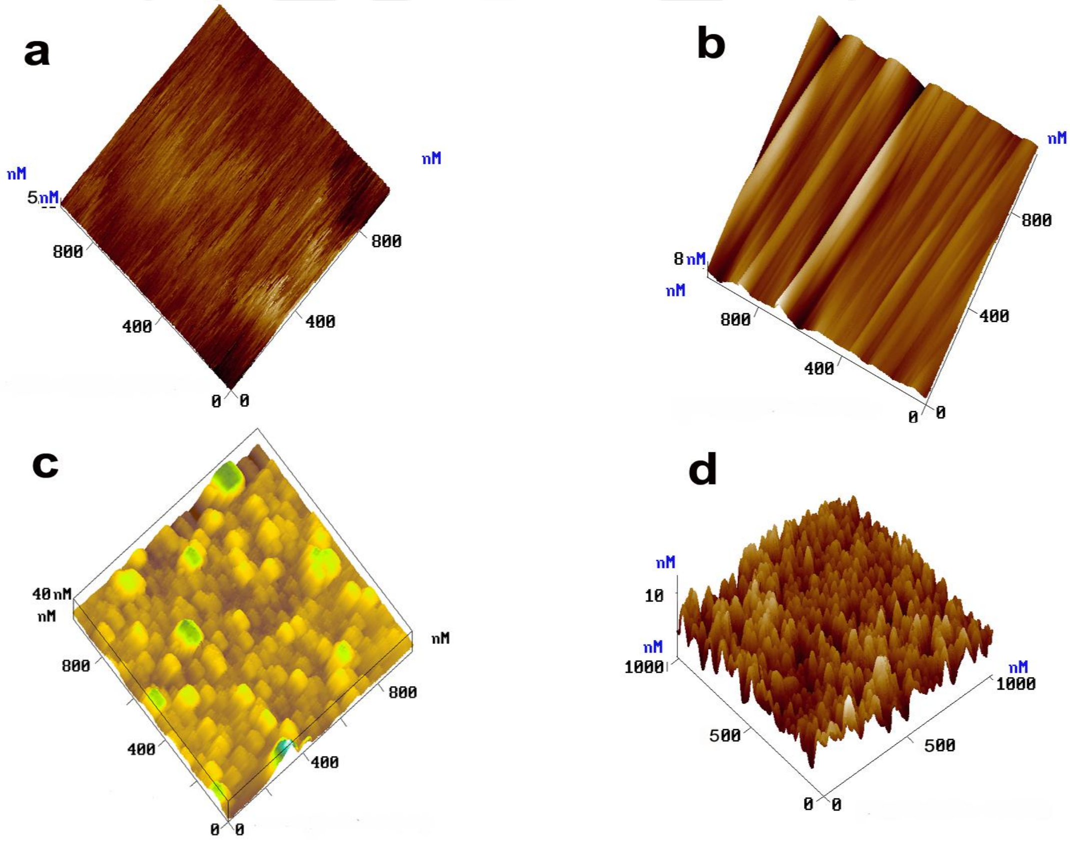

Figure.5.17 AFM scans of (a) unannealed sapphire surface, (b) 1200^{o}C annealed sapphire surface, (c) $Zn_{1-x}Mg_xO$ (x=0.1) thin film surface deposited on unannealed sapphire, (d) $Zn_{1-x}Mg_xO$ (x=0.1) thin film surface deposited on 1200^{o}C annealed sapphire.

At temperatures $\geq$ 1200° C , the growth of multiheight steps results from direct coalescence of lower multiple steps and from displacements of monosteps originated from the thermal parting of multi height steps [228, 229]. Fig.5.17(c) and 5.17(d) shows AFM scans of pulsed laser deposited $Zn_{1-x}Mg_xO$ (x =0.1) thin films on unannealed and 1200^{o}C annealed sapphire substrates respectively. The rms roughness for $Zn_{1-x}Mg_xO$ (x=0.1) films deposited on annealed sapphire was ~ 3nm as compared to that of ~ 6nm for unannealed sapphire.

SEM images of $Zn_{1-x}Mg_xO$ (x=0.1) thin films deposited at 700^{o}C on unannealed and annealed (0001) sapphire substrates are shown in Figure.5.18 (a) and (b), respectively. The columnar hexagonal growth of $Zn_{1-x}Mg_xO$ thin films is clearly visible in both the films. The $Zn_{1-x}Mg_xO$ (x=0.1) thin films deposited on unannealed sapphire showed slanted columnar growth and uneven top surface. Where as $Zn_{1-x}Mg_xO$ films deposited on annealed sapphire showed excellent vertical growth with very clean top surface profile.

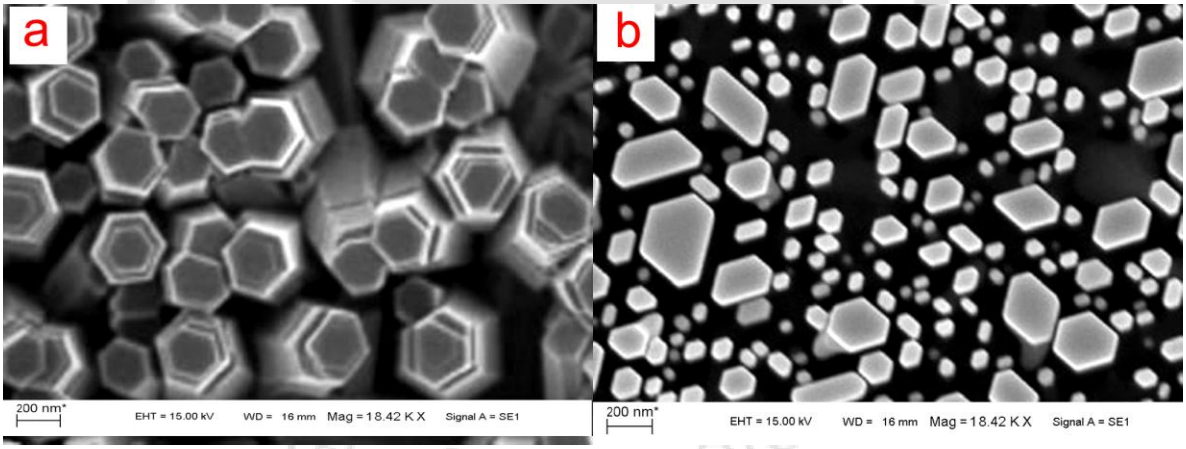

Figure.5.18 SEM images of $Zn_{1-x}Mg_xO$ (x=0.1) films deposited on (a) unannealed sapphire, (b) 1200^{o}C annealed sapphire

The annealing at high temperature resulted in the formation of atomic steps on the substrate surface with reduced surface energy state. The formation of the terrace structure is probably the origin of the growth of the highly c-axis oriented film, as well-defined steps of the sapphire substrate can act as preferred nucleation sites for film growth. Thus terrace structure facilitates smooth vertical columnar growth and reduces the strain in column formation during the growth of $Zn_{1-x}Mg_xO$ other than those caused by the lattice mismatch.

Figure.5.19 shows the X-ray diffraction (XRD) of $Zn_{1-x}Mg_xO$ films deposited on unannealed (0001) sapphire substrates and annealed (0001) sapphire substrates. All the films showed a preferential *c*-axis orientation (0002).

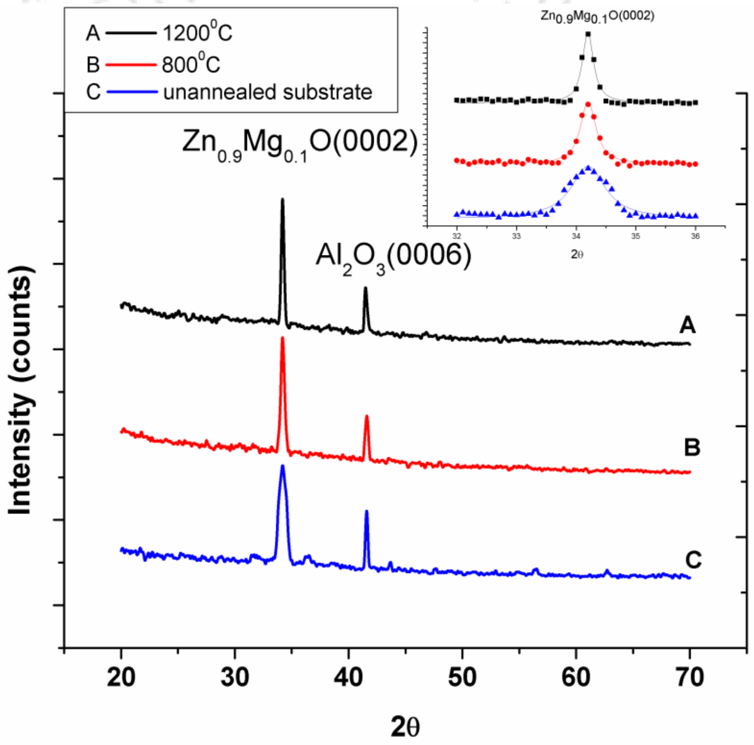

Figure.5.19 XRD patterns of $Zn_{1-x}Mg_xO$ (x=0.1) films deposited at 700°C substrate temperature on unannealed and annealed sapphire substrates (inset shows expanded view of $Zn_{0.9}Mg_{0.1}O$ (0002) peak)

The intensity of the (0002) $Zn_{1-x}Mg_xO$ peak on annealed sapphire substrates was larger than that of the unannealed sapphire substrate. The FWHM of the (0002) $Zn_{1-x}Mg_xO$ peak on annealed sapphire substrates was smaller than that of the unannealed sapphire substrate. The intensity of the (0002) $Zn_{1-x}Mg_xO$ peak in the XRD spectra increased with increasing annealing temperature of sapphire substrate, while the FWHM values of the (0002) $Zn_{1-x}Mg_xO$ peak decreased. This observation confirmed that the annealing of the sapphire substrate prior to film deposition can improve the $Zn_{1-x}Mg_xO$ film quality grown by pulsed laser deposition.

Figure.5.20 shows the PL spectra of $Zn_{1-x}Mg_xO$ (x=0.1) films deposited on to the unannealed and annealed substrates at 800°C and1200°C respectively. The PL spectra showed a strong UV emission having peak at 364 nm. The intensity of UV emission peak is higher on annealed sapphire substrates and increases with the annealing temperature. This can be related to the vertical columnar growth of the $Zn_{1-x}Mg_xO$ films deposited on substrates annealed at high temperature prior to deposition.

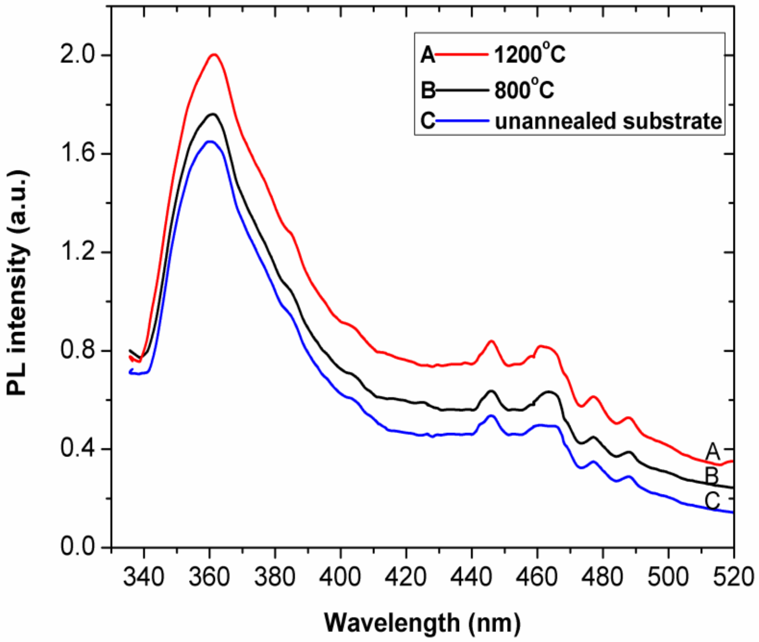

Figure.5.20 PL spectra of $Zn_{1-x}Mg_xO$ (x=0.1) films deposited at 700°C substrate temperature on unannealed and annealed sapphire substrates

5.5 Conclusion

ZnO thin films were deposited via PLD on Si (100) substrates in O_2 ambient. Structural and optical characterizations of ZnO thin films revealed an optimum value of O_2 pressure in the range of 10^{-3} mbar to 10^{-1} mbar and target substrate distance more than 20 mm to make smooth cluster free stochiometric ZnO films.

The high quality (0002) - oriented crystalline $Zn_{1-x}Mg_xO$ films were deposited on (0001) sapphire substrates using PLD technique. XRD and Raman studies confirmed wurtzite structure of $Zn_{1-x}Mg_xO$ alloy films up to 34 % Mg concentration and cubic phase for 60 % and above of Mg concentration. E_2^{high} mode (in Raman spectra) showed asymmetric line broadening and peak shift towards lower frequencies upon increase in Mg concentration. The c – axis lattice constant was found to decrease slightly with increase in Mg concentration. Room temperature excitonic emission was observed from the c-axis oriented $Zn_{1-x}Mg_xO$ ($0.0 \leq x \leq 0.34$) thin films. Effect of Mg concentration and Mg doping on the exciton band gap, exciton binding energy, and broadening parameter was studied from the absorption spectra. The optical band gap was successfully tuned from 3.3 to 4.6 eV by adjusting the Mg content ($x = 0.0$ to $x= 0.60$). The annealing of the sapphire substrate prior to the deposition enhanced columnar growth and crystallinity of the $Zn_{1-x}Mg_xO$ films. The enhancement in UV-PL signal is observed for films deposited on substrates annealed at higher temperatures.

Chapter 6

Non-linear optical properties of pulsed laser deposited $Zn_{1-x}Mg_xO$ thin films

Zinc oxide in the form of crystal as well as thin film shows 2nd and 3rd order non linear optical behavior [230, 231]. The non-linear optical properties in thin films are particularly attractive as it can find direct applications in the integrated non linear optical devices [89, 90]. In chapter 5, it was shown that pulsed laser deposited thin films of $Zn_{1-x}Mg_xO$ ($0 \leq x \leq 0.34$) at 700° C in 0.1 mbar O_2 ambient, are highly c-axis oriented with hexagonal wurtzite structure. The hexagonal wurtzite structure belongs to non-centrosymmetric point group and hence, $Zn_{1-x}Mg_xO$ thin films are also expected to show non linear properties and harmonic generation. Non linear absorption and second harmonic generation (SHG) in $Zn_{1-x}Mg_xO$ thin films will be governed by the Mg content (x) because, with increase in Mg concentration levels, lattice structure of ZnO will change. In this chapter, harmonic generation and measurement of nonlinear absorption coefficient, nonlinear refractive index and third order susceptibility of pulsed laser deposited thin films of $Zn_{1-x}Mg_xO$ are discussed.

6.1 Harmonic generation in $Zn_{1-x}Mg_xO$ thin films

SHG in $Zn_{1-x}Mg_xO$ (x = 0.0, 0.01, 0.02, 0.05, and 0.1) thin films (deposited via PLD on to fused silica substrates at 700° C at 0.1 mbar O_2 pressure) was recorded using setup described in Chap.2, Sec 2.8. The fundamental (1064 nm) wavelength of Q-switched Nd:YAG laser was used for pumping. The angle of incidence of pump beam was found to be around 30° for maximum SHG output. Fig.6.1 shows the SHG and third harmonic generation (THG) at 532 nm and 355 nm, respectively, in pure ZnO thin film. Pump threshold for THG was 85 MW/cm^2 and that for SHG was at a lower value of 64 MW/cm^2. No THG emission was observed from $Zn_{1-x}Mg_xO$ ($x \neq 0$) thin films. SHG and green band emission spectrum for $Zn_{1-x}Mg_xO$ thin films for different Mg concentration (x) is shown in Fig. 6.2.

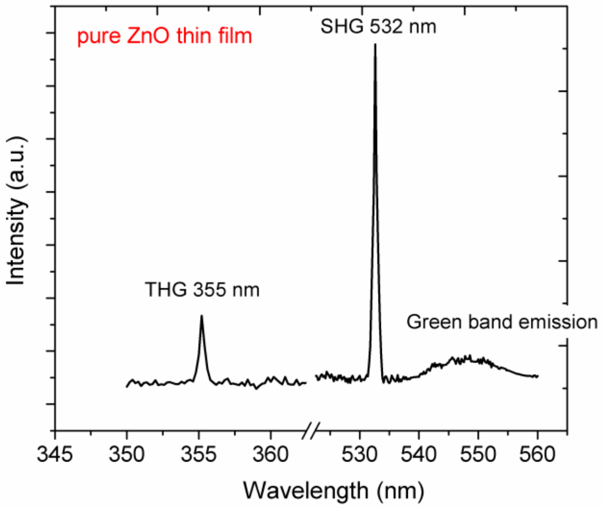

Figure 6.1 SHG and THG observed from pure ZnO thin films using 1064 nm excitation (Laser intensity 85 MW/cm^2)

SHG intensity was observed to be rapidly decreasing with increased Mg content as shown in Fig.6.2, whereas defect related green band emission was increased slightly. For $Zn_{1-x}Mg_xO$ thin films, having more than 10% of Mg content, SHG signal was very weak and couldn’t be recorded. This can be attributed to the degradation of wurtzite lattice structure of ZnO upon Mg-doping. This was also confirmed by micro Raman studies, as discussed in Chapter.5, Sec 5.3.2.

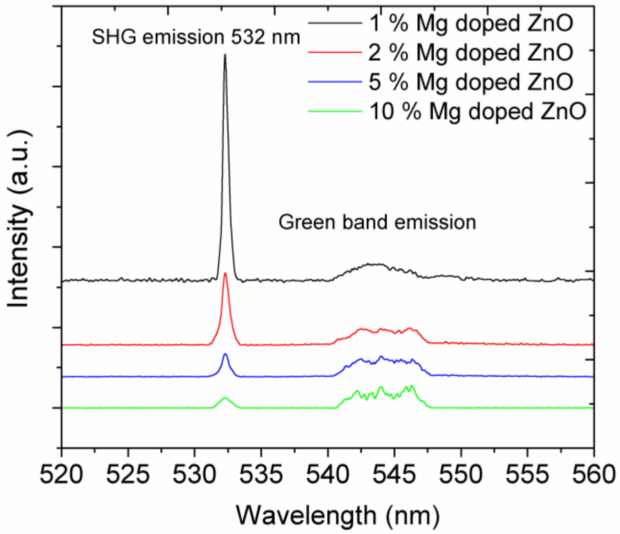

Figure 6.2 SHG and green band emission from $Zn_{1-x}Mg_xO$ ($0.01 \leq x \leq 0.10$) thin films with different Mg content

The defect-related green band emission, caused by radiative transitions between the oxygen vacancies and Zn interstitials in ZnO crystals [224], is also observed upon excitation with 1064 nm. Upon alloying between MgO and ZnO, number of oxygen vacancies increased due to insertion of Mg interstitials into ZnO lattice but number of Zn interstitials decreased. This gives rise to slight increase in green band emission intensity for $Zn_{1-x}Mg_xO$ thin films. Overall, the ratio of SHG to green band emission intensity was decreased with increase in Mg content, shown in Fig. 6.3.

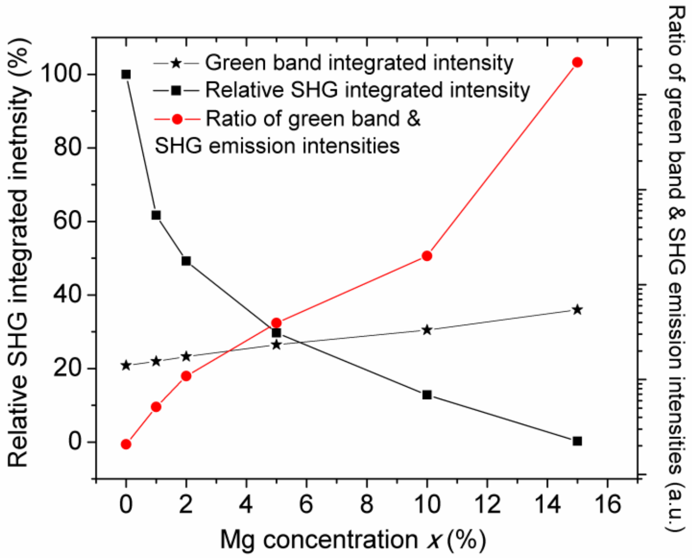

Figure 6.3 Variation of relative SHG integrated intensity (w.r.t to pure ZnO thin films) green band intensity and green band to SHG emission ratio of $Zn_{1-x}Mg_xO$ *(*$0.00 \leq x \leq 0.15$*) thin films with Mg content*

6.2 Multiphoton absorption induced UV emission from $Zn_{1-x}Mg_xO$ thin films

Multiphoton absorption induced multiple emission peaks in UV-region were observed in the PL spectra of pulsed laser deposited $Zn_{1-x}Mg_xO$ thin films, Fig. 6.4, using the experimental setup of Fig. 2.7. It can be attributed to deep level emissions originating from excited states in conduction band as well as excited state absorption to various meta-stable states following three photon absorption [232] and emitting the band spectra in UV region. In case of ZnO, the free exciton UV emission was centered around 388 nm which shifted gradually to 366 nm upon 10 % of Mg doping. The broadening of the multiphoton absorption induced PL indicated degradation of wurtzite ZnO lattice upon Mg doping.

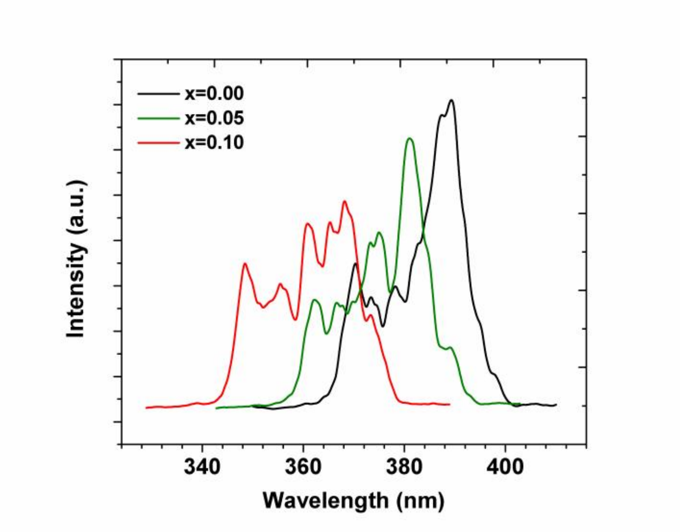

Figure 6.4 Multiphoton absorption induced UV-PL spectra for ZnO and $Zn_{1-x}Mg_xO$ (x=0.05; x=0.10) films

Mg content x (%)	**Peak position (nm)**
0	388.0
5	381.0
10	366.6

Table 6.1 UV-PL peak position of $Zn_{1-x}Mg_xO$ films with different Mg content (x)

6.3 Nonlinear absorption coefficient and nonlinear refractive index of $Zn_{1-x}Mg_xO$ thin films

The non-linear absorption coefficient and non-linear refractive index of $Zn_{1-x}Mg_xO$ thin films were measured by open and close z-scan technique, respectively (described in Sec. 2.8 of Chapter.2). Z-scan measurements were performed for pure ZnO thin film and four $Zn_{1-x}Mg_xO$ samples with 1%, 2%, 5% and10% Mg content deposited on fused silica substrate. The z-scan for fused silica substrate is shown in Fig 6.5 (a), confirms the absence of any non-linear absorption.

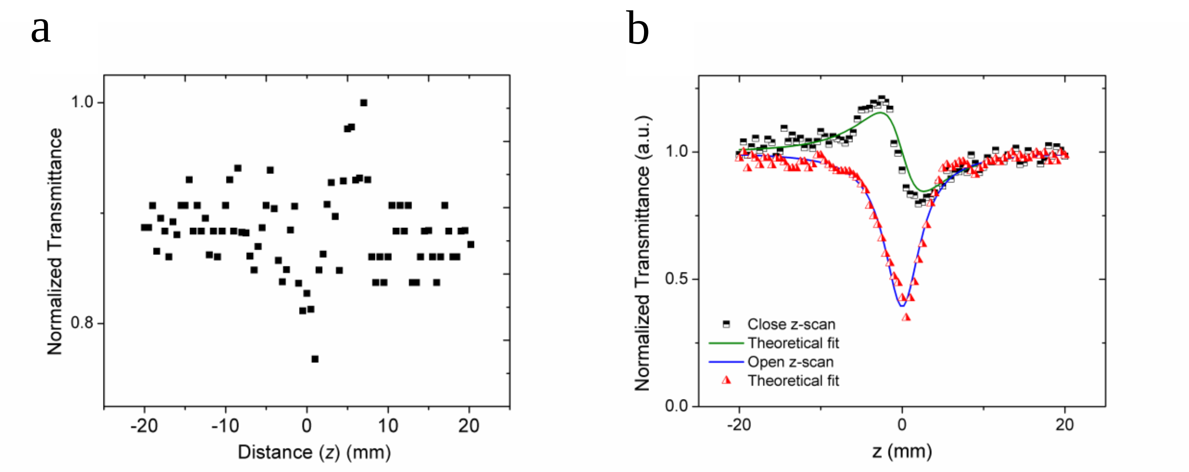

Figure 6.5 Open z-scan curve for (a) Fused silica substrate; Open and close z-scan curves for (b) pure ZnO thin films

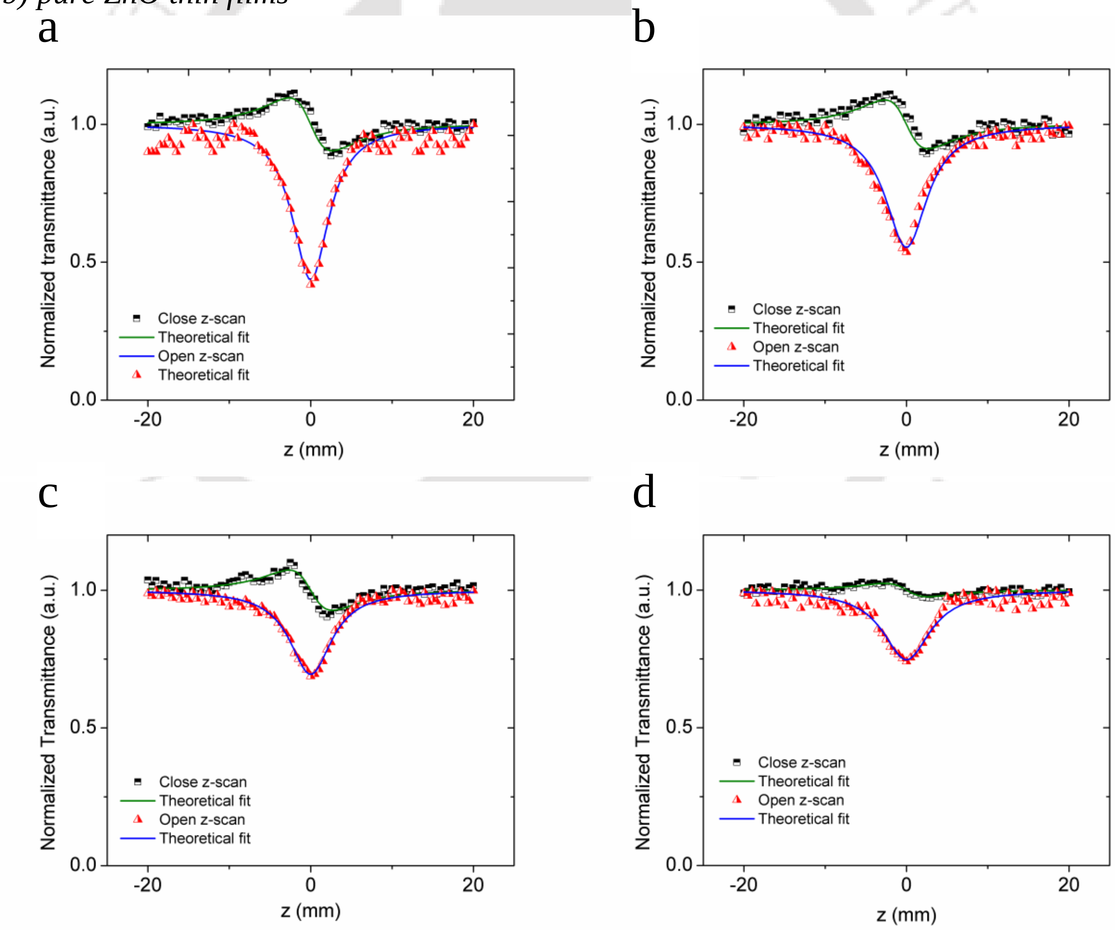

Figure 6.6 Open and close z-scan curves for $Zn_{1-x}Mg_xO$ *thin films with (a) 1% Mg; (b) 2% Mg; (c) 5% Mg; and (d) 10 % Mg. (Symbols and solid line represent experimental data and theoretical fit, respectively)*

The open and close z-scan curves for pure ZnO thin film are shown in Fig.6.5 (b) and corresponding curves for $Zn_{1-x}Mg_xO$ thin films with different Mg content are shown in Fig.6.6. The theoretical fittings corresponding to eq. 2.5 and eq. 2.6 (Chapter 2) are also shown in the same figure by solid line. The non-linear absorption coefficient β, non-linear refractive index n_2 and third order non-linear susceptibility $\chi^{(3)}$ of $Zn_{1-x}Mg_xO$ thin films were calculated from these curves using eq. 2.5, eq. 2.6 and eq. 2.9, respectively. These values are listed in Table 6.2. The data confirms that NLO properties of the $Zn_{1-x}Mg_xO$ thin films decrease with increase in Mg content.

Mg concentration (x) (%) in $Zn_{1-x}Mg_xO$ thin films	**Nonlinear absorption β (cm/GW)**	**Nonlinear refractive index n_2 (10^{-13} cm^2/W)**	**Nonlinear susceptibility $\chi^{(3)}$ (10^{-10} esu)**
0	194.59	11.2	1.41
1	180.36	6.93	1.05
2	142.95	6.42	0.89
5	97.89	5.28	0.68
10	81.13	1.75	0.39

Table 6.2 Values of various nonlinear optical coefficients obtained using z-scan for $Zn_{1-x}Mg_xO$ *thin films*

6.4 Conclusion

The second harmonic generation, MPA induced UV emission and Non-linear absorption co-efficient, nonlinear refractive index and third order nonlinear susceptibly in $Zn_{1-x}Mg_xO$ thin films were studied. The NLO properties of these films were found to be decreasing with increase in Mg content. All these effects can be attributed to ZnO lattice degradation upon Mg doping.

Chapter 7

Non-linear optical properties and Lasing action in ZnO nanorods

Nonlinear optical properties and harmonic generation in ZnO and $Zn_{1-x}Mg_xO$ ($0.0<x<0.10$) thin films were discussed in Chapter 6. In Chapter 5, bandgap tuning and excitonic UV-PL emission was reported for the well aligned, c-axis oriented $Zn_{1-x}Mg_xO$ ($0\leq x\leq 0.34$) thin films. Further to achieve lasing action, vertically oriented ZnO nanorod arrays were grown onto pulsed laser deposited ZnO seed layer. Vertically c-axis oriented, well-aligned ZnO nanorod arrays, having large surface to volume ratio, have been used for the fabrication of random nanolasers [233-235]. The strong transverse confinement of light in a nanorod reduces the out-of-plane emission. This enhances the carrier injection rate at the interface of ZnO nanorods, thereby improving the ultraviolet (UV) stimulated emission inside the random media. Arrays of ZnO nanorods can be grown by vapor phase processes [236] as well as by the wet chemical route or hydrothermal process [137]. Vapor phase processes generally require high temperatures, high vacuums, and involved infrastructure. In contrast to the vapor phase process, wet chemical methods are a low cost simple laboratory technique for growing the arrays of ZnO NRs.

In this chapter, the growth of aligned long ZnO nanorod arrays with a high aspect ratio on to pulsed laser deposited ZnO seed layer using a preheating hydrothermal process is presented. The effect of preheating time, growth time and seed layer on the density, the aspect ratio, the vertical orientation and the optical properties of ZnO nanorod arrays was investigated. The probable chemical growth mechanism of ZnO nanorod arrays is described. Multi photon absorption (MPA) induced near band edge UV amplified spontaneous emission (ASE) and second harmonic generation (SHG) emission were observed from these ZnO NRs using Q-switched Nd:YAG (1064 nm) laser as the pump. The pumping processes and intrinsic mechanisms for MPA-induced lasing action in ZnO NRs are discussed.

7.1 Experimental Details

The experimental details about hydrothermal growth of ZnO nanorods, grown on seed layer of ZnO, are discussed in Sec. 2.5. The thin film of ZnO seed layer was deposited on the fused silica substrate via PLD technique. ZnO thin films were deposited at a substrate temperature of 700^{o} C under 10^{-1} mbar oxygen pressure for a deposition time of one hour. The surface morphology of ZnO films and NRs were obtained by using scanning electron microscope. ZnO NRs were also analyzed using transmission electron microscope. Photoluminescence (PL) spectra of the ZnO thin films and NRs were recorded using fluorescence spectrometer with 300 nm line of Xe lamp as the excitation source. The multiphoton absorption induced harmonic generation and UV lasing action from ZnO NRs was recorded using the setup described in Sec. 2.7.

7.2 Effect of Pre-heating and seed layer on Hydrothermal Growth and Optical Properties of ZnO Nanorods

Fig.7.1 shows the top and cross-section SEM images of ZnO thin films deposited as seed layer via PLD on to fused silica substrates with the film thickness ~ 1 µm [Fig.7.1 (b)].

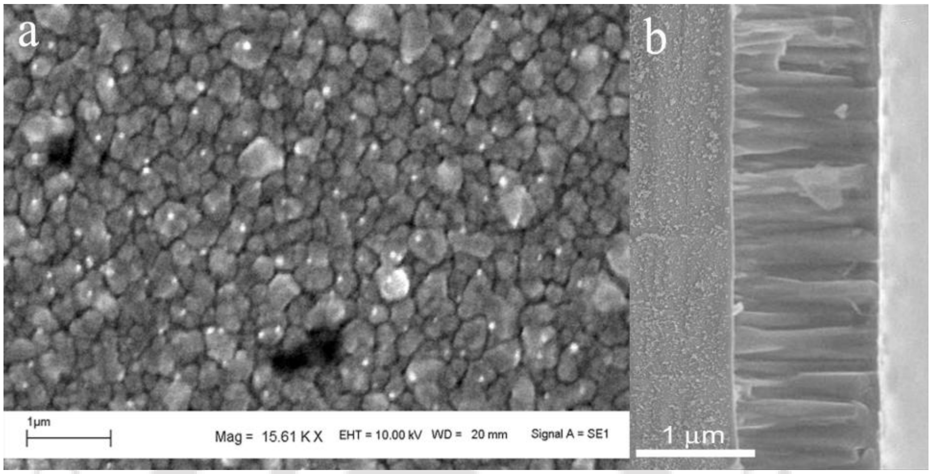

Figure 7.1 SEM images of ZnO seed layer deposited on to fused silica substrate at 700^{o}C (a) Top view (b) Cross-sectional view

The effect of pre-heating on the surface morphology, alignment and size distribution of ZnO NRs is shown in Figure 7.2. SEM image of ZnO NR bundles grown without pre-heating the solution is shown in Fig.7.2 (a). Without pre-heating the average diameter of randomly oriented NRs was around ~ 500 nm. In Fig.7.2 (b), cross sectional SEM image of ZnO NRs grown with 2 hr pre-heating and 12 hr growth time is shown. The ZnO NRs found to be slightly oriented along the vertical direction with average diameter of NRs ~ 150 nm and with an average length of ~ 1 µm. Upon increasing the pre-heating time to 6 hr, as shown in Fig.7.2 (c) and corresponding cross-sectional view in Fig.7.2 (d), the vertically aligned 3-4 µm long ZnO NRs with an average diameter of around 100 nm were obtained. As the pre-heating time was further increased to 10 hr, the vertical alignment of ZnO NRs got disturbed [Fig.7.2 (e)]. The average diameter ZnO NRs in this case was found to be around 200 nm. Thus it appears that 6 hours pre-heating time was optimal to grow the vertically aligned ZnO NRs. To analyze the effect of growth-time, NRs were grown for 6 hrs with optimal pre-heating time of 6 hrs. Fig 7.2 (f) shows the cross-sectional view of dense, uniform and vertically aligned ZnO NR arrays of about ~ 150 nm in diameter and with an average length of about 2-3 μm has been grown on the ZnO seed layer. Though the average length of NRs grown for 12 hrs at optimal pre-heating time [Fig.7.2 (d)] was large, there was large variation in their lengths. Whereas NRs grown for 6 hrs showed fairly uniform length [Fig.7.2.(f)]. These ZnO NRs were used for lasing action studies via multi-photon absorption.

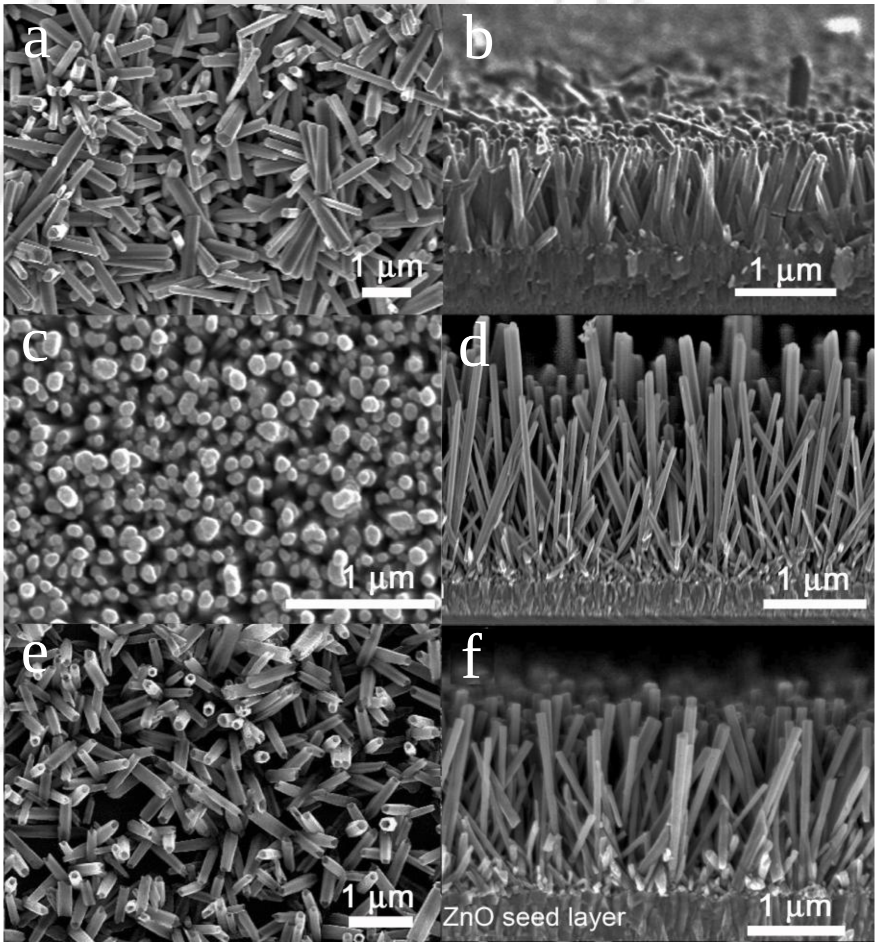

Figure 7.2 SEM images of ZnO NRs grown using ZnO seed layer (a) without pre-hating the solution (growth time 12 hrs), (b) for a growth time of 12 hr and with pre-heating of the solution for 2 hr; (c) growth time 12 hr, pre-heating time 6 hr; (d) growth time 12 hr, pre-heating time 6 hr (cross sectional view); (e) 12 hr growth time with 10 hr pre-heating and (f) 6 hr growth time with 6 hr pre-heating (cross-sectional view)

Fig. 7.3 (a) shows the TEM image of a single ZnO nanorod (6 hr growth time with 6 hr pre-heating) obtained by dispersing it into distilled water and then transferred on a carbon coated copper grid for microscopic analysis. The distribution of diameter for ZnO NRs was observed to be in the range of 50 nm to 200 nm. The corresponding selected area electron diffraction (SAED) pattern is shown in Fig.7.3 (b), confirming the single crystalline (0002) orientation for ZnO NRs. High resolution TEM (HRTEM) lattice image of the nanorod is shown in Fig.7.3 (c), further confirming single crystalline orientation. The lattice constant of ZnO NR calculated from HRTEM imaging was found to be approximately 0.522 nm matching with the literature [237].

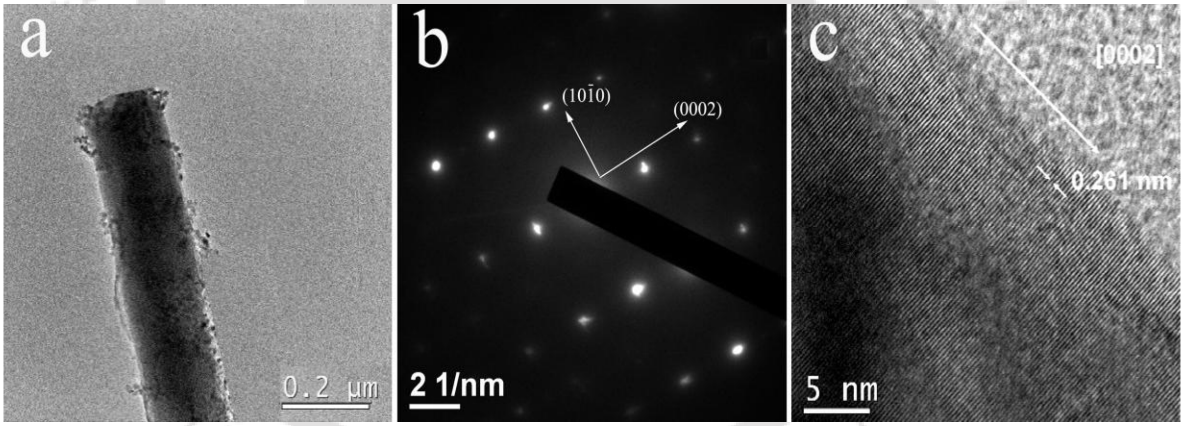

Figure 7.3 (a) TEM image of a single ZnO nanorod; (b) SAED pattern; (c) HRTEM lattice image

7.2.1 Growth Mechanism

In hydro-chemical thermal growth process, Zn^{2+} and OH^- are provided by hydration of Zinc Nitrate [$Zn(NO_3)_2$] and Hexamethylenetetramine [HMT], respectively. During the preheating process, following hydrothermal reactions can occur in the precursor solution:

$$2Zn(NO_3)_2 + 6H_2O \rightarrow 2Zn^{2+} + 4NH_3 + 9O_2(g) \quad (1)$$

$$(CH_2)_6N_4 + H_2O \rightarrow 4NH_3(g) + 6HCHO(g) \quad (2)$$

$$NH_3 + H_2O \rightarrow NH_4^+ + OH^- \quad (3)$$

Here, Zn^{2+} in the solution will react with OH^- to form soluble $Zn(OH)_2$ complexes, which act as the growth unit of ZnO nanostructures. Finally, ZnO is obtained by thermal decomposition of $Zn(OH)_2$ through following reactions:

$$Zn^{2+} + 2OH^- \leftrightarrow Zn(OH)_2(s) \quad (4)$$

$$Zn(OH)_2 \leftrightarrow ZnO(s) + H_2O \quad (5)$$

7.2.2 Effect of ZnO seed layer. For the growth of vertically aligned ZnO nanorods with high aspect ratio, homogeneous nucleation of bulk ZnO within the precursor solution must be suppressed and heterogeneous nucleation on preferably c-axis oriented ZnO seeds has to be promoted. Initially, without pre-heating, the degree of super saturation of the precursor solution is very high and homogeneous nucleation of bulk ZnO in solution occurs predominantly [238]. After preheating for 6 hr and more, at the initial growth stage, the degree of super saturation of the growth precursor is reduced and homogeneous nucleation in solution becomes difficult [239]. The presence of the ZnO seed layer can effectively lower the nucleation energy barrier, and heterogeneous nucleation easily occurs on the seed layer due to the matching lattice structure and the polar nature of the PLD-ZnO seed layer [240]. In addition, the surface roughness of the ZnO seed layer not only provides nucleation sites, but also limits the migration of the available nucleation sites. Hence, the more nucleation sites on the seed layer, the higher will be the nanorod density and alignment level with the larger aspect ratio.

7.2.3 Effect of pre-heating. During the hydrothermal growth process, the zinc concentration in the precursor solution linearly decreases with preheating and growth time due to the formation of ZnO crystals on to the seed layer as well as precipitation in the solution via the reactions explained above. A low zinc concentration is favorable for the formation of ZnO nanorods with smaller diameter [241]. The decrease in the diameter and increase in aspect ratio of ZnO nanorods with the reduction of the zinc precursor concentration is due to the dissolution, re-growth and transport limitation in the solution. Following the growth of ZnO nanorods, the chemical reaction in equation (5) moves to the left because of decomposition of ZnO into zinc ions again. These decomposed zinc ions directly transfer to the vicinal Zn terminated polar (0001) planes available on to the ZnO seed layer surface with high chemical activity. This results in a decrease of the diameter and a quick increase in the length and aspect ratio of the ZnO NRs.

7.2.4 Effect of HMT. After the preheating process residual hexamine, being a non-polar chelating agent, would preferentially attach to the non-polar facets of the ZnO nanorods/wires. This will lead to exposure of only the polar Zn-terminated (0001) plane for epitaxial growth [242], which also promotes the growth along the [0001] direction and drives the formation of small ZnO nanorods/wires with high aspect ratio.

7.3 XRD and Raman spectra of hydrothermally grown ZnO NRs on pulsed laser deposited (PLD) seed layer of ZnO

The XRD patterns of ZnO NRs and pulsed laser deposited ZnO thin films used as seed layer is shown in Figure 7.4. The PLD ZnO thin film seed layer show hexagonal wurtzite phase with a preferential c-axis orientation [Fig. 7.4 (A)]. ZnO NRs grown without the seed layer were preferentially (100) orientated as shown in Fig. 7.4, plot B.

After the aqueous chemical growth of ZnO on to the seed layer, highly c-axis oriented nanorod arrays were formed, as confirmed by an intense (002) peak in the XRD pattern of ZnO NR samples [Fig. 7.4. (C) to Fig.7.4 (H)]. The ZnO seed layer provides the well defined nucleation centers for the hydro thermal growth of c-axis vertically aligned ZnO nanorods.

The effect of preheating time on ZnO NR orientation can also be seen in Fig.7.4. The intensity of (002) peak initially increases with preheating time up to 6 hr but with further increase in preheating time up to 10hr it was observed to decrease, Fig. 7.4, plot F & G.

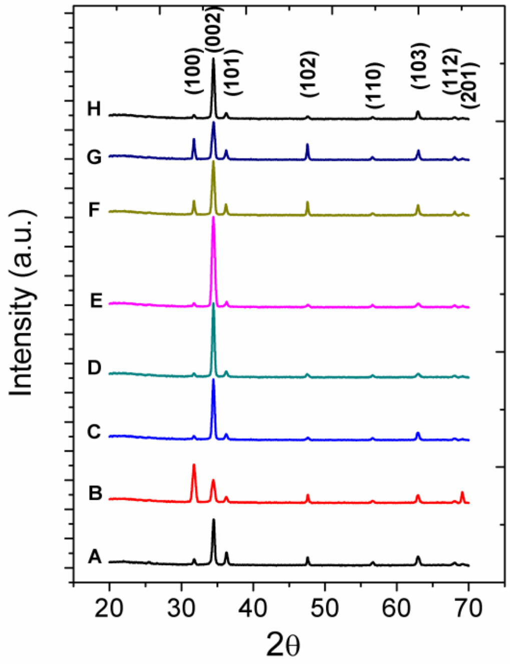

Figure 7.4 XRD patterns of (A) ZnO seed layer, (B) ZnO NRs grown without seed layer (preheating 6 hr). ZnO NRs grown using seed layer (C) without pre-heating and with pre-heating of the solution for (D) 2 hr; (E) 6 hr; (F) 8 hr; (G) 10 hr; (H) 6 hr pre-heating with 6 hr growth time

Fig.7.5 shows the Raman spectra of ZnO NRs grown for three different pre-heating time of 2h, 6h, and 10h respectively. A strong characteristic peak at 437 cm^{-1} for the E_2^{high} mode confirms that all the NRs were having c-axis oriented wurtzite structure.

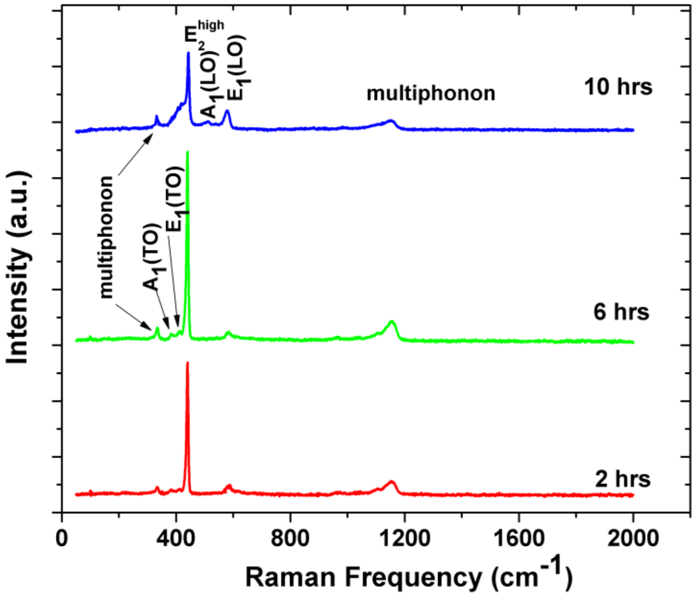

Pre-heating time (hrs)	FWHM of E_2^{high} mode (cm^{-1})	Peak Intensity of E_2^{high} mode (a.u.)
2	6.87	13462
6	6.53	18627
10	8.61	8694

Figure 7.5 Raman spectra of ZnO NRs grown using seed layer for a growth time of 12 hr with varying pre-heating times for the precursor solution

Other characteristic peaks of ZnO hexagonal structure has also been observed, but with very small intensity, viz. E_1(LO) mode at 576 cm^{-1}, A_1(TO) mode at 387 cm^{-1} and E_1(TO) mode at 412 cm^{-1}. The intensity of E_2^{high} mode is maximum for 6 hr pre-heating time. For the NRs grown with 10 hr pre-heating time, this intensity is decreased and FWHM is increased. It indicates the degradation of lattice structure as well as growth in random directions of ZnO NRs grown in solutions with large pre-heating time as was also confirmed by the XRD and SEM results. In addition, multi phonon modes were also observed at 333 cm^{-1} and 1147 cm^{-1}.

7.4 Photoluminescence Spectra of ZnO NRs

Fig.7.6 shows PL spectra from ZnO NR samples and ZnO thin film seed layer with excitation of 300 nm wavelength of Xe lamp source. PL emission from ZnO seed layer is a broad band UV-emission centered around 374 nm along with defect related green band emission situated around 540 nm. PL spectra of ZnO NRs with different growth time of 6 hr, 8 hr and 12 hr without pre-heating the precursor solution is shown in Fig. 7.6.

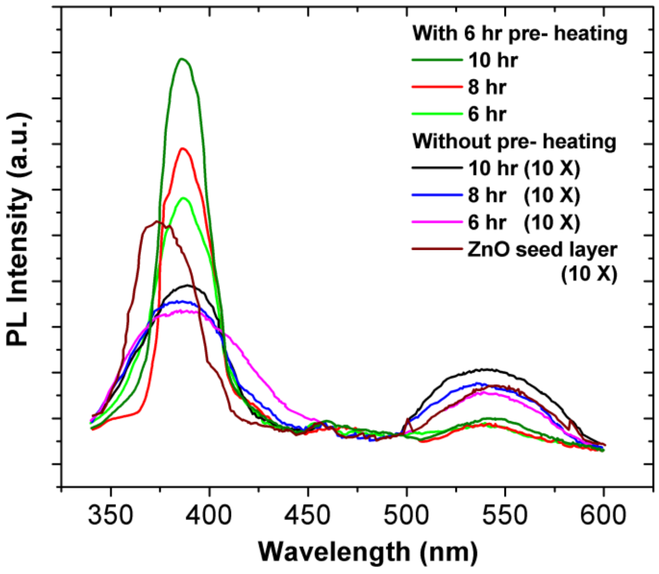

Figure 7.6 PL spectra of ZnO NRs with different growth times ranging from 6 hr to 12 hr (with and without pre-heating) and ZnO seed layer

In the same figure, PL spectra of ZnO NRs grown with pre-heating the solution for 6 hr have been shown for different growth time. PL emission from ZnO NR samples showed enhanced UV-emission centered around 386 nm. This is attributed to the free exciton recombination. There is a marginal effect of the growth time on to the UV emission as well as green emission from the ZnO NRs grown without pre-heating of the pre-cursor solution. Defect related, relatively weak green band emission centered on 540 nm was observed to be suppressed in NRs grown after pre-heating. This indicates high quality of ZnO NRs. The UV emission from ZnO NR samples was slightly red shifted with respect to that from ZnO seed layer, possibly due to high surface to volume ratio for ZnO nanorods [243]. The UV-PL intensity drastically increased for the NRs grown after pre-heating the solution. In case of pre-heating, UV-PL intensity found to be increased considerably with growth time of NRs. This behavior can be attributed to increase in NRs density and aspect ratio with increasing growth time and formation of highly c-axis oriented ZnO NRs due to pre-heating of precursor solution as is also obvious from the SEM images of NRs [Fig 7.2].

7.5 Second Harmonic Generation in ZnO nanorods

ZnO possesses large second order nonlinearity due to its non-centrosymmetric nature [231, 244-247]. SHG in ZnO nanowires via femtosecond IR laser excitation have been reported recently [247]. Due to its large two-photon absorption (TPA) coefficient [230], the TPA process in ZnO can be strong enough to act as a possible route to induce SHG at 532 nm upon 1064 nm nanosecond IR laser excitation.

SHG in ZnO nanorods was studied using setup described in Chap.2, Sec 2.5. The fundamental (1064 nm) wavelength from a Q-switched Nd:YAG laser having 8-ns pulse width was used for excitation. The angle of incident beam was adjusted around 30^{o} for maximum SHG output for all the samples. The laser irradiance was kept fixed at 28 MW/cm^2 for all the measurements. Bright green emission from the ZnO NR samples was observed visually upon excitation. SHG emission in direction perpendicular to the sample surface was collected using a lens and imaged on to monochromator entrance slit for recording.

SHG measurements were performed for four samples, ZnO NRs grown for 12 hr time with no-preheating [Fig.7.2 (a)], ZnO NRs grown for 12 hr time with 2 hr pre-heating [Fig.7.2 (b)], ZnO NRs grown for 12 hr time with 6 hr pre-heating [Fig.7.2 (c) and (d)], and ZnO NRs grown for 12 hr time with 6 hr pre-heating then annealed in O_2 ambient at 600^o C for 4 hrs. The SHG and green band emission from ZnO NRs samples mentioned above is shown in Figure 7.7.

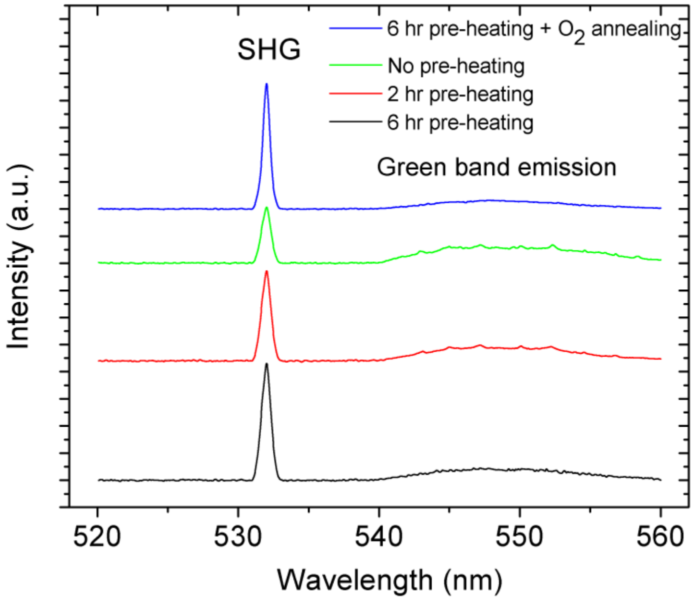

Figure 7.7 SHG and green band emission from ZnO NRs grown in different conditions

The SHG line intensity was increased for ZnO NR samples grown with pre-heating in comparison to NRs grown without pre-heating. Also the SHG line intensity was increased for ZnO NRs grown with longer pre-heating time. SHG efficiency in wurtzite nanostructures depend upon two important parameters, lattice orientation and aspect ratio of the nanostructures [244]. Hence the increase in SHG can be attributed to enhanced c-axis orientation and larger aspect ratio of ZnO NRs grown with 6 hr pre-heating in comparison to 2hr pre-heating (Fig.7.2 and 7.4).

The ZnO NRs grown without pre-heating were randomly oriented [Fig. 7.2 (a)] which can be a reason for low SHG intensity. Effect of crystalline structure and orientation on the SHG efficiency of ZnO NRs can further be observed in case of O_2 annealed ZnO NR sample. The SHG intensity for this sample was increased in comparison to unannealed one whereas green band emission intensity was suppressed. This can be related to removal of oxygen vacancy defect states in ZnO NRs and enhancement in their crystalline quality upon annealing in O_2 ambient.

7.6 Nonlinear absorption and refraction in ZnO nanorods

The non-linear absorption coefficient and non-linear refractive index of ZnO NRs grown in different conditions were measured by open and close z-scan technique, respectively. Z-scan measurements were performed for four ZnO NR samples. Three samples were with 12 hr growth time and different pre-heating time of 2 hr, 6 hr, 10 hr, and one with 12 hr growth time but no pre-heating. The open and close z-scan curves for all these four samples are shown in Fig.7.8 (a), (b), (c) and (d), respectively. The values of non-linear absorption co-efficient β, non-linear refractive index n_2 and non-linear susceptibility $\chi^{(3)}$ obtained from the fitting of z-scan curves (Chapter 2, Sec. 2.8) are listed in Table 7.1. The maximum non-linear absorption coefficient (β = 329.57 cm/GW) was obtained for 6hr pre-heated ZnO NRs, followed by 10hr and 2hr pre-heated samples. While the lowest value of β (231.09 cm/GW) was obtained for ZnO NRs grown without pre-heating. Non-linear refractive index n_2 of ZnO NRs was also found to be dependent upon pre-heating duration. While the maximum value of n_2 was estimated around 22 × 10^{-13} cm^2/W for ZnO NRs grown with 6 hr preheating, it decreased to 16 × 10^{-13} cm^2/W for NRs grown without preheating. Third-order non-linear susceptibility $\chi^{(3)}$ followed a similar trend with 2.65 × 10^{-10} esu for ZnO NRs grown with 6 hr preheating and 1.90 × 10^{-10} esu for NRs grown without preheating

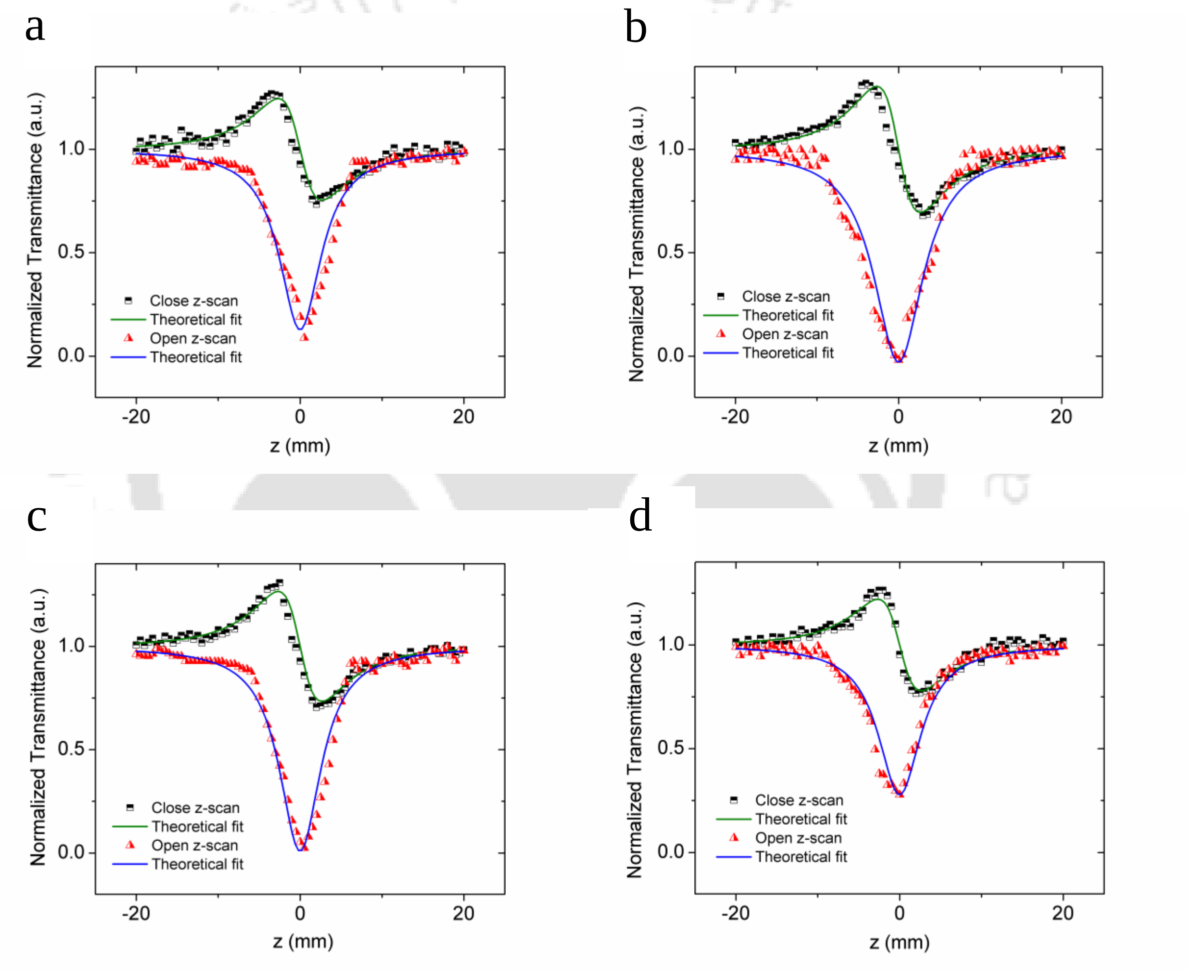

Figure 7.8 Open and close z-scan curves for ZnO NRs with 12 hr growth time and pre-heating time (a) 2 hr; (b) 6 hr; (c) 10 hr; (d) without pre-heating. (Symbols and solid line represent experimental data and theoretical fit, respectively)

The dependence of non-linear optical coefficients on the preheating duration can be attributed to enhancement in vertical alignment and aspect ratio of ZnO NRs with preheating as discussed in sec 7.2. These results further confirm that optimum pre-heating time to obtain the vertically aligned ZnO NRs with excellent non-linear optical properties on the PLD seed layer of ZnO is 6 hrs.

ZnO Nanorod growth conditions	**Nonlinear absorption β (cm/GW)**	**Nonlinear refractive index n_2 (10^{-13} cm^2/W)**	**Nonlinear susceptibility $\chi^{(3)}$ (10^{-10} esu)**
No preheating/12 hr growth time	231.09	16.0	1.90
2 hr preheating/12 hr growth time	279.30	17.8	2.17
10 hr preheating/12 hr growth time	315.20	19.3	2.38
6 hr preheating/12 hr growth time	329.57	22.1	2.65

Table 7.1 Values of various nonlinear optical coefficients obtained using z-scan for ZnO NRs grown under different conditions

7.7 Multi Photon Absorption Induced Lasing Action in ZnO Nanorods

In most of the photo pumped lasing action in ZnO, single photon absorption mechanism has been utilized by pumping with deep UV-lasers. Multi-photon absorption (MPA) process [248, 249] by pumping with IR lasers for frequency conversion is another potential solution for the generation of UV laser in ZnO. Multi photon absorption in ZnO utilizes non-linear interaction between applied intense optical field and ZnO nanostructures. This leads to simultaneous absorption of two or more photons of sub band gap energy. These virtual states interband transition produces electron-hole pairs in the excited states and subsequently, the band edge emission from ZnO nanostructures takes place via radiative recombination. MPA has been demonstrated as an efficient excitation process to pump carriers in ZnO thin films with green nano-second lasers as well as near IR femtosecond lasers [88, 249-251].

MPA induced lasing action in ZnO nanorods can take place via three mechanisms; two photon absorption (TPA) using second harmonic at 532 nm from ZnO (generated via two photon direct absorption in ZnO, Sec 6.5), direct three photon absorption (3PA) of 1064 nm and sum frequency generation utilizing both 532 and 1064 nm. Out of these, possibility of sum frequency generation along the c-axis of ZnO nanorods in the present setup can be ruled out because phase matching condition will not be satisfied. It may be possible that both TPA and 3PA processes are taking part simultaneously in inducing lasing action in ZnO nanorods [252, 253].

MPA induced lasing action in ZnO NRs have been recorded by exciting with 1064 nm wavelength of 8 ns Q-switched Nd:YAG laser. Initially at low excitation intensities, broad UV-PL emission with excitonic features, situated around 386 nm has been observed (Fig.7.9). In addition to MPA induced UV emission from ZnO NRs, second harmonic generation at 532 nm and green band emission centered at 540 nm has been also observed. With an increase of the pump intensity to 28 MW/cm^2, broad PL spectra switches over to an intense and relatively sharp peak centered around ~ 392 nm, indicating a transition from spontaneous emission to amplified spontaneous emission (ASE). Variation of laser intensity at 392 nm, SHG at 532 nm and green band emission at 540 nm with respect to pump intensity is plotted in Fig. 7.10. Beyond lasing threshold (marked by I_{th} in Fig.7.10), intensity of ASE peak increases almost exponentially with pump as shown in Fig.7.10, where as below threshold UV output intensity varies linearly with pump intensity.

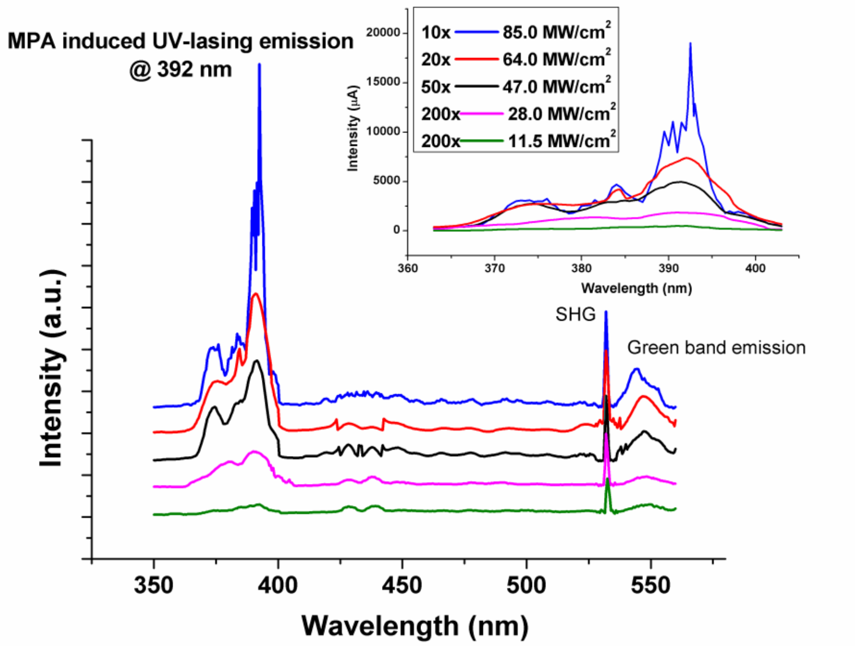

Figure 7.9 MPA induced PL spectra with second harmonic generation from ZnO NRs excited by 1064 nm Nd:YAG laser with 8 ns pulse width. (Inset: expanded view of MPA induced UV-PL emission from ZnO NRs)

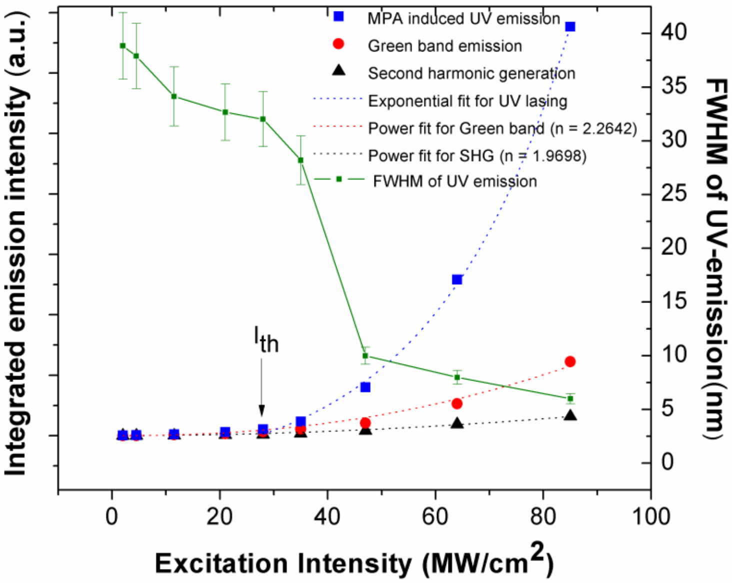

Figure 7.10 Variation of emission intensity of MPA induced UV emission at 392 nm, green band emissions at 540 nm, SHG emission at 532 nm and FWHM of UV emission at 392 nm with excitation intensity.

Super linear as well as exponential growth in the output lasing intensity with UV pump was documented in earlier reports on ZnO based lasers [95, 96, 254-256]. Further the growth of the laser radiation (above threshold) for the pulsed system is exponential. Defect related green band emission peak increases linearly with pump intensity while SHG signal intensity at 532 nm showed quadratic dependence on pump intensity. The drastic decrease in FWHM of UV emission at 392 nm as a function of pump intensity as shown in Fig.7.10, further confirms the lasing action in ZnO NRs. At very high pump intensities, nearly equispaced multiple peaks with very narrow line width (~ 0.5-0.8 nm) were observed in the ASE spectra, as shown in the inset of Fig.7.9. This multiple peak structure at high excitation intensities corresponds to longitudinal lasing modes arising because of micro cavity formation in NR arrays with lateral facets acting as weak reflectors [257], as shown schematically in Fig.7.11.

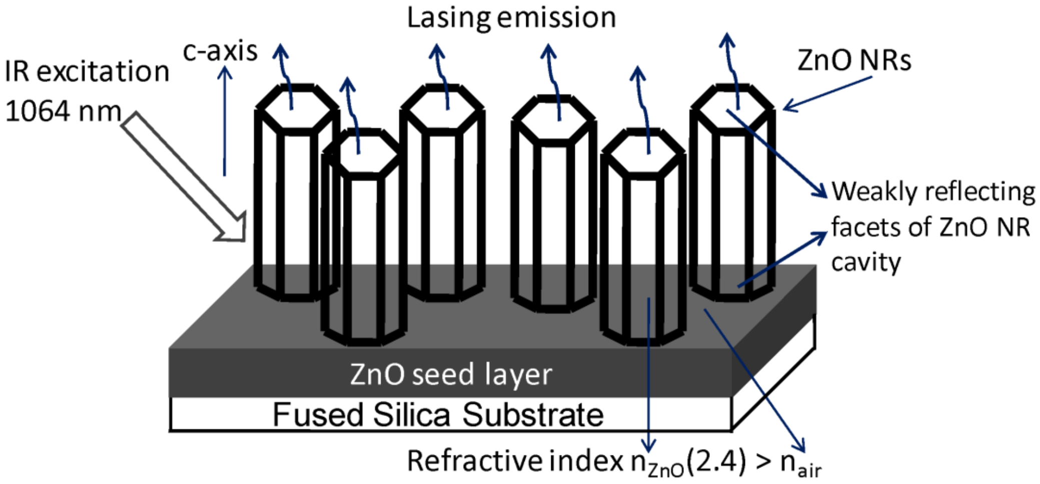

Figure 7.11 Schematic of ZnO NR cavity formed to sustain lasing emission along the c-axis of NRs.

ZnO nanarod structures not only support longitudinal modes (as in the case of classical FP cavity) but also support transverse modes due to strong optical confinement. These transverse modes travel through the ZnO NR waveguide via total internal reflection taking place at NR boundary walls. The NR's behaves as a wave guide as the refractive index of ZnO (~2.4) is higher than that of air (1.0). The lasing modes propagate in a manner similar to that of a wave guide and hence low reflectivity at the lateral facets is sufficient to provide the optical feedback to support the lasing action. The observed mode spacing (~ 1 nm) between multiple longitudinal modes indicates the presence of coherent scattering of light in the dense ZnO nano rods. The optical amplification in ZnO nanostructures is generally considered to arise from the exciton-exciton scattering [258]. But, in the present case, the red shift of lasing peak at 392 nm from the position of free exciton emission peak at 386 nm is much smaller than that of expected from exciton-exciton scattering (83 meV @ 300K) so it can not be attributed to exciton-exciton scattering . This shift and ASE may be due to exciton-carrier interaction and /or exciton–phonon interaction. At extremely high intensity of pump, near to damage threshold, recombination of electron hole plasma (EHP) may also contribute towards the gain of ASE [259].

7.8 Conclusion

Well aligned ZnO nanorod arrays with a diameter of ~ 100 nm and a length of up to 3-4 μm have been synthesized using a preheating hydrothermal method on to PLD ZnO seed layer. The use of a PLD-ZnO seed layer and the preheating process helped to produce highly oriented nanorod arrays with a relatively high aspect ratio (~30) by decreasing the nucleation energy barrier and $[Zn^{2+}]/[OH^{-}]$ ratio in the precursor solution. Structural and morphological characterizations revealed that these ZnO NRs possess a wurtzite structure with *c*-axis growth orientation. The vertical alignment and c-axis orientation of NRs found to be dependent upon preheating duration. PL measurements at room temperature showed that the ZnO NRs grown using preheated solution showed large UV emission and comparatively small defect related green band emission.

The three fold increase in SHG signal was observed in ZnO NRs compared to that of pulsed laser deposited ZnO seed layer. Non-linear absorption coefficient was found to increase from 194 cm/GW to 329 cm/GW for ZnO NR samples in comparison to PLD thin film of ZnO. The non-linear refractive index of ZnO NRs was found to be increased approximately three times compared to that of ZnO thin film. It was observed that annealing of ZnO NRs in O_2 ambient can further enhance the SHG line intensity and decrease the defect related green band emission. Upon excitation with nanosecond pulses of Nd:YAG laser (1064 nm), MPA induced UV laser action at 392 nm was realized in hydrothermally grown ZnO NR arrays at room temperature.

Chapter 8

Conclusion

The fabrication and characterization of AlN, TiO_2, $Zn_{1-x}Mg_xO$ ($0 \le x \le 0.7$) semiconductor thin films via laser ablation is reported in this thesis. The effect of substrate annealing, target-substrate distance, substrate temperature and background gas pressure on the properties of thin films grown using PLD was studied. The frequency up-conversion was observed in $Zn_{1-x}Mg_xO$ thin films and ZnO nanorods confirming non-linear optical (NLO) properties of these systems. The possibility of UV laser action in ZnO NRs was also explored.

AlN thin films with c-axis orientation were deposited at room temperature via PLD technique using pure Al target. The optimum value of N_2 pressure, target substrate distance and laser irradiance for the deposition of (002) oriented AlN thin films was found to be 10^{-2} mbar, 3 cm and 8 x 10^{11} W/cm^2, respectively. The observation of AlN band in laser produced plasma of Al in nitrogen background confirmed the reactive recombination between Al and N ions to form molecular AlN. From the parametric intensity variation of various ionic lines of LIP spectra, it was concluded that Al II and N II transitions may be responsible for growth of AlN thin films with (002) preferred orientation and Al III and N III transitions for AlN thin films with (101) preferred orientation.

TiO_2 thin films have been deposited via PLD technique on glass substrates in O_2 and Ar ambient using a sintered TiO_2 target. TiO_2 films deposited in Ar ambient were predominantly having amorphous anatase phase which upon annealing at 500^o C changed to crystalline anatase phase. Enhanced crystalline structure and change in phase from anatase to rutile with annealing temperature was observed for TiO_2 thin films deposited in O_2 ambient. TiO_2 nanorods were obtained after post-annealing at 650^o C of the films deposited at 1 mbar O_2 pressure. The PL spectra of TiO_2 films showed red shift with increase in annealing temperature with peak position at 3.03 eV for as-deposited film to 3.26 eV for 650^{o}C annealed film. As–deposited TiO_2 thin film showed 10% reflectance in UV-VIS range which may be suitable for anti-reflection coating applications. The contact angle measurements confirmed the higher hydrophobicity of TiO_2 thin films with the increase in annealing temperature.

The dynamics of laser induced ZnO plasma was studied to find correlation between properties of ZnO thin film grown via PLD and laser induced ZnO plasma parameters. An optimum value of O_2 pressure in the range of 10^{-3} mbar to 10^{-1} mbar and target substrate distance more than 20 mm was observed to be suitable for the fabrication of smooth cluster free stochiometric ZnO films.

Bandgap engineering of ZnO was achieved by depositing high quality (0002) - oriented crystalline $Zn_{1-x}Mg_xO$ films epitaxially on (0001) sapphire substrates using PLD technique. XRD and Raman studies confirmed wurtzite structure of $Zn_{1-x}Mg_xO$ alloy films up to 34 % Mg concentration and cubic phase for 60 % and above of Mg concentration. Room temperature excitonic emission was observed from the c-axis oriented $Zn_{1-x}Mg_xO$ $(0.0 \le x \le 0.34)$ thin films. Effect of Mg concentration and substrate temperature on the exciton band gap, exciton binding energy, and broadening parameter was studied from the absorption spectra. The optical band gap of $Zn_{1-x}Mg_xO$ thin film was successfully tuned from 3.3 to 4.6 eV by adjusting the Mg content (x = 0.0 to x= 0.60) and corresponding PL was observed to be shifted from 386 nm (x = 0.00) to 292 nm (x = 0.34). The annealing of the sapphire substrate prior to the deposition enhanced columnar growth and crystallinity of the $Zn_{1-x}Mg_xO$ films. The enhancement in UV-PL signal was observed for films deposited on substrates annealed at higher temperatures.

The second and third harmonic generation, at 532nm and 355nm respectively, from $Zn_{1-x}Mg_xO$ ($0 \leq x \leq 0.1$) film upon excitation with nanosecond pulses of 1064 nm radiation confirmed the non linear optical properties of these PLD films. SHG intensity was observed to be rapidly decreasing with increased Mg content. No harmonic generation was observed for the films with more than 10 % of Mg content. THG emission was observed only in pure ZnO thin films (x=0). The non-linear absorption coefficient and non-linear refractive index of $Zn_{1-x}Mg_xO$ thin film was decreased from 180 cm/GW to 81 cm/GW and 11.2×10^{-10} cm^2/W to 1.75×10^{-10} cm^2/W, respectively, with increasing the Mg content from 1 to 10%. Both these effects were attributed to ZnO lattice degradation upon Mg doping.

The well aligned ZnO nanorods were grown on PLD seed layer of ZnO using a hydrothermal method to explore the possibilities of lasing action in UV region via multiphoton absorption (MPA). The vertical alignment and c-axis orientation of NRs found to be dependent on hydrothermal growth parameters. ZnO NRs showed enhanced UV emission and comparatively small defect related green band emission compared to that of ZnO seed layer. The three fold increase in SHG signal was also observed in ZnO NRs. Non-linear absorption coefficient was found to increase from 194 cm/GW for seed layer to 329 cm/GW for ZnO NR. Non-linear refractive index of ZnO NRs was increased two fold compared to that of its seed layer. Multiphoton absorption (MPA) induced UV lasing action around 392nm was observed upon excitation with nanosecond pulses of Nd:YAG laser (1064 nm), in the ZnO NRs.

Future Scope

The c-axis oriented $Zn_{1-x}Mg_xO$ ($0<x<0.34$) thin films developed in the present work can be used for fabrication of tunable UV broadband light emitting diodes (LEDs) on the sapphire (0001) or ZnO substrate with appropriate doping for n- and p- type layer for the formation of p-n junction. MPA induced UV lasing from ZnO NRs can solve the problems associated with deep UV excitation for the practical application of such NRs in the areas of medical imaging and nano drug delivery.

Another material system having potential for bandgap tunability to cover near IR to deep UV spectrum consists of composites of AlN (6.2 eV), GaN (3.4 eV) and InN (0.7 eV). Composite thin films of $Al_{1-x}In_xN$ and $Al_{1-x}Ga_xN$ can be fabricated using the deposition process outlined in the present thesis. In the present work, AlN thin films via PLD by using pure aluminum has been demonstrated successfully in (002) oriented wurtzite phase. At present, the major limitation to extend the AlN to AlInN or to AlGaN is the non availability of low cost suitable target for PLD for this series of nitrides. Due to very high cost of pure InN and GaN powders, difficulty in handling to prepare the the oxygen free target for PLD, low thermal decomposition temperature of InN, and Ga cluster formation upon laser ablation are the major obstacles to be resolved in order to use PLD for the fabrication of $Al_{1-x}In_xN$ and $Al_{1-x}Ga_xN$ thin films.

Bibliography

1 Ashfold, M.N.R., Claeyssens, F., Fuge, G.M., and Henley, S.J., (2004). *Pulsed laser ablation and deposition of thin films*. Chem. Soc. Rev. **33**, 23

2 Vispute, R.,D., et al (1999). *Pulsed laser deposition and processing of wide band gap semiconductors and related materials.* J. Elec. Res. **28**, 275

3 Ohtomo, A., and Tsukazaki, A.,(*2005). Pulsed laser deposition of thin films and superlattices based on ZnO.* Semicond. Sci. Technol. **20**, S1

4 Lackner, J.M., (2005). *Industrially-styled room-temperature pulsed laser deposition of ZnO:Al films*. Thin Solid Films **494**, 302

5 Zheng, J. P., and Kwok, H. S., (1993). *Preparation of indium tin oxide films at room temperature by pulsed laser deposition.* Thin Solid Films **232**, 99

6 Suresh, A., Wellenius, P., Dhawan, A., and Muth, J., (2007). *Room temperature pulsed laser deposited indium gallium zinc oxide channel based transparent thin film transistors*. Appl. Phys. Lett. **90**, 123512

7 Thöny, S.S., Youden, K. E., Harris, J. S., and Hesselink, L., (1994). *Growth of epitaxial strontium barium niobate thin films by pulsed laser deposition*. Appl. Phys. Lett. **65**, 2018 (1994)

8 Chrisey, D. B., and Hubler, G.K., (Eds.) (1994). *Pulsed Laser Deposition of Thin Films*. Wiley-Interscience, New York

9 Smith, H.M., and Turner, A.F., (1965). *Vacuum deposited thin films using a ruby laser.* Appl. Opt. **4**, 147

10 Narayan, J., Biunno, N., Singh, R., Holland, O. W., and Auciello, O., (1987). *Formation of thin superconducting films by the laser processing method.* Appl. Phys. Lett. **51**, 1845

11 Cheung, J., and Horwitz, J., (1992). *Pulsed laser deposition history and laser-target interactions*. MRS Bulletin. **17**, 30

12 Gross, R., Chaudhari, P., Kawasaki, M., Ketchen, M. B., and Gupta, A., (1990). *Low noise* $YBa_2Cu_3O_{7-\delta}$ *grain boundary junction dc SQUIDs*. Appl. Phys. Lett. **57**, 727

13 Kwon, C., et al, (1993). *High critical current densities in ultrathin $YBa_2Cu_3O_{7-\delta}$ films sandwiched between $(Pr_xY_{1-x})Ba_2Cu_3O_{7-\delta}$ layers.* Appl. Phys. Lett. **62**, 1289

14 Liu, M., et al (2010). *Magnetic and transport properties of epitaxial $(LaBa)Co_2O_{5.5+\delta}$ thin films on (001) $SrTiO_3$*. Appl. Phys. Lett. **96**, 132106

15 Hou, Y., Huang, Z., Gao, Y., Ge, Y., Wu, J., and Chu, J., (2008). *Characterization of $Mn_{1.56}Co_{0.96}Ni_{0.48}O_4$ films for infrared detection*. Appl. Phys. Lett. **92**, 202115

16 Wilmott, P. R., Manoravi, P., and Holiday, K., (2000). *Production and characterization of Nd,Cr:GSGG thin films on Si(001) grown by pulsed laser ablation*. Appl. Phys.A **70**, 425

17 Singh, M. P., Truong, K. D., Jandl, S., and Fournier, P., (2009). *Stabilization and functional properties of $La_3NiAlMnO_9$ and $La_3CoAlMnO_9$ magnetoelectric triple perovskites*. Appl. Phys. Lett. **94**, 171908

18 Wu, C. T., et al, (2010). *Heterojunction of $Fe(Se_{1-x}Te_x)$ superconductor on Nb-doped $SrTiO_3$*. Appl. Phys. Lett. **96**, 122506

19 Bakalova, S., et al (2007). *Influence of in-situ nitrogen pressure on crystallization of pulsed laser deposited laser beams.* Appl.Surf.Sci. **253**, 8215

20 Kim, H. S., Pearton, S. J., Norton, D. P., and Ren’ F., (2007). *Behavior of rapid thermal annealed ZnO:P films grown by pulsed laser deposition*. J. Appl. Phys. **102**, 104904

21 Di Trolio, A., Bauer, E. M., Scavia, G., and Veroli, C., (2009). *Blueshift of optical band gap in* **c***-axis oriented and conducting Al-doped ZnO thin films*. J. Appl. Phys. **105**, 113109

22 Shim, E.S., Kang, H.S., Pang, S.S., Kang, J.S., Yun, I., Lee, S.Y., (2003). *Annealing effect on the structural and optical properties of ZnO thin film on InP.* Mat. Sci and Engg. B **102**, 366

23 Capitelli, M., Casavola, A., Colonna, G., De Giacomo, A., (2004). *Laser-induced plasma expansion: theoretical and experimental aspects*. Spectrochimica Acta Part B, **59**, 271

24 Mulser, P. and Bauer, D., (2010). *High power laser matter interaction.* Springer tracts in modern physics **238**, Springer-Verlag, Berlin Heidelberg

25 Amoruso, S., Toftmann. B., and Schou, J., (2004). *Thermalization of a UV laser ablation plume in a background gas: From a directed to diffusion like flow*. Phys. Rev. E **69**, 056403

26 Chen, X. Y., Xiong, S. B., Sha, Z. S., and Liu, Z. G., (1997). *The interaction of ambient background gas with a plume formed in pulsed laser deposition*. Appl. Surf. Sci. **115**, 279

27 Venkateshan, T., and Green, S. M., (1996). *Pulsed laser deposition: thin films in a flash.* The Industrial Physicist **2**, 22

28 Clark, J. H., and Weston, R. G., (1996). *An inexpensive mutli-target carousel for PLD systems.* Meas. Sci. Technol. **7**, 823

29 Mao, S.S., Mao, X., Greif, R., and Russo, R. E., (2000). *Initiation of early stage plasma during picoseconds laser ablation of solids.* Appl. Phys. Lett. **77**, 2464

30 Sokolowski-Tinten, K., *et al* (1998). *Transient states of matter during short pulse laser ablation.* Phys. Rev. Lett. **81**, 224

31 Lu, Y. F., Hong, M. H., and Low, T. S., (1999). *Laser plasma interaction at an early stage of laser ablation.* J. Appl. Phys. **85**, 2899

32 Singh, R. K., and Narayan, J., (1990). *Pulsed-laser evaporation technique for deposition of thin films: Physics and theoretical model*. Phys. Rev. B **41**, 8843

33 Chinchkov, B. N., Momma, C., Nolte, S., Von-Alvensleben, F., and Tunnermann, A., (1996). *Femtosecond, picoseconds and nanosecond laser ablation of solids.* Appl. Phys. A, **63**, 109

34 Russo, R. E., (1995). *Laser ablation.* Appl. Spectroscopy, **49,** 14A

35 Willmott, P.R., and Huber, J.R., (2000). *Pulsed Laser Vaporization and Deposition*. Rev. Mod. Phys. **72**, 315

36 Gibbon, P., (2005). *Short pulse laser interactions with matter: an introduction*. Imperial College Press, London

37 Allmen, M. V., and Blatte, A., (1995). *Laser-beam interactions with materials: physical principles and applications.* (Second Ed.) Springer Verlag, Berlin

38 Gamaly, E. G., Rode, A. V., and Luther-Davies, B., (1999). *Laser ablation of carbon at the threshold of plasma formation.* Appl. Phys. A **69**, S121

39 Rand, S., (1964). *Inverse Bremsstrahlung with High-Intensity Radiation Fields*. Phys. Rev. **136**, B231

40 Dreyfus, R.W., (1991). *Cu^0, Cu^+, and Cu_2 from excimer-ablated copper*. J.Appl. Phys. **69**, 1721

41 Wiedeman, L., and Helvajian, H., (1991). *Laser photodecomposition of sintered $YBa_2Cu_3O_{6+x}$: Ejected species population distributions and initial kinetic energies for the laser ablation wavelengths 351, 248, and 193 nm*. J.Appl. Phys. **70**, 4513

42 Demtroder, W., and Jantz, W., (1970). *Investigation of laser-produced plasmas from metal-surfaces*. Plasma Physics **12**, 691

43 Venables, J.A., Spiller, G.D., and Hanbuecken, M., (1984). *Nucleation and growth of thin films*. Rep. Prog. Phys. **47**, 399

44 Metev, S., and Meteva, K., (1989). *Nucleation and growth of laser plasma deposited thin films.* Appl. Surf. Sci. **43**, 402

45 Metev, S., (1994). *Nucleation and growth of pulsed laser deposited thin films* in "*Pulsed Laser Deposition of Thin Films*", (Eds: D.B. Chrisey and G.K. Hubler). Wiley-Interscience, New York, Chapter 9, pp. 255.

46 Adrain, R.S., Watson, J., (1984). *Laser microspectral analysis: a review of principles and applications*. J. Phys. D: Appl. Phys. **17**, 1915

47 Harilal, S.S., Bindhu, C.V., Issac, R. C., Nampoori, V. P. N., and Vallabhan, C. P. G., (1997). *Electron density and temperature measurements in a laser produced carbon plasma*. J. Appl. Phys. **82**, 2140

48 Sattman, R., Sturm, V., and Noll, R., (1995). *Laser-induced breakdown spectroscopy of steel samples using multiple Q-switch laser pulses.* J. Phys. D: Appl. Phys. **28**, 2181

49 Miziolek, A. W., Palleschi, V., Schechter, I., (2006). *Laser-induced breakdown spectroscopy (LIBS): fundamentals and applications*. Cambridge University Press, London

50 Haisch, C., Liermann, J., Panne, U., and Niessner, R., (1997). *Characterization of colloidal particles by laser-induced plasma spectroscopy.* Analytica Chimica Acta **346**, 23

51 Sun, Q., Tran, M., Smith, B. W., and Winefordner, J. D., (2000). *Determination of Mn and Si in iron ore by laser-induced plasma spectroscopy*. Analytica Chimica Acta **413**, 187

52 Neuhauser, R. E., Panne, U., and Niessner, U., (1999). *Laser-induced plasma spectroscopy: a versatile tool for monitoring heavy metal aerosols.* Analytica Chimica Acta **392**, 47

53 Griem, H. R., Kolb, A. C., and Shen, K. Y., (1959). *Stark Broadening of Hydrogen Lines in a Plasma*. Phys. Rev. **116**, 4

54 Griem, H.R., (1974). *Spectral Line Broadening by Plasmas*. Academic Press, Newyork

55 Griem, H.R., (1964). *Plasma Spectroscopy*. McGraw-Hill, Newyork

56 Bekefi, G., (Ed.), (1976). *Principles of Laser Plasmas*. John Wiley and Sons

57 Lochte-Holtgreven, W., (Ed.), (1968). *Plasma Diagnostics*. North Holland Publishing Company, Newyork

58 Griem, H. R., (1963). *Validity of Local Thermal Equilibrium in Plasma Spectroscopy*. Phys. Rev. **131**, 1170

59 Cowan, R. D., and Dieke, G. H., (1948). *Self-Absorption of Spectrum Lines*. Rev. Mod. Phys. **20**, 418

60 McWhirter, R.W.P., (1965). *Spectral intensities*, in: R.H. Huddlestone, S.L. Leonard (Eds.) “Plasma Diagnostic Techniques”, Academic Press, 1965, Chapter 5.

61 Aragón, C., and Aguilera, J.A., (2008). *Characterization of laser induced plasmas by optical emission spectroscopy: A review of experiments and methods*. Spectrochimica Acta Part B **63**, 893 (2008)

62 Dicke, R. H., (1953). *The Effect of Collisions upon the Doppler Width of Spectral Lines*. Phys. Rev**. 89**, 472

63 Ali, A. W., and Griem, H. R., (1965). *Theory of Resonance Broadening of Spectral Lines by Atom-Atom Impacts*. Phys. Rev. **140**, A1044

64 Foley, H. M., (1946). *The Pressure Broadening of Spectral Lines*. Phys. Rev. **69**, 616

65 Gornushkin, I. B., King, L. A., Smith, B. W., Omenetto, N., and Winefordner, J. D., (1999). *Line broadening mechanisms in the low pressure laser-induced plasma* Spectrochimica Acta Part B **54**, 1207

66 Col´on, C., Alonso-Medina, A., and Herr´an-Mart´ınez, C., (1999). *Spectroscopic study of laser-produced lead plasma: experimental atomic transition probabilities for Pb III lines.* J. Phys. B: At. Mol. Opt. Phys. **32**, 3887.

67 Colao, F., Lazic, V., Fantoni, R., Pershin, S., (2002). *A comparison of single and double pulse laser-induced breakdown spectroscopy of aluminum samples.* Spectrochim. Acta Part B **57**, 1167

68 Cho, A.Y., (1991). *Advances in Molecular Beam Epitaxy*. J. Crystal Growth, **111**,1

69 Depla, D., and Mahieu, S., (Eds.) (2005). *Reactive Sputter Deposition (Series: Springer Series in Materials Science, Vol. 109)*. Springer, Berlin

70 Neifeld, R. A., *et al* (1988). *Systematics of thin filmsformed by excimer laser ablation: Results on* $SmBa_2Cu_3O_7$. Appl. Phys. Lett. **53**, 703

71 Takahashi, K., Yoshikawa, A., and Sandhu, A.,(Eds.), (2007). *Wide Bandgap Semiconductors: Fundamental Properties and Modern Photonic and Electronic Devices*. Springer-Verlag, Heidelberg, Berlin

72 Ren, F., and Jolper, J.C., (Eds.), (2003). *Wide Energy Band Gap Electronic Devices*. World Scientific, Singapore

73 Pearton, S., J., (Ed.), (2000). *Processing of Wide Band Gap Semiconductors (Materials and Processing Technology)*. Voyes Publications, Newyork

74 Jain, S.C., Willander, M., Narayan, J., and Overstraeten, R.V., (2000). *III nitrides : Growth, Charecterization, and Properties*. J. Appl. Phys. **87**, 965

75 Gao, F., Lee, S., J., Pan, J., S., Tang, L., J., Kwong, Dim-Lee, (2005). *Surface passivation using ultrathin AlNx film for Ge–metal–oxide–semiconductor devices with hafnium oxide gate dielectric*. Appl. Phys. Lett. **86**, 113501

76 Yim, W. M., Paff, R. J., (1974). *Thermal expansion of AlN, sapphire, and silicon*. J. Appl. Phys. **45**, 1456

77 Yoshida, S., (2007). *Fundamental Properties of Wide band gap semiconductors* in *"Wide Bandgap Semiconductors: Fundamental Properties and Modern Photonic and Electronic Devices"* (Eds: Kiyoshi Takahashi, Akihiko Yoshikawa and Adarsh Sandhu). Springer-Verlag, Berlin Heidelberg

78 Assouar, M. B., Elmazria, O., Kirsch, P., Alnot, P., Mortet, V., and Tiusan, C., (2007). *High-frequency surface acoustic wave devices based on AlN/diamond layered structure realized using e-beam lithography*. J. Appl. Phys. **101**, 114507

79 Karabalin, R.B., *et al*, (2009). *Piezoelectric nanoelectromechanical resonators based on aluminum nitride thin films*. Appl.Phys.Lett. **95**, 103111

80 Benjamin, M. C., Wang, C., Davis, R. F., Nemanich, R. J., (1994). *Observation of a negative electron affinity for heteroepitaxial AlN on α(6H)-SiC(0001)*. Appl. Phys. Lett. **64**, 3288

81 Kumta, A., Rusli, and Xia, J. H., (2009). *Breakdown phenomena of Al-based high-k dielectric/SiO$_2$ stack on 4H-SiC*. Appl. Phys. Lett. **94**, 233505

82 Liu, W., Zhu, J. J., Jiang, D. S., Yang, H., and Wang, J. F., (2007). *Influence of the AlN interlayer crystal quality on the strain evolution of GaN layer grown on Si (111)*. Appl. Phys. Lett. **90**, 011914

83 Ponce, F. A., and Bour, D. P., (1997). *Nitride-based semiconductors for blue and green light-emitting devices*. Nature **386**, 351

84 Taniyasu, Y., Kasu, M., Makimoto, T., (2006). *An aluminium nitride light-emitting diode with a wavelength of 210 nanometres*. Nature **441**, 325

85 Willander, M., *et al*, (2009). *Zinc Oxide Nanorod based Photonic Devices: Recent Progress in Growth, Light emitting diodes and lasers*. Nanotechnology, **20**, 332001

86 Wright, J.S., *et al* (2010). *Nitride and Oxide semiconductor based nanostructured hydrogen gas sensors*. Semicond .Sci. Technology, **25**, 024002

87 Özgür, Ü., Alivov, Ya. I., Liu, C., Teke, A., Reshchikov, M. A. , Doğan, S. Avrutin, V., Cho, S.-J. and Morkoç, H. (2005). *A comprehensive review of ZnO materials and devices*. J.Appl.Phys. **98**, 041301

88 Chelnokov, E. V., Bityurin, N., Ozerov, I., and Marine, W., (2006). *Two-photon pumped random laser in nanocrystalline ZnO*. Appl. Phys. Lett. **89**, 171119

89 Johnson, J. C., Yan, H., Schaller, R. D., Petersen, P. B., Yang, P., and Saykally, R. J., (2002). *Near-field imaging of Nonlinear Optical Mixing in Single Zinc Oxide Nanowires*. Nano Lett. **2**, 279

90 Wraback, M., Shen, H., Liang, S., Gorla, C. R., and Lu, Y., (1999). *High contrast, ultrafast optically addressed ultraviolet light modulator based upon optical anisotropy in ZnO films grown on R-plane sapphire*. Appl. Phys. Lett. **74**, 507

91 Vivas, M.G., Shih, T., Voss, T., Mazur, E., and Mendonca, C. R., (2010). *Nonlinear spectra of ZnO: reverse saturable, two- and three-photon absorption*. Optics Express, **18**, 9628

92 Fujiwara, H., and Sasaki, K., (2006). *Observation of optical bistability in a ZnO powder random medium*. Appl. Phys. Lett. **89**, 071115

93 Bagnall, D.M., Chen, Y.F., Zhu, Z., Yao, T., Shen, M.Y., Goto, T., (1998). *High temperature excitonic stimulated emission from ZnO epitaxial layers*. Appl. Phys. Lett. **73,** 1038

94 Ryu, Y. R., *et al* (2007). *Excitonic ultraviolet lasing in ZnO based light emitting diodes*. Appl. Phys. Lett. **90**, 131115

95 Yu, S.F., Yuen, C., Lau, S.P., Park, W.I., and Yi, Gyu-Chul, (2004). *Random laser action in ZnO nanorod arrays embedded in ZnO epilayers*. Appl. Phys. Lett. **84**, 3241

96 Han, X., *et al* (2005). *Ultraviolet lasing and time-resolved photoluminescence of well aligned ZnO nanorod arrays*. Appl. Phys. Lett. **86**, 223106

97 Chu, S., Olmedo, M., Yang, Z., Kong, J., and Liu, J., (2008). *Electrically pumped ultraviolet ZnO diode lasers on Si*. Appl. Phys. Lett. **93**, 181106

98 Zalamai, V.V., Ursaki, V.V. , Klingshirn, C., Kalt, H., Emelchenko, G.A., and Redkin, A.N., (2009). *Lasing with guided modes in ZnO nanorods and nanowires*. Appl. Phys. B **97,** 817

99 Kang, J. H., Park, Y. R., Kim, K. J., (2000). *Spectroscopic ellipsometry study of* $Zn_{1-x}Mg_xO$ *thin films deposited on* Al_2O_3 *(0001).* Solid State Commun. **115**,127

100 Makino, T., *et al* (2001). *Band gap engineering based on* $Mg_xZn_{1-x}O$ *and* $Cd_yZn_{1-y}O$ *ternary alloy films*. Appl. Phys. Lett. **78**, 1237

101 Ohtomo, A., *et al* (2000). *Room-temperature stimulated emission of excitons in ZnO/(Mg,Zn)O superlattices*. Appl. Phys. Lett. **77,** 2204

102 Liu, K., W., *et al* (2007). $Zn_{0.8}Mg_{0.2}O$*-based metal–semiconductor–metal photodiodes on quartz for visible-blind ultraviolet detection*. J. Phys. D **40**, 2765

103 Liu, K., W., *et al* (2008). *The growth of ZnMgO alloy films for deep ultraviolet detection*. J. Phys. D **41**, 125104

104 Ohtomo, A., *et al* (1998). *$Mg_xZn_{1-x}O$ as a II–VI widegap semiconductor alloy*. Appl. Phys. Lett. **72**, 2466

105 Zorba, V., Chen, X., and Mao, S. S., (2010). *Superhydrophilic TiO_2 surface without photocatalytic activation*. Appl. Phys. Lett. **96**, 093702

106 Wang, R., et al (1997). *Light-induced amphiphilic surfaces*. Nature **388**, 431

107 Asahi, R., Morikawa, T., Ohwaki, T., Aoki, K., Taga, Y., (2001). *Visible-Light Photocatalysis in Nitrogen-Doped Titanium Oxides*. Science **293**, 269

108 McFarland, E.W., Tang, J., (2003). *A photovoltaic device structure based on internal electron emission*. Nature **421**, 616

109 Dubrovinsky, L.S., *et al* (2001). *The hardest known oxide*. Nature **410**, 653

110 Tan, B., and Wu, Y., (2006). *Dye-Sensitized Solar Cells Based on Anatase TiO_2 Nanoparticle/Nanowire Composites*. J. Phys. Chem. B, **110,** 15932

111 Grant, F.A., (1959). *Properties of Rutile (Titanium Dioxide)*. Rev. Mod. Phys. 31, 646

112 Li, W., et al (2009). *Highly thermal stable and highly crystalline anatase TiO_2 for photocatalysis*. Environ Sci Technol. **43**, 5423

113 Kang, S. H., et al (2008). *Columnar rutile TiO_2 based dye-sensitized solar cells by radio-frequency magnetron sputtering*. J. Power Sources **184**, 331

114 Kadoshima, M., et al (2003). *Rutile-type TiO_2 thin film for high-k gate insulator*. Thin solid films **424**, 224

115 Zhang, Y. X., et al (2002). *Hydrothermal synthesis and photoluminescence of TiO_2 nanowires*. Chem. Phys. Lett. **365**, 300

116 Wu, J.-M., Shih, H. C., Wu, W.-T., Tseng, Y.-K., and Chen, I-C., (2005). *Thermal evaporation growth and the luminescence property of TiO_2 nanowires*. J. Crystal Growth **281**, 384

117 Okimura, K., (2001). *Low temperature growth of rutile TiO_2 films in modified rf magnetron sputtering*. Surf. Coatings Tech. **135**, 286

118 Thompson, A.G., (1997). *MOCVD Technology for Semiconductors*. Mat. Lett. **30**, 255

119 Pierson, H. O., (1999). *Handbook of Chemical Vapor Deposition: Principles, Technology and Applications* (Second Ed.). Noyes Publications, Newyork

120 Cuomo, J. J., Rossnagel, S.M., Kaufman, H. R., (Eds.) (1989). *Handbook of Ion Beam Processing Deposition: Principles, Deposition, Film Modification and Synthesis*. Noyes Publications, New Jersey

121 Sun, C. J., Kung, P., Saxler, A., Ohsato, H., Haritos, K., and Razeghi, M., (1994). *A crystallographic model of (0001) aluminum nitride epitaxial thin film growth on (0001) sapphire substrate*. J. Appl. Phys. **75**, 3964

122 Koblmueller, G., et al (2003). *Growth diagram and morphologies of AlN thin films grown by molecular beam epitaxy*. J. Appl. Phys. **93**, 9591

123 Meng, G. Y. Azéma, N., Crosa, B., Durand, J., and Cot, L., (1993). *The growth mechanism of <1010> oriented AlN thin films by low-frequency plasma-enhanced metalorganic chemical vapour deposition process.* J. Crystal Growth **129**, 610

124 Harris, H., Biswas, N., Temkin, H., Gangopadhyay, S., and Strathman, M., (2001). *Plasma enhanced metalorganic chemical vapor deposition of amorphous aluminum nitride*. J. Appl. Phys. **90**, 5825

125 Vispute, R. D., Narayan, J., Wu, H., and Jagannadham, K., (1995). *Epitaxial growth of AlN thin films on silicon (111) substrates by pulsed laser deposition*. J. Appl. Phys. **77**, 4724

126 Meng, W. J., Sell, J. A., Perry, T. A., Rehn, L. E., and Baldo, P. M., (1994). *Growth of aluminum nitride thin films on Si(111) and Si(001): Structural characteristics and development of intrinsic stresses*. J. Appl. Phys. **75**, 3446

127 Jones, A.C., and Hitchman, M. L., (2009). *Chemical Vapour Deposition: precursors, processes and applications.* Royal Society of Chemistry Publishing, Cambridge

128 Neumayer, D.A., and Ekerdt, J.G., (1996). *Growth of Group III Nitrides. A Review of Precursors and Techniques*. Chem. Mater. **8(1)**, 9

129 Zetterling, C.-M., et al (1997). *Investigation of aluminum nitride grown by metal–organic chemical-vapor deposition on silicon carbide.* J. Appl. Phys. **82**, 2990

130 Ambacher, O., et al (1996). *Thermal stability and desorption of Group III nitrides prepared by metal organic chemical vapor deposition*. J. Vac. Sci. Technol. B **14**, 3532

131 Eason, R. (Ed.) (2007). *Pulsed laser deposition of thin films: Application led growth of functional materials.* John Willey and Sons, New Jersey

132 Gu, X. Q., et al (2007). *Room-temperature photoluminescence from ZnO/ZnMgO multiple quantum wells grown on Si(111) substrates*. Appl. Phys. Lett. **91**, 022103

133 Simmons, J.D., and McDonald, J.K., (1972). *The emission spectrum of AlN.* J. Mol. Spectrosc. **41**, 584

134 Gonjalo, J., Afonso, C. N., and I. Madaringa (1997). *Expansion dynamics of the plasma produced by laser ablation of BaTiO3 in a gas environment*. J.Appl.Phys. **81**, 957

135 Huang, M. H., (2001). *Room-Temperature Ultraviolet Nanowire Nanolasers*. Science **292**, 1897

136 Yan, R., Gargas, D., and Yang, P., (2009). *Nanowire photonics*. Nature Photonics **3**, 569

137 Baruah, S., and Dutta, J., (2009). *Hydrothermal growth of ZnO nanostructures.* Sci. Technol. Adv. Mater. **10,** 013001

138 Van Stryland, W., Sheik-Bahae, M., Saida, A.A., and Hagana, D.J., (1993). *Characterization of nonlinear optical absorption and refraction*. Progress in Crystal Growth and Characterization of Materials, **27**, 279

139 Sheik-Bahae, M., Said, A., A., Wei, T. H., Hagan, D. J., and Van Stryland, E., W., (1990). *Sensitive measurement of optical nonliniearties using a single beam*. IEEE J. Quantum Electronics **26**, 760

140 Henari, F., Z., Morgenstern, K., Blau, W., J., Karavanskii, V., A., and Dneprovskii, V., S., (1995). *Third order nonlinearity and all-optical switching in porous silicon.* Appl. Phys. Lett. **67**, 323

141 Yang, G., et al, (2001). *Large Third-order nonlinear optical susceptibility of Rh-doped $BaTiO_3$ thin films prepared by pulsed laser deposition*. Chin. Phys. Lett. **18**, 1598

142 Jones, K. A., et al (1998). *AlN an an encapsulate for annealing SiC.* J. Appl. Phys. **83**, 8010

143 Kong, Y.C., et al (2008). *Charge storage characteristics in Al/AlN/Si metal–insulator–semiconductor structure based on deep traps in AlN layer.* Appl. Phys. A **90**, 545

144 Kneissl, M., et al (2007). *Ultraviolet semiconductor laser diodes on bulk AlN.* J. Appl. Phys. **101**, 123103

145 Bakalova, S., et al (2007). *Influence of in-situ nitrogen pressure on crystallization of pulsed laer deposited laser beams.* Appl. Surf. Sci. **253**, 8215

146 Fujimura, N., Nishihara, T., Goto, S., Xu, J., Ito, T., (1993). *Control of preferred orientation for* ZnO_x *films: contraol of self-texture.* J. Cryst. Growth **130**, 269

147 Yoshiyama, H., et al (1988). *Role of surface energy in thin-film growth of electroluminenscent ZnS, CaS and SrS.* J. Cryst. Growth **86**, 56

148 Strassburg, M., et al (2004). *The growth and optical properties of large, high-quality AlN single crystals.* J. Appl. Phys. **96**, 5870

149 Cao, Y.G., et al (2000). *Blue emission and Raman scattering spectrum from AlN nanocrystalline popwders.* J. Cryst. Growth 213, 198

150 Mattila, T., and Nieminen, R.M., (1996). *Ab initio study of oxygen point defects in GaAs, GaN and AlN.* Phys. Rev., B **54**,16676

151 Sun, J., Wu, J., Ling, H., Shi, W., Ying, Z., and Li, F., (2001). *Photoluminescence and its time evolution of AlN thin films.* Phys. Lett. A **280**, 381

152 Kumar, A., Chan, H.L., Weimer, J.J., and Sanderson, L., (1997). *Structural characterization of pulsed laser deposited AlN thin flms on semiconductor substrates.* Thin Solid Films **308-309**, 406

153 Edgard, J.H., (Ed.), (1994). *Properties of group-III nitrides*. INSREC, London

154 Kurucz, R.L., and Bell, B., (1995). *Atomic Line Data, Kurucz CD-ROM No. 23. http://www.cfa.harvard.edu/amp/ampdata/kurucz23/sekur.html,*Smithsonian Astrophysical Observatory, Cambridge, MA

155 NIST atomic spectra database, http://physics.nist.gov/PhysRefData/ASD/index.html, ver. 3.0.0.6 (2005)

156 Sharma, A. K., and Thareja, R. K., (2000). *Pulsed laser ablation of Al in presence of nitrogen: formation of AlN.* J. Appl. Phys, **88**, 7334

157 Knudtson, J.T., Green, W.B., and Sutton, D.G., (1987). *UV-VIS spectroscopy of laser produced aluminium plasmas.* J.Appl. Phys., **61**, 4771

158 Rahman, M., M., Yu, G., Soga, T., Jimbo, T., Ebisu, H., and Umeno, M., (2000). *Refractive index and degree of inhomogeneity of nanocrystalline* TiO_2 *thin films: effects of substrate and annealing temperature.* J. Appl. Phys., **88**, 4634

159 Kim, S., K., Kim, W., D., Kim, K., M., Hwang, C., S., Jeong, J., (2004). *High dielectric constant* TiO_2 *thin films on a Ru electrode grown at* 250^o *C by atomic layer deposition.* App. Phys. Lett., **18**, 4112

160 Armstrong, A.R., Armstrong, G., Canales, J., Garcia, R., Bruce, P.G., (2005). *Lithium-Ion Intercalation into* TiO_2*-B Nanowires.* Adv. Mater. **17**, 862

161 Richards, B.S., Cotter, J.E., and Honsberg, C.B., (2002). *Enhancing the surface passivation of* TiO_2 *coated silicon wafers.* Appl. Phys. Lett. **80**, 1123

162 Watanabe, T., *et al* (1999). *Photocatalytic activity and photoinduced hydrophilicity of titanium dioxide coated glass.* Thin Solid Films **351**, 260

163 Eliahou-Niv, S., Dahan, R., and Golan, G., (2006). *Design and analysis of a novel tunable optical filter.* Microelectronics Journal **37**, 302

164 Bange, K., Ottermann, C.R., Anderson, O., Jeschkowski, U., Laube, M., and Feile, R., (1991). *Investigations of* TiO_2 *films deposited by different techniques.* Thin Solid Films **197,** 279

165 Yagi, S., Shimizu, M., Okumura, H., Ohashi, H.i, Yano, Y., and Akutsu, N., (2007). *High Breakdown Voltage AlGaN/GaN Metal–Insulator–Semiconductor High-Electron-Mobility Transistor with* TiO_2*/SiN Gate Insulator.* Jpn. J. Appl. Phys. **46**, 2309

166 Deloach, J. D., Scarel, G., and Aita, C. R., (1999). *Correlation between titania film structure and near ultraviolet optical absorption*. J. Appl. Phys. **85**, 2377

167 Gouma, P.I., Dutta, P.K., and Mills, M.J., (1999). *Structural stability of titania thin films.* Nano Structured Mater. **11**, 1231

168 Won, D.J., Wang, C.H., Jang, H.K., and Choi, D.J., (2001). *Effects of thermally induced anatase-to-rutile phase transition in MOCVD-grown TiO2 films on structural and optical properties.* Appl. Phys. A **73**, 595

169 Yamamoto, S., Sumita, T., Sugiharuto, Miyashita, A., and Naramoto, H., (2001). *Preparation of epitaxial TiO2 films by pulsed laser deposition technique.* Thin Solid Films **401**, 88

170 Nakamura, T., Ichitsubo, T., Matsubara, E., Muramatsu, A., Sato, N., and Takahashi, H., (2005). *Preferential formation of anatase in laser-ablated titanium dioxide films.* Acta Materialia **53**, 323

171 Luca, D., Macovel, D., and Teodorescu, C. M., (2006). *Characterization of titania thin films prepared by reactive pulsed-laser ablation.* Surface Science **600**, 4342

172 Lackner, J. M., Waldhauser, W., Ebner, R., Major, B., and Schoberl, T., (2004). *Pulsed laser deposition of titaniumoxide coatings at room temperature—structural, mechanical and tribological properties.* Surface & Coatings Technology **180**, 585

173 Kitazawa, S., Choi, Y., and Yamamoto, S., (2004). *In situ optical spectroscopy of PLD of nano-structured* TiO_2. Vacuum **74**, 637

174 Kim, J. H., Lee, S., Im, H. S., (1999). *The effect of target density and its morphology on* TiO_2 *thin films grown on Si(100) by PLD.* Appl. Surf. Sci. **151**, 6

175 Long, H., Hwang, G., Chen, A., Li, Y., and Lu, P., (2008). *Growth and characteristics of laser deposited anatase and rutile* TiO_2 *films on Si substrates.* Thin solid films **517**, 745

176 Xin, Y., Han, K., Stampe, P.A., and Kennedy, R.J., (2006). *The effect of oxygen pressure on the microstructures of Co-doped rutile* TiO_2 *thin films grown by pulsed laser deposition.* J.Crystal.Growth **290**, 459

177 Tang, H., Prasad, K., Sanjines, R., Schmid, P.E., and Levy, F., (1994). *Ellectrical and optical properties of* TiO_2 *anatase thin films.* J. Appl. Phys. **75**, 2042

178 Daude, N., Gout, C., and Jouanin, C., (1977). *Electronic band structure of titanium dioxide*. Phys. Rev. B **15**, 3229

179 Chertihin, G.V., and Andrews, L., (1995). *Reactions of Laser Ablated Titanium, Zirconium, and Hafnium Atoms with Oxygen Molecules in Condensing Argon.* J. Phys. Chem. **99,** 6356

180 Erkov, V.G., Devyatoba, S.F., Molodstova, E.L., Malsteva, T.V., and Yanovskii, U.A., (2000). *Si–*TiO_2 *interface evolution at prolonged annealing in low vacuum or* N_2O *ambient.* Appl. Surf. Sci.**166**, 51

181 Shao,L., Zhang, L., Chen, M., Lu, H., and Zhou, M., (2001). *Reactions of titanium oxide with water molecules. A matrix isolation FTIR and density functional study.* Chem. Phys. Lett. **343,** 178

182 McDevitt, N. T., and Ban, W. L.,(1964). *Infrared absorption study of metal oxides in the low frequency region (700-240* cm^{-1}*).* Spectrochimica Acta **20**, 799

183 Zeman, P., and Takabayashi, S., (2002). *Self-cleaning and antifogging effects of* TiO_2 *films prepared by radio frequency magnetron sputtering.* Journal of Vacuum Science Technology A **20**, 388

184 Lee,C. J., Lee,T. J, Lyu,S.C., Zhang,Y., Ruh,H. and Lee, H. J.(2002). *Field emission from well-aligned zinc oxide nanowires grown at low temperature*. Appl.Phys.Lett. **81**, 3648

185 Hoffman, R.L., Norris B. J., and WageR, J. F.(2003). *ZnO-based transparent thin-film transistors*. Appl.Phys.Lett. **82**, 733

186 Look , D. C., Claflin,B., Alivov, Ya. I., Park, S. J., (2004). *The future of ZnO light emitters*. Physica Status Solidi (b) **201**, 2203

187 Xu,H., Liu,X., Cui ,D., Li,M., Jiang,M., (2006). *A novel method for improving the performance of ZnO gas sensors*. Sensors and Actuators B **114**, 301

188 Gonzalez-Valls, I. and Lira-Cantu,M (2009).Vertically-aligned nanostructures of ZnO for excitonic solar cells: a review. Energy Environ. Sci. **2**, 19

189 Cui, J., Safodev, S., Blumstengel, S., Puls, J., and Henneberger, F., (2006). *Optical gain and lasing of ZnO/ZnMgO multiple quantum wells: From low to room temperature*. Appl. Phys. Lett. **89**, 051108

190 Hofstetter, D., Theron, R., El-Shaer, A.H., Bakin, A., and Waag, A., (2008). *Demonstration of a ZnO/MgZnO-based one-dimensional photonic crystal multiquantum well laser*. Appl. Phys. Lett. **93**, 101109

191 Claeyssens,F., Freeman,C.L., Allan,N.L., Sun,Y., Ashfold,M.N.R. and Harding,J.H. (2005). *Growth of ZnO thin films—experiment and theory*. J. Mater. Chem. **15**, 139

192 Kawakami, M., Hartanto,A.B., Nakata,Y. and Okada,T. (2003). *Synthesis of ZnO Nanorods by Nanoparticle Assisted Pulsed-Laser Deposition*. Jpn. J. Appl. Phys. **42,** L33

193 Claeyssens,F., Cheesman, A., Henley,S.J. and Ashfold,M.N.R. (2002). Studies of the plume accompanying pulsed ultraviolet laser ablation of zinc oxide. J.Appl. Phys. **92**, 6886

194 Namba,S., Nozu, R., Takiyama, K.,Oda,T.,(2006). *Spectroscopic study of ablation and recombination processes in a laser-produced ZnO plasma*. J. Appl. Phys. **99**, 073302

195 Ozerov,I.,Bulgakov, A.V., Nelson, D.K., Castell, R. and Marine,W. (2005). *Production of gas phase zinc oxide nanoclusters by pulsed laser ablation*. Appl. Surf. Sci. **247**, 1

196 Harilal,S.S., O'Shay,B., Tao,Y. and Tillack,M.S. (2006). *Ambient gas effects on the dynamics of laser-produced tin plume expansion*. J.Appl.Phys. **99**, 083303

197 Ying,M., Xia,Y., Sun, Y., Zhao, M., Ma, Y., Liu, X., Li, Y. and Hou, X. (2003). *Plasma properties of a laser-ablated aluminum target in air*. Laser and particle beams **21**, 97

198 Zel'dovich, Ya. B., and Raizer, Yu. P., (1966). *Physics of Shock Waves and High-Temperature Hydrodynamic Phenomena*. New York: Academic Press

199 Arnold, N., Gruber, J.and Heitz, J. (1999). *Spherical expansion of the vapor plume into ambient gas: an analytical model*. Appl. Phys. A **69**, S87

200 Beilis, I. I., (2007). *Laser plasma generation and plasma interaction with ablative target*. Laser. Part. Beams **25**, 53

201 Shukla, G., and Khare, A., (2009).*Optical Emission Spectroscopic Studies on Laser Ablated* TiO_2 *Plasma.* App. Surf. Sci. **255**, 8730

202 Jagdish, C., and Pearton, S. J., (2006). *Zinc Oxide bulk, thin films and nanostructures: processing, properties and applications.* Elsevier, Oxford

203 Hansen,T.N., Schou,J. and Lunney,J.G. (1997). Angular distributions of silver ions and neutrals emitted in vacuum by laser ablation. Europhys. Lett. **40 (4),** 441

204 Kasperczuk et al (2007). *Interferometric investigations of influence of target irradiation on the parameters of laser produced plasma jets*. Laser and Particle Beams **25**, 425

205 Thareja, R.K., and Sharma, A.K. (2006). *Reactive pulsed laser ablation: Plasma Studies*. Laser and Particle Beams **24**, 311

206 Hansen,T.N, Schou,J and Lunney,J.G (1998).Angle-resolved energy distributions of laser ablated silver ions in vacuum. Appl.Phys.Lett. **72**, 1829

207 Shannon, R.D., (1976). *Revised effective ionic radii and systematic studies of interatomic distances in halides and chalcogenides*. Acta Crystallogr. Sect. A: Cryst. Phys. Diffr. Theor. Gen. Crystallogr. **32**, 751

208 Segnit, E. R., and Holland, A. E., (1965). *The System MgO-ZnO-SiO*$_2$. J. Am. Ceram. Soc. **48**, 409

209 Shukla, G., and Khare, A., (2009b). *Effect of Mg doping and substrate temperature on the structural and optical properties of* $Zn_{1-x}Mg_xO$ *thin films.* Appl. Phys. A **96**, 713

210 Pan, C.J., Lin, K. F., Hsu, W. T., and Hsieh, W.F., (2007). *Raman study of alloy potential fluctuations in* $Mg_xZn_{1-x}O$ *nanopowders*. J. Phys.: Condens. Matter **19**, 186201

211 Arguello, C. A., Rousseau, D. L., and Porto, S. P. S.,(1969). *First-Order Raman Effect in Wurtzite-Type Crystals.* Phys. Rev. **181**, 1351

212 Pradhan, A. K., Zhang, K., Loutts, G. B., Roy, U. N., Cui, Y., Burger, A., (2004). *Structural and spectroscopic characteristics of ZnO and ZnO:*Er^{3+} *nanostructures.* J. Phys.: Condens. Matter **16**, 7123

213 Calleja, J. M., and Cardona, M., (1977). *Resonant Raman scattering in ZnO.* Phys. Rev. B **16**, 3753

214 Anderson, A., (Ed.) (1973). *The Raman Effect: Applications, Vol.2*. Published by Dekker, M., New York

215 Mang, A., Reimann, K., and Rübenacke, St., (1995). *Band gaps, crystal-field splitting, spin-orbit coupling, and exciton binding energies in zno under hydrostatic pressure.* Solid State Commun. **94**, 251

216 Chia, C. H., *et al* (2003). *Confinement-enhanced biexciton binding energy in ZnO/ZnMgO multiple quantum wells*. Appl.Phys.Lett. **82**, 1848

217 Choopun, S., Vispute, R. D., Yang, W., Sharma, R. P., Venkatesan, T., and Shen, H., (2002). *Realization of band gap above 5.0 eV in metastable cubic-phase* $Mg_xZn_{1-x}O$ *alloy films.* Appl.Phys.Lett. **80**, 1529

218 Hullavarad, S.S., Hullavarad, N.V., Pugel, D.E., Dhar, S., Venkatesan, T., and Vispute, R.D., (2008). *Structural and chemical analysis of pulsed laser deposited* $Mg_xZn_{1-x}O$ *hexagonal (x = 0.15, 0.28) and cubic (x = 0.85) thin films*. Optical Materials **30**, 993

219 Maemoto, T., Ichiba, N., Ishii, H., Sasa, S., and Inoue, M., (2007). *Structural and optical properties of ZnMgO thin films grown by pulsed laser deposition using ZnO-MgO multiple targets.* J. Phys. Conf. Series **59**, 670

220 Lorenz, M., et al (2005). *$Mg_xZn_{1-x}O$ ($0 \le x < 0.2$) nanowire arrays on sapphire grown by high-pressure pulsed-laser deposition*. Appl. Phys. Lett. **86**, 143113

221 Thomas, D.G., (1960). *The exciton spectrum of zinc oxide.* J. Phys. Chem. Solids **15**, 86

222 Elliot, R.J., (1959). *Intensity of Optical Absorption by Excitons*. Phys. Rev. **108**, 1384

223 Muth, J.F., Kolbas, R.M., Sharma, A.K., Oktyabrsky, S., and Narayan, J., (1999). *Excitonic structure and absorption coefficient measurements of ZnO single crystal epitaxial films deposited by pulsed laser deposition.* J.Appl.Phys. **85**, 7884

224 Vanheusden, K., Seager, C. H., Warren, W. L., Tallant, D. R., and Voigt, J. A., (1996). *Correlation between photoluminescence and oxygen vacancies in ZnO phosphors.* Appl. Phys. Lett**.** **68**, 403

225 Egelhaaf, H.-J., and Oelkrug, D., (1996). *Luminescence and nonradiative deactivation of excited states involving oxygen defect centers in polycrystalline ZnO.* J. Cryst. Growth **161**,190

226 Chichibu, S.F., Yoshida, T., Onuma, T., Nakanishi, H., (2002). *Helicon-wave-excited-plasma sputtering epitaxy of ZnO on sapphire (0001) substrates.* J. Appl. Phys. **91**, 874

227 Yoshimoto, M., (1995). *Atomic-scale formation of ultrasmooth surfaces on sapphire substrates for high-quality thin-film fabrication.* Appl. Phys. Lett. **67**, 2615

228 Hsu, T., and Kim, Y., (1991). Structure of the α-Al_2O_3(1120) surfaces: facets and reconstruction. Surf. Sci. **258**, 119

229 Kurnosikov, O., Pham Van, L., and Cousty, J., (2000). *About anisotropy of atomic-scale height step on (0001) sapphire surface.* Surf. Sci. **459**, 256

230 Lin, J.-H., Chen, Y.-J., Lin, H.-Y., and Hsieh, W.-F., (2005). *Two-photon resonance assisted huge nonlinear refraction and absorption in ZnO thin films*. J. Appl. Phys. **97**, 033526

231 Wang,G., Kiehne, G. T., Wong, G. K. L., Ketterson, J. B., Liu, X., and Chang, R. P. H., (2002). *Large second harmonic response in ZnO thin films*. Appl. Phys. Lett. **80**, 401

232 Gu, B., and Ji, W., (2008). *Two step four photon absorption.* Optics Express **16**, 10208

233 Djurišić, A. B., and Leung, Y. H., (2006). *Optical properties of ZnO nanostructures*. Small, **2**, 944

234 Ma, X., Chen, P., Li, D., Zhang, Y., and Yang, D., (2007). *Electrically pumped ZnO film ultraviolet random lasers on silicon substrate*. Appl. Phys. Lett. **91**, 251109 - 251111

235 Wang, Z. L., (2004). *Zinc oxide nanostructures: growth, properties and applications.* J. Phys.: Condens. Matter **16**, R829

236 Zhao, Q., X., Klason, P., and Willander, M., (2007*). Growth of ZnO nanostructures by vapor-liquid-solid method*. Appl. Phys. A, **88**, 27

237 Reeber, R., R., (1970). *Lattice parameters of ZnO from 4.2° to 296°K.* J. Appl. Phys., **41**, 5063

238 Weintraub, B., Zhou, Z., Li, Y., and Deng, Y., (2010). *Solution synthesis of one-dimensional ZnO nanomaterials and their applications.* Nanoscale **2**, 1573

239 Xu, C., Paul, S., Cao, L., and Gao, D., (2010). *Preferential Growth of Long ZnO Nanowire Array and Its Application in Dye-Sensitized Solar Cells.* J. Phys. Chem. C, **114**, 125

240 Ohnishi, T., Ohtomo, A., Kawasaki, M., Takahashi, K., Yoshimoto, M., and Koinuma, H., (1998). *Determination of surface polarity of c-axis oriented ZnO films by coaxial impact-collison ion scattering spectroscopy.* Appl. Phys. Lett. **72**, 824

241 Vayssieres, L., (2005). *Growth of arrayed nanorods and nanowires of ZnO from aqueous solutions.* Adv. Mater. **15**, 464

242 Sugunan, A., Warad, H.C., Boman, M., and Dutta, J., (2006). *Zinc oxide nanowires in chemical bath on seeded substrates: Role of hexamine.* J. Sol-Gel Sci. Technol. **39**, 49

243 Al-Suleiman, Motor, A. C., El-Shaer, A., Bakin, A., Wehmann, H. H., and Waag, A., (2006). *Photoluminenscence properties: catalyst free ZnO nanorods and layers versus bulk ZnO.* Appl. Phys. Lett. **89**, 231911

244 Chan, S.W., *et al* (2006). *Second harmonic generation in zinc oxide nanorods.* Appl. Phys. B **84**, 351

245 Neumann, U., Grunwald, R., Griebner, U., Steinmeyer, G., and Seeber, W., (2004). *Second-harmonic efficiency of ZnO nanolayers*. Appl. Phys. Lett. **84**, 170

246 Larciprete, M.C., Haertle, D., Belardini, A, Bertolotti, M., Sarto, F., and Gunter, P., (2006). *Characterization of second and third order optical nonlinearities of ZnO sputtered films.* Appl. Phys. B **82**, 431

247 Prasanth, R., Van Vugt, L. K., Vanmaekelbergh, D. A. M., and Gerritsen, H. C., (2006). *Resonance enhancement of optical second harmonic generation in a ZnO nanowire*. Appl. Phys. Lett. **88**, 181501

248 Burin, A. L., Cao, H., and Ratner, M. A., (2003). *Two-photon pumping of a Random Laser*. IEEE J. Sel. Top. Quantum Electron. **9**, 124

249 Dai, D. C., Xu, S. J., Shi, S. L., Xie, M. H., and Che, C. M., (2005). *Efficient multiphoton-absorption-induced luminescence in single crystalline ZnO at room temperature*. Opt. Lett. **30**, 3377

250 Zhang, C. F., *et al* (2005). *Observation of two-photon-induced photoluminescence in ZnO microtubes*. Appl. Phys. Lett. **87**, 051920

251 Zhang, C. F., et al (2006). *Femtosecond pulse excited two-photon photoluminescence and second harmonic generation in ZnO nanowires*. Appl. Phys. Lett. **89**, 042117

252 Dong, Z.W. et al (2007). *Multi-photon excitation UV emission by femtosecond pulses and nonlinearity in ZnO single crystal*. J.Phys.: Condens. Matter **19**, 216202

253 Zhang, C.F., Dong, Z.W., You, G.J., and Qian, S.X., (2006b). *Multiphoton route to ZnO nanowire lasers*. Opt. Lett. **31**, 3345

254 Chen, Y., Tuan, N.T., Segawa, Y., Ko, Hang-ju, Hong, Soon-ku, and Yao, T., (2001). *Stimulated emission and optical gain in ZnO epilayers grown by plasma-assisted molecular-beam epitaxy with buffers*. Appl. Phys. Lett. **78**, 1469

255 Leong, E.S.P., Yu, S.F., and Lau, S.P., (2006). *Directional edge-emitting UV random laser diodes*. Appl. Phys.Lett. **89**, 221109

256 Zhou, H., *et al* (2007). *Ordered, uniform-sized ZnO nanolaser arrays*. Appl. Phys. Lett. **91**, 181112

257 Hauschild, R., and Kalt, H., (2006). *Guided modes in ZnO nanorods*. Appl. Phys. Lett. **89**, 123107

258 Klingshirn, C., Hauschild, R., Fallert, J., and Kalt, H., (2007). *Room-temperature stimulated emission of ZnO: Alternatives to excitonic lasing*. Phys. Rev. B **75**, 115203

259 Mitsubori, S., Katayama, I., Lee, S.H., Yao, T., and Takeda, J., (2009). *Ultrafast lasing due to electron-hole plasma in ZnO nano-multipods*. J. Phys.: Condens. Matter **21**, 064211

List of Publications

1. International Journals:

(a) **Published**

i. Shukla, G. and Khare, A., (2008). *Dependence on* N_2 *pressure of the crystal structure and surface quality of AlN thin films deposited via pulsed laser deposition technique at room temperature*. Applied Surface Science, **255**, 2057

ii. Shukla, G. and Khare, A., (2009). *Effect of substrate annealing on the quality of pulsed laser deposited* $Zn_{1-x}Mg_xO$ *thin films*. Applied Surface Science, **255**, 7017

iii. Shukla, G. and Khare, A., (2009). *Optical emission spectroscopic studies on laser ablated* TiO_2 *plasma*. Applied Surface Science, **255**, 8730

iv. Shukla, G. and Khare, A., (2009). *Effect of Mg doping and substrate temperature on the properties of pulsed laser deposited epitaxial* $Zn_{1-x}Mg_xO$ *thin films*. Applied Physics A, **96**, 713

v. Shukla, G., Mishra, P., K., and Khare, A., (2010). *Effect of annealing and* O_2 *pressure on structural and optical properties of pulsed laser deposited* TiO_2 *thin films*. Journal of Alloys and Compounds, **489**, 246

vi. Shukla, G. and Khare, A., (2010). *Spectroscopic studies on laser ablated ZnO plasma and correlation with pulsed laser deposited ZnO thin film properties*. Laser and Particle Beams, **28**, 149

vii. Shukla, G. and Khare, A., (2011). *Effect of Pre-heating on Hydrothermal Growth and Optical Properties of ZnO Nanorods*. International Journal of Nanoscience, *Accepted for publication*

(b) **To be communicated**

i. Shukla, G. and Khare, A, “Multi photon absorption induced random lasing action in ZnO nanorods”, *to be submitted (2011)*

ii. Shukla, G. and Khare, A, “Room temperature excitonic emission and Non-linear optical properties of Mg-doped ZnO thin films”, *to be submitted (2011)*

iii. Shukla, G. and Khare, A, “Plasma dynamics studies of Al plasma during pulsed laser deposition of AlN thin film”, *to be submitted (2011).*

2. Conference Presentations

i. “Effect of Pre-heating on Hydrothermal Growth and Optical Properties of ZnO Nanorods” by Gaurav Shukla and Alika Khare, paper presented at ICONSAT 2010, Feb17-20, 2010 at IIT Bombay, Mumbai.

ii. “Effect of dynamics of ZnO plasma on the pulsed laser deposited ZnO thin films” by Gaurav Shukla and Alika Khare, *Oral presentation* at Plasma 09, Dec 8 – 11 2009, held at NIT Hamirpur.

iii. “Multi Photon Absorption induced amplified spontaneous emission from hydrothermally grown ZnO nanorods” by Gaurav Shukla and Alika Khare, accepted for presentation at ASSP 2010 (OSA Laser Congress), Jan 31, 2010 – Feb 3, 2010, SanDiego, CA, USA.

iv. “Pulsed laser deposition of $Zn_{1-x}Mg_xO$ thin films” by Gaurav Shukla and Alika Khare, paper presented in NLS 2009 held at LASTEC (New Delhi) during Jan 7-10 2009.

v. “Measurement of electron number density and electron temperature during pulsed laser ablation of TiO_2 target” by Gaurav Shukla and Alika Khare, paper presented in NLS 2009 held at LASTEC (New Delhi) during Jan 7-10 2009.

vi. “Effect of substrate annealing on the quality of pulsed laser deposited $Zn_{1-x}Mg_xO$ thin films” by Gaurav Shukla and Alika Khare, presented at Cochin NANO 2009 held at CUSAT (kerala) during JAN 3-6 2009.

vii. “Plasma dynamics studies during pulsed laser deposition of AlN” by Gaurav Shukla and Alika Khare, paper presented in PLASMA 07 held at IPR Gandhinagar (Gujrat) during Dec 6 -10 2007.

viii. “Pulsed Laser Ablation of Indium in N_2 Environment” by Gaurav Shukla and Alika Khare, paper presented in PLASMA 07 held at IPR Gandhinagar (Gujrat) during Dec 6 - 10 2007.

ix. “Effect of Substrate on Pulsed Laser Deposition of InN Thin Film” by Gaurav Shukla and Alika Khare, paper presented in PLD-2007 held at Rajkot (Gujrat) during oct 3-5 2007.

x. "Nanostructured Growth of AlN Thin Films by Pulsed Laser Deposition" by Gaurav Shukla and Alika Khare, (ORAL) paper presented in PLD-2007 held at Rajkot (Gujrat) during oct 3-5 2007.

xi. "Optical and structural properties of reactive pulsed laser deposited AlN thin films" paper presented in "PANE' 07- National Conference of Physics Academy of North East" by Gaurav Shukla and Alika Khare, held at Gauhati University during Jan 7-8, 2007.

xii. "Reactive pulsed laser deposition of AlN thin films and effects of N_2 pressure" by Gaurav Shukla and Alika Khare, paper presented in "Plasma 06 – National Symposium on Plasma Physics" held at MNIT Jaipur during DEC 19-22, 2006.